UNIVERSITY OF CALIFORNIA,
IRVINE

Next Generation Materials: Understanding the Structure and Arrangement of Nanomaterials and the Influence on Functional Properties

DISSERTATION

submitted in partial satisfaction of the requirements
for the degree of

DOCTOR OF PHILOSOPHY

in Chemistry

by

Kellen Marie Kartub

Dissertation Committee:
Professor Robert M. Corn, Chair
Professor A. S. Borovik
Professor Eric Potma
Professor Andrej Lupták

2019

DEDICATION

To

my wonderful family

my amazing husband, Jack

and to my 10-year-old self, who started this journey

TABLE OF CONTENTS

LIST OF FIGURES

LIST OF TABLES

ACKNOWLEDGMENTS

The idea of thanking all the people who have helped me get to this point is a daunting and exciting challenge, as I have racked up quite the list after all this time. But I shall do my best.

First, I must thank my PI, Rob Corn. Thank you for taking a chance on me despite how new I was to this work. Thank you for standing by me these past five years, even when I got a little distracted. I have greatly appreciated the opportunity to learn in your lab.

Thank you to the other members of my committee, Andy Borovik, Eric Potma, and Andrej Lupták. You have been amazing mentors and wonderful sources of information. I sincerely appreciate being able to turn to you (often unannounced) with my questions. I would like to particularly thank Andrej for all he has taught me in the year and half we have collaborated together. I have thoroughly enjoyed learning from you.

To the members of the Corn Lab, without whom I would not be here, I say a very big thank you! Gerald, Adam, Millie, Brandon, Anna, our lovely visitors Yuhei and Hiroshi, you have all been amazingly supportive and kind, and I have learned so much from all of you. I know that between the CGGC, Disneyland visits, group outings, listening to my rants (or freak outs), and laughing over The Office and other tv shows, it is amazing we got work done, but I say it was worth it. Thank you for your support and friendship in the lab and beyond. I have so many fond memories from our times together and I will cherish them forever. And a special thank you to Brandon, who has had to shoulder the burden of sharing brain with me. Without your help, edits, suggestions, advice, patience, and our boba runs, I would not be here. Thank you!

Expanding to the chemistry department in general, there are too many people to thank. It has been an honor getting to know the labs on campus and the amazing people who keep them running. I want to give a special shout out to the Yang Lab (Charlene, Anny, Juliette, Zach,

Brian, Alex, Bianca, Drew, and especially Jeff and Nadia whose hood I would use!), Lupták Lab (Michael Vu, Luiz, Michael Wu, Claire, Kelly, Mona, Kyle, Anya, and Lucy), and Nowick Lab (Mike, Kate, Will, Xing, Gretchen, Maj, James Jr.) as I have had the absolute privilege of being an honorary group member in each of these labs. Everyone in these groups welcomed me into their lab space not only to run experiments but made me feel welcomed into the group as a friend. I can't thank these groups enough for that. I also must also include the Law Lab, Borovik Lab, Evans Lab, Penner Lab, and everyone else who has helped me. These groups have provided advice, spare parts, chemicals, everything! All I had to do was ask and someone was there to help. I am humbled by everyone's kindness and willingness to help.

I know I've already mentioned big thank you's, but here comes another one to the IMRI folk! Truly, this dissertation would not be what it is without their help. The people of IMRI are what made this possible. They have been amazing mentors and I am forever indebted to them and their kindness. Furthermore, I was to thank them for all the patience they have had with me and answering all my questions and all their assistance troubleshooting this thing or another. Thank you Qiyin for your help with the XRD. Thank you, Dr. Tran, for training me on the XPS. Thank you Dr. Zheng and Toshi for your help with the electron microscopes. And a big thank you to Mingjie and Dr. Li. These two really did so much for me. On top of training me and helping me interpret data, they have spent late nights on the instrument with me, and they even tolerated my tendency to burst in and say one of two things "I need help," or "I need TEM time and I need is ASAP!" with my usual flair of panic and crazy. I repeat, I would not have a thesis if it were not for these two and the whole IMRI crew. Thank you, thank you, thank you!

Danielle and Phong, thank you both so much for keeping me sane towards the end. Danielle, your advice both professionally and personally has seen me through so much.

Particularly the bit about prioritizing when I swamped with wedding planning and research. Thank you so much Danielle. Phong, it if weren't for our meetings, I would have been so lost. It is easy to get overwhelmed in grad school but being able to talk things through with you helped me work through everything and stay on track. Thank you so much Phong.

My inorganic ladies, Bianca, Kelsey, Megan, and Monica, thank you. You have been one of my strongest support networks this entire time. You are, without a doubt, some of the kindest, most brilliant, and amazing people I know. I am eternally thankful that we met and got to spend 5+ amazing years together whether it was classes and homework, struggling through orals, or shutting down Sake 2 Me time and again. You have helped me through this process in so many ways, I can't even begin to express it. Sorry I traumatized you that time I wore sweatpants.

To my good friends Mike, Alana, Ben, Krista, Ted, Vicki, Zach and so many other, thank you. Grad school would not have been the same without your friendship and support. Mike, I would have starved without our ramen dinners. Alana, you have been such an inspiration, a wonderful friend, and a great pilates teacher. Ben, thank you for being my choir-bingo buddy and late-night work buddy (even if it meant we kind of enabled each other's terrible sleeping habits). Krista, Ted, Vicki, and the rest of the Loh Down crew, you guys are the best and I have loved working with you and Sandra! Zach, thank you for encouraging my passion for science communication and for letting me play your awesome games!

To all my friends from high school and college, to my newfound Internet friends - Becky, Naomi, Leah, Sarah, Steph, Gabe, Dan, Chery, Gloria, and more. Thank you for supporting me and cheering me on through this crazy process.

Thank you to all my amazing teachers and professors who have always encouraged my passion for science and learning. I wish I told you more how much I appreciate your hard work and support and what a positive impact it had on me.

To my family, my parents, my grandparents, my siblings, my aunts, uncles, cousins, and my new in-laws. Thank you, thank you, thank you. I could go on forever, but I will hit on the main ones. Thank you for your love, your support, and thank you for feeding me!

And to my amazing husband (of two months!) Jack, I say thank you. You have always been my biggest support and encouraged me every step of the way. You helped me through the bad and celebrated the good with me. And in these final months and weeks, you have been simply amazing. I am forever grateful. I cannot imagine my life without you. I love you so much.

It wouldn't be a Kellen Kartub thesis if this wasn't done at… 6 in the morning (?!) after what maaaay have been a very long night. So, if anything is slightly incoherent, you know why. And so, to wrap this up, I say one last time: thank you to every person who has touched my life in such a positive way. I consider myself truly blessed to have so many wonderful people in my life and I really would not be here without you all.

The work presented in this dissertation was supported by the National Science Foundation through grant CHE-1807317 and through grant CHE-1403506.

CURRICULUM VITAE

Kellen Kartub

EDUCATION

University of California, Irvine (Irvine, CA)
Ph.D., Chemistry, 2019
Advisor: Professor Robert Corn

Wellesley College (Wellesley, MA)
B.A., Chemistry, 2014

PROFESSIONAL EXPERIENCE

Graduate Student Researcher
Department of Chemistry, University of California, Irvine (Irvine, CA) 2014-2019

Undergraduate Student Researcher
Department of Chemistry, Wellesley College (Wellesley, MA) 2012-2014

TEACHING EXPERIENCE

UC Irvine, Department of Physical Science
Physical Sciences 220 Science Communication Winter 2019

UC Irvine, Chemistry Department
Chem M3LC, Quantitative Chemistry Lab Fall 2017
Chem 1LD, Introductory Chemistry Lab Summer 2017
Chem M3LC, Quantitative Chemistry Lab, Head TA Fall 2015
Chem M3LC, Quantitative Chemistry Lab Spring 2015
Chem 1A, General Chemistry Lecture Winter 2015
Chem 1P, Preparatory Chemistry Lecture Fall 2014

PEDAGOGY CERTIFICATION

Center for the Integration of Teaching, Research, and Learning Associate Level, UC Irvine
Division of Teaching Excellence and Innovation Certificate of Teaching Excellence, UC Irvine
Division of Teaching Excellence and Innovation Course Design Certificate, UC, Irvine

PUBLICATIONS

B. M. Matthews, A. M. Maley, K. Kartub, and R. M. Corn. Characterizing the Incorporation of DNA into Single NIPAm Hydrogel Nanoparticles with Surface Plasmon Resonance Imaging Measurements. J*ournal of Physical Chemistry C.* **123** 6090-6096 (2019).

H. W. M. Fung, S. So, K. Kartub, and R. M. Corn. Quantitative Characterization of Optical Coupling in Nanoporous ZnO-WO3 and ZnO-PEDOT Composite Electrodeposited Gratings using Electrodiffraction Measurements. *Journal of Physical Chemistry C.* **123** 762-769 (2019).

H. W. M. Fung, S. So, K. Kartub, G. Loget and R. M. Corn. Ultra-Antireflective Electrodeposited Plasmonic and PEDOT Nanocone Array Surfaces. *Journal of Physical Chemistry C.* **2017**, *121* 22377-22383.

S. So, H. W. M. Fung, K. Kartub, A. M. Maley and R. M. Corn. Fabrication of PEDOT Nanocone Arrays with Electrochemically Modulated Broadband Antireflective Properties. *Journal of Physical Chemistry Letters.* **2017**, *8* 576-579.

H. Zhang, K. Kartub, A. Kwan, A. Webb, D. Carrico-Moniz. Synthesis and evaluation of (1S)-1,2-dihydro-1-naphthalenol derivatives against PANC-1 cells. *Tetrahedron Letters.* **2015,** *56* 1720-1723.

POSTERS AND PRESENTATIONS

K. Kartub. Nanostructured Materials for Optical Applications (presentation). SoCal Undergraduate Research Symposium; University of California, Irvine. July 27th, 2018.

K. Kartub. Nanostructured Materials for Optical Applications (presentation). Inorganic Chemistry Seminar Series; University of California, Irvine. May 17th, 2018.

K. Kartub, H. W. M. Fung, R. M. Corn. Attachment Chemistries for Fabricating Functionalized Nanoparticles for Biosensing Applications (poster). The International Chemical Congress of the Pacific Basin Societies; Honolulu, Hawaii. December 17th, 2015.

ABSTRACT OF THE DISSERTATION

Next Generation Materials: Understanding the Structure and Arrangement of Nanomaterials and the Influence on Functional Properties

By

Kellen Kartub

Doctor of Philosophy in Chemistry

University of California, Irvine, 2019

Professor Robert Corn, Chair

This dissertation presents three different projects aimed at understanding how fabrication, functionalization, and arrangement of nanostructures relates to their resulting properties. The composition, dimensions, and arrangement of nanoparticles and nanostructures are particularly significant for controlling the properties of magnetic nanoparticles, optical nanostructures, and directed assemblies of gold nanoparticles. Chapter 2 of this thesis demonstrates how the size and composition of ferrite nanoparticles are directly linked to the unique magnetic properties they exhibit, and how with further functionalization, these nanoparticles can be modified for future biological applications. Magnetic ferrite nanoparticles were synthesized at various sizes, 10 and 40 nm, and then post-synthetically modified with a hydrophilic polyacrylic acid coating before further incorporation of these nanoparticles into biologically relevant systems such as poly-lysine and polyacrylic acid hydrogels. In Chapter 3, we look at the reduction of electrochromic WO_3 and its arrangement within highly patterned nanostructured arrays, which we anticipate will exhibit localized surface plasmon resonance (LSPR) in an effort to develop powerful new surfaces for light-based sensing applications in the near infrared. Several post-fabrication

modification techniques, including furnace reduction and MoO_3 doping, were explored to create permanent reduced states within the WO_3 crystal lattice. Finally, Chapter 4 presents our progress in developing improved methodologies to structurally characterize DNA-gold interactions of smaller masses. 1.4 nm nanogold was bound to 60 base-pair thiol-modified DNA strands, purified, and then analyzed through cryo-electron microscopy.

Chapter 1

Introduction

1.1 Overview of Dissertation

Nanoparticles and nanostructured materials are an enduring area of research due to their fascinating behaviors and wide use in a plethora of applications. Nanoparticles and nanostructures can have dramatically enhanced properties from their bulk counterparts despite having the same material composition.[1,2] Properties such as shape, size, and composition can be tuned for optimal use in applications such as optics,[3,4] cancer therapeutics,[5–7] electronics,[8,9] sensors,[10–12] energy storage,[13–15] and data storage.[16,17] Functionalization of the particle or structure surface widens the range of applications even further to include targeted drug delivery[18–20] and biosensors.[21,22] The composition, dimensions, and arrangement of nanoparticles and nanostructures significantly influence their capabilities, particularly for magnetic nanoparticles,[23–26] optical nanostructures,[27–29] and the directed assembly of gold nanoparticles.[1,30,31] Therefore, understanding how fabrication, functionalization, and arrangement of nanostructures is important in controlling the resulting properties and critical in developing the next generation of nanomaterials.

This dissertation presents three different projects, each based within the idea that nanoscale materials can be designed for specific applications best when their shape, size, composition and arrangement are understood, as well as how these parameters relate to their exhibited properties. Chapter 2 of this thesis demonstrates how the size and composition of ferrite nanoparticles are directly linked to the unique magnetic properties they exhibit, and how with further functionalization, these nanoparticles can be modified for future biological applications. In Chapter 3, we look at the reduction of electrochromic metal oxides and their arrangement within highly patterned nanostructured arrays, which we anticipate will exhibit localized surface plasmon resonance (LSPR) in an effort to develop powerful new surfaces for

light-based sensing applications in the near infrared. Finally, Chapter 4 describes the development of improved methodologies to probe the structure of nanogold bound DNA by cryo-electron microscopy for improved control over DNA directed assemblies of nanogold.

1.2 Magnetic Nanoparticles

Application of magnetic materials is increasing in biological and medicinal fields, where novel magnetic nanoparticles serve as image contrast agents, drug targeting and delivery methods, and biosensors.[18,32–36] For magnets to be effective in a biological system, they need to be highly responsive to a magnetic field, non-aggregating, and hydrophilic as biological systems are aqueous.[24,37] Ferrite nanoparticles, which can be tuned to have a high magnetic susceptibility,[24,34,38] are superparamagnetic at small diameters below 20 nm,[24,37] and can be further functionalized such that they are hydrophilic,[39] are well suited to meet these conditions and for use in biological systems. Chapter 2 of this dissertation presents a new procedure to post-synthetically modify magnetic ferrite nanoparticles of various sizes, 10 and 40 nm, with a hydrophilic polyacrylic acid coating and then further incorporates these nanoparticles into biologically relevant systems such as poly-lysine and polyacrylic acid hydrogels.

1.2.1 Magnetic Behaviors

Magnetic behavior is the response to an externally applied magnetic field that results from the perturbation of spin and orbital motion of electrons. Spin and orbital motions dictate the magnetic moment, the magnetic strength and orientation of a magnetic object.[40] All materials can be classified into at least one of five basic types of magnetic behaviors (Figure 1.1) based on their response to an externally applied magnetic field: diamagnetism, paramagnetism, ferromagnetism, antiferromagnetism, and ferrimagnetism.[25,40]

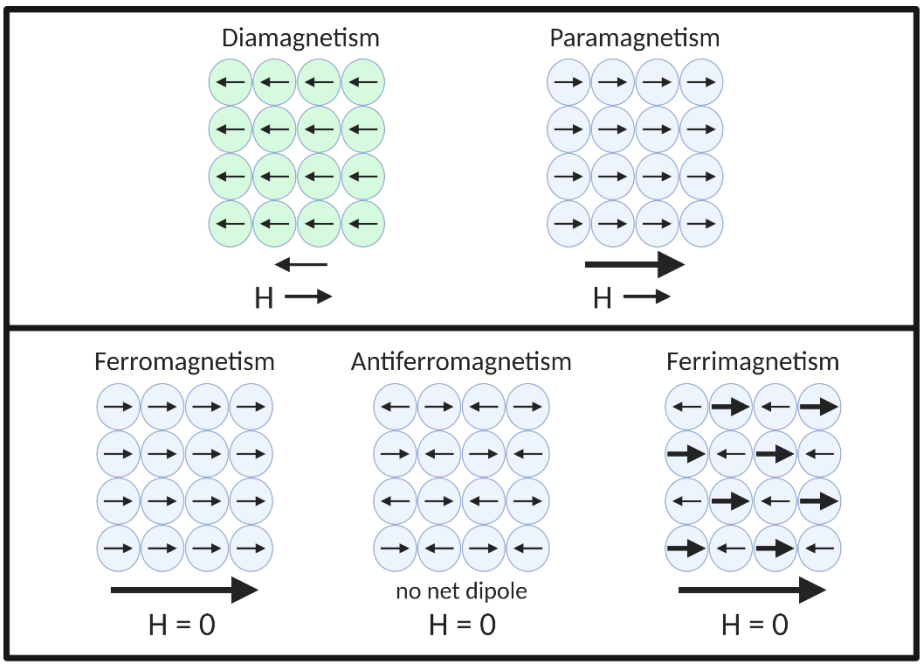

Figure 1.1. Depictions of the types of magnetism: Diamagnetism is the alignment of orbital motion opposite an applied magnetic field. Paramagnets have randomized spins at no field but will weakly align with an applied magnetic field. Ferromagnetism is when the spins are aligned, even at zero field, creating a permanent magnetic effect. Antiferromagnetism has antiparallel, generating a net zero magnetization. Ferrimagnetism has the spin ordering of antiferromagnetism, but with unequal magnitudes, resulting in a net overall magnetic moment.

All materials are diamagnetic in that the orbital motion of electrons will align opposite a magnetic field. This response however, is weakly repulsive and will be overpowered by other magnetic behaviors present.[25] Purely diamagnetic materials have fully paired electrons, resulting in a net cancellation of magnetic moments due to spin motion.[25] The four other magnetic behaviors are the result of unpaired valence electrons and are therefore most commonly observed in metal cations.[40] The electron spins in paramagnets have no long-range ordering, but will weakly align in the presence of a magnetic field.[25] In ferromagnets, the magnetic moments of each atom are of equal strength and are all aligned in parallel.[25] Furthermore, this alignment remains in the absence of a magnetic field, creating permanent magnetization. Antiferromagnetism is observed in materials with atomic magnetic moments of equal magnitude

but in opposing directions, generating a net zero magnetization.[25] Ferrimagnetism is similar to antiferromagnetism in that the magnetic moments of atoms are in opposing directions, but the magnitudes in a ferrimagnet are not the same.[25] These unequal magnitudes of spin result in an observed overall magnetic effect akin to ferromagnetism. Prominent examples of ferrimagnets featured in this dissertation include magnetite and ferrites.

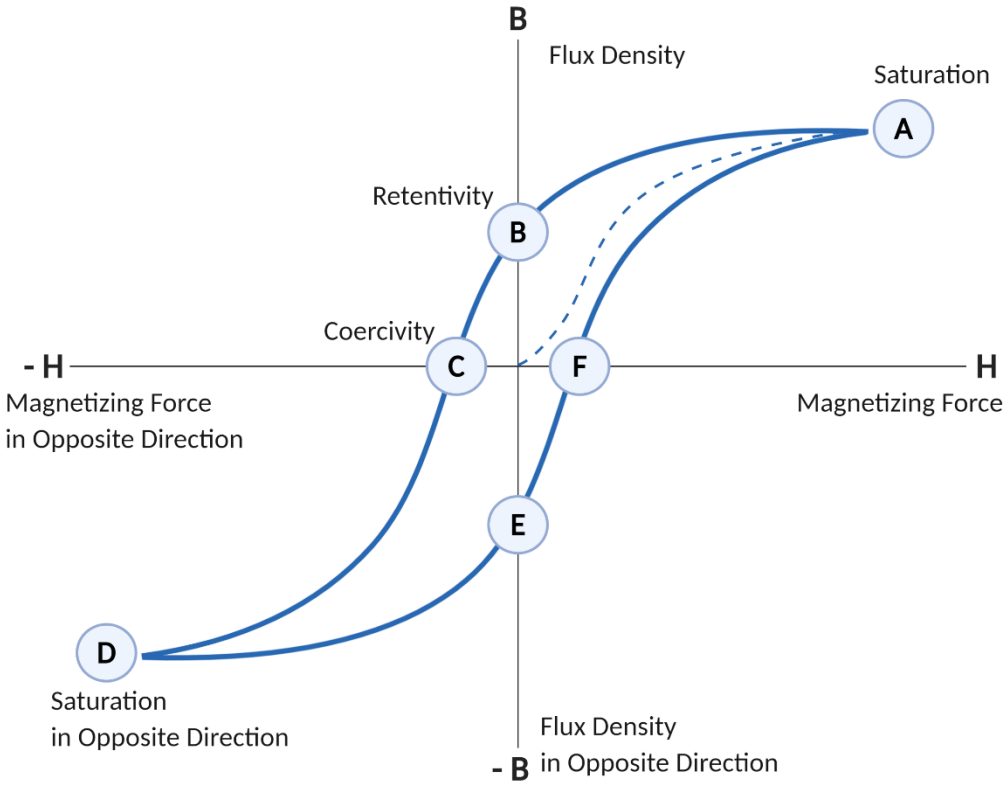

Figure 1.2. Magnetic hysteresis loop showing a) saturation, b) retentivity, and c) coercivity.

Magnetic material are evaluated by a variety of different terms and symbols which can best be understood by looking at a magnetic hysteresis loop. A magnetic hysteresis loop (Figure 1.2) plots the magnetic flux density (*B*) against magnetic field (*H*). Magnetic flux density is

defined as the density of lines of force and object experiences when placed in a magnetic field, and it is related to H by the permeability (μ), as seen in Equation 1.[40]

$$(1)\ B = \mu H$$

As mentioned previously, the magnetic moment is the strength and orientation of a magnetic object. The saturation magnetization is the maximum magnetization (M), which is the density of a magnetic moment per unit volume, achievable in an applied field. Magnetic susceptibility (χ) is defined as magnetization per field strength (M/H); it is a measure of the response a sample has to an applied magnetic field.[40] Magnetic permeability is the magnetic flux density per field strength (B/H) and is demonstrated by the slope at zero field. Coercivity is the magnetic field required to remove remnant magnetization from a magnetic and retentivity is flux density retained. The hysteresis loop shown in Figure 1.2 is representative of a typical ferromagnetic or ferrimagnetic material as there is a retained magnetization due to the permanent magnetic moment. The magnetic nanoparticles discussed in Chapter 2 are designed to be superparamagnetic manganese-zinc ferrite nanoparticles, meaning they should have no coercivity, high magnetic susceptibility, and high magnetic saturation.

As mentioned previously, nanomaterials often have enhanced properties compared to their bulk counterpart.[1,2] Superparamagnetism is a magnetic phenomenon observed at the nanoscale; particles below 20 nm have no coercivity but high magnetic moments.[25] When magnetic nanoparticles are below 20 nm, only a single magnetic domain is observed.[25,41] Particles now behave as a single paramagnetic atom, as there is no longer any coercivity, but with an enormous magnetic moment, as the magnetic ordering is still well-defined.[25] Because they respond so strongly to an external magnetic field but do not retain any remnant magnetization that could lead to aggregation, superparamagnetic nanoparticles are an ideal

material for biological applications.[24,37] In Chapter 2, ferrite nanoparticles with an observed superparamagnetic response are synthesized by reducing their diameter to 10 nm.

1.2.2 Magnetic Ferrite Nanoparticles

The magnetic behavior of ferrite nanoparticles is controlled not only by their diameter, but by the arrangement of the ions within its crystal lattice as well. Ferrites exhibit ferrimagnetism because of their mixed spinel structure. Spinels are a cubic close-packed arrangement of the formula MFe_2O_4 where M is a II cation and Fe is a III cation.[25,40] A general spinel crystal lattice can be seen in Figure 1.3, however, the way cations arrange themselves within this lattice determines what kind of spinel the material is. All spinels have eight tetrahedral (A site; binds to four oxygen atoms) and sixteen octahedral (B site; binds to six oxygen atoms). In a normal spinel, all eight of the A sites filled with II cations and all sixteen B sites are filled with III cations. Inverse spinels have their A sites filled with III cations and the remaining eight III cations and all II cations fill the B sites. Finally, in mixed spinels, II and III cations are dispersed equally among the A and B sites. Magnetically, the A and B sites create two separate sublattices that are aligned antiparallel from one another. As there are twice as many atoms within the B sublattice, there is an overall magnetic moment favoring the B sites.[25,41] In Chapter 2, we specifically designed a ferrite doped with both manganese and zinc cations. Manganese ferrites have higher magnetic susceptibilities than most ferrites,[34,42] and diamagnetic zinc favor tetrahedral A sites, reducing the antiferromagnetic coupling between the two lattices and increasing the overall magnetic moment.[25,43]

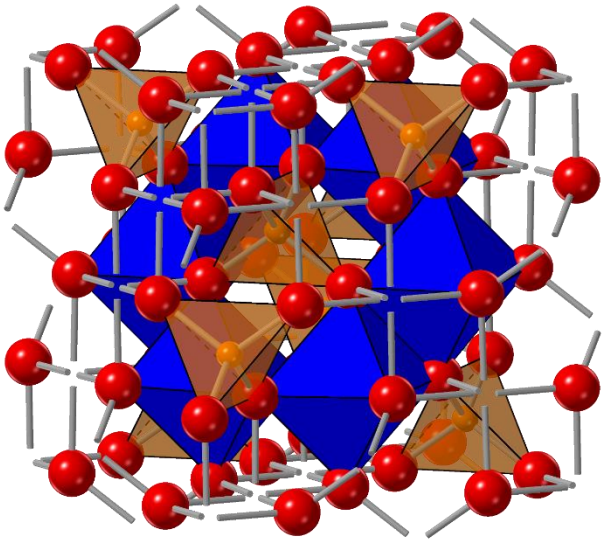

Figure 1.3. A spinel structure showing the ions in tetrahedral holes (orange) with the tetrahedral shape filled in, the ions in octahedral holes (blue), and the oxygen ions (red). Modeled in Crystal Maker.

1.3 LSPR in Metal Oxide Nanostructures

Because of their strong spectral properties, materials that exhibit localized surface plasmon resonance (LSPR) have found applications in biological sensors,[27,44–46] immunoassay labels,[47–49] optical switches,[50–52] and waveguides.[53,54] Fabricating LSPR nanostructures out of metal oxide materials offers more flexibility as the resonance can be tuned to meet specific application needs by composition, independent of the size and arrangement.[55] Additionally, these resonances occur in the near infrared (NIR), allowing plasmonic metal oxide nanostructures to have applications as energy efficient smart windows or in solar energy collection.[55,56] Chapter 3 explores the fabrication and modification of different WO_3 nanostructures to explore tunable LSPR in the NIR for improved light-based sensing devices. Several nanostructured arrays including nanowire, nanoring, and diffraction gratings were successfully fabricated using WO_3. Although the nanostructures presented do not possess strong resonances, the methods developed

were successfully incorporated into diffraction gratings with enhanced electrodiffraction from nanostructured ZnO.[57]

1.3.1 Localized Surface Plasmon Resonance Theory

LSPR is a spectroscopic phenomenon characterized by sharp absorbance or scattering peaks.[27] The phenomenon occurs when a plasmon, defined as the collective oscillations of delocalized electrons, is excited by electromagnetic radiation.[27,55] The plasmon is often visualized as an electric field causing mechanical oscillations of the electron cloud around a fixed metal core (Figure 1.4).

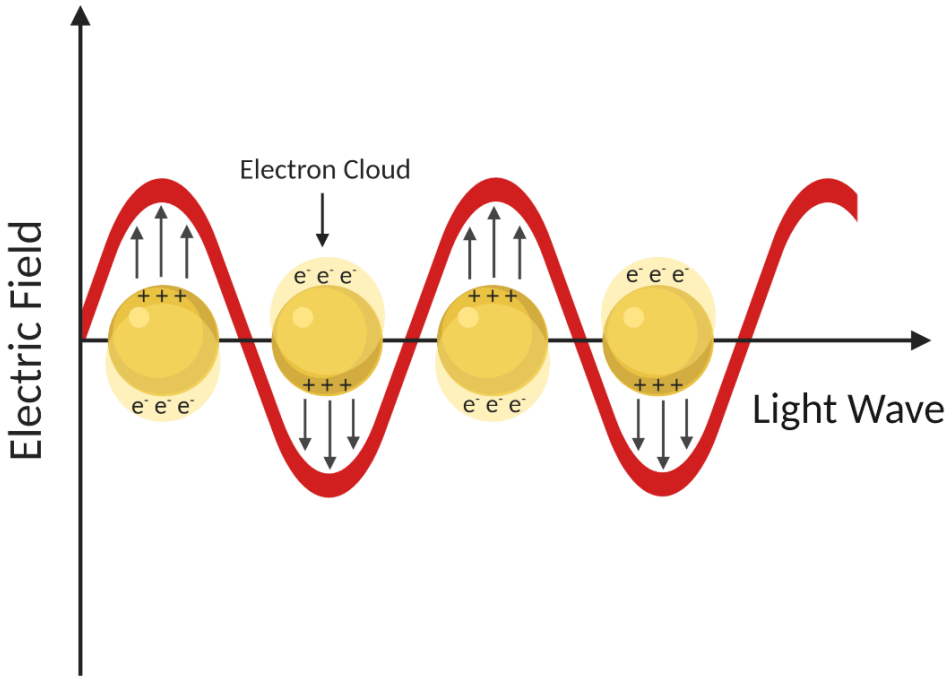

Figure 1.4. Graphic representation demonstrating localized surface plasmon resonance of a nanoparticle.

As this plasmon response is confined to particles or structures of subwavelength dimensions, it is termed a localized surface plasmon (LSP).[27] When a nanoparticle exhibits LSP behavior, the optical extinction is maximum at the plasmon resonant frequency,[44] making LSPR materials the

powerful spectral tool they are today. A localized surface plasmon resonant nanoparticle scatters and absorbs light so strongly, a single nanoparticle can be visualized using dark-field[44] or near-infrared[58] microscopy. As LSPR is a nanoscale phenomenon, the frequency at which a plasmon resonates is highly dependent on the structure's size and shape.[44] For example, the resonant frequency of a gold nanosphere can be tuned over 60 nm through changes in its diameter between 10 and 100 nm.[59] In another study by Mock et al, silver nanoparticles of the same volume but different shapes were demonstrated to have a wide range of resonances throughout the visible spectrum depending if they were spheres (blue), pentagons (green), or triangles (red).[60] Composition also plays an important role as this phenomenon is most commonly observed in nobel metals due to their large densities of free carriers and appears mostly in the visible region.[27] However, LSPR can also be observed in the NIR by doping metal oxides, such as electrochromic WO_3.

Metal oxides like tungsten oxide (WO_3) can be tuned to produce localized surface plasmon resonance (LSPR) by doping in charge carriers.[44,55] The main method for controlling plasmonic resonance within WO_3 nanostructures is through oxygen deficiencies within the crystal lattice.[28,61] Oxygen deficient tungsten trioxide ($WO_{3-\delta}$, where δ is > 0.1) undergoes a metal-insulator transition when $\delta = 0.1$, and takes on a more metallic character.[28,62] By altering δ, different resonances can be observed and tuned to give NIR signal. In Chapter 3, we tested several post-fabrication modification techniques, including furnace reduction and MoO_3 doping, to create permanent reduced states within the WO_3 crystal lattice.

1.3.2 Electrochromic Metal Oxides

The optical properties of electrochromic materials can be reversibly tuned through the application of an electrical potential.[56,63] This unique control over absorbance, transmittance, and reflectivity has made electrochromic materials have shown promise as optical energy saving devices,[64,65] sensors,[66] batteries,[67,68] and display materials.[69–71] Tungsten oxide (WO_3), has been one of the most prominently researched metal oxides because of its ideal electrochromic properties – high coloration efficiencies, stability, good electron transport efficiencies, and stability in aqueous solutions.[56,72–74] As illustrated in Figure 1.5 and Equation 2, insertion of electrons and charge balancing cations, M^+, causes a WO_3 film, electrodeposited on ITO glass, to change from transparent to a deep blue.[74,75] The M^+ ion is most commonly H^+ or Li^+ ions, but in fact can be any cation that will intercalate within the WO_3 lattice.

$$(2)\quad W^{VI}O_3 + xM^+ + xe^- \leftrightarrow M_xW_{(1-x)}{}^{VI}W_x{}^{V}O_3$$

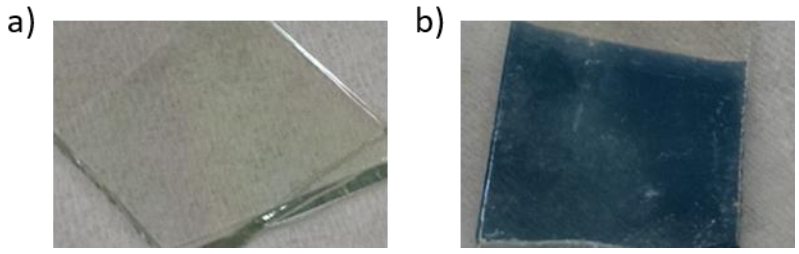

Figure 1.5 Images demonstrating the electrochromic behavior of a WO_3 thin film. The film is observed to change from transparent in its fully oxidized to colored, blue in this case, when reduced. Lithium intercalation is a common reduction technique, but reduction can occur through oxygen vacancies.

Fully oxidized WO_3 has a full O2*p* band and empty *d* band wide enough apart such that it appears transparent. The smallest addition of M^+ ions and charge balancing electrons will reduce tungsten ions from VI to V and partially fill the *d* band, resulting in an optical absorption such that WO_3 appears blue.[76–78]

1.4 DNA-Nanogold Conjugates

Just as nanoparticles display fascinating properties different from bulk materials, nanoparticles assembled into 2D arrays and 3D shapes can display new electronic, magnetic, and optical properties different from individual samples and bulk materials.[1] With these new properties come new applications for ensembles of nanoparticles in electronic, memory, and optical devices.[31,79,80] A recent development in achieving absolute control over ensemble design is the use of sequence-specific DNA bonds to direct the placement of each nanoparticle component within a structure.[81,82] The DNA nucleobases' have sufficient affinity for a gold surface for oligonucleotides to wrap themselves around gold nanoparticles in a random fashion.[83,84] However, attaching a thiol moiety to the end of a DNA strand will orient the nucleotide perpendicular to the nanoparticle surface, which is a more flexible configuration for further hybridization over random attachment.[83] The resulting motif of these "programmable materials" can reliably be predicted through the specific design of DNA hybridization.[31,83] DNA directed nanoparticle designs include linear arrays,[85,86] 2D arrays,[31,87] 3D lattices,[88–90] and tripods.[91] To better understand how to control and take advantage of DNA-mediated assemblies of gold nanoparticles, it is of the utmost importance to understand the structure of the DNA-gold interaction.[79] Structural information of flexible heterogeneous samples like DNA-gold conjugates is difficult to obtain from characterization techniques like X-ray crystallography.[79] The final portion of this thesis, Chapter 4, presents our progress in developing improved methodologies to structurally characterize DNA-gold interactions of smaller masses. In Chapter 4, 1.4 nm nanogold was bound to 60 base-pair thiol-modified DNA strands, purified, and then analyzed through cryo-electron microscopy.

1.5 Cryo-Electron Microscopy

Cryo-electron microscopy (EM) has revolutionized biological and chemical fields with its ability to visualize biological samples with a resolution as far down as 2 Å.[92] Although X-ray crystallography is, and will continue to be, an effective tool to produce atomic models, it comes with limitations.[93] Samples that cannot be isolated in sufficient quantity or do not readily produce crystals, such as membrane proteins or polymers, cannot be analyzed by crystallographic methods.[93,94] With the development of cryo-EM, a variety of biological samples including viruses,[95,96] ribosomes,[97] enzymes,[98,99] and most importantly for the purpose of this dissertation, DNA.[79,100] In particular, cyro-EM has been used to reconstruct the structures of DNA arrangements of 10 nm gold particles.[101,102] Additionally, the 3D structure of hybridized DNA-nanogold conjugates have been successfully reconstructed using a combination of negative-staining, individual-particle electron tomography, and cryo-EM.[79]

Electron microscopes have been imaging inorganic samples since the 1930s, but it has taken decades of design modification and technological improvement for biological samples to be images by electron microscopes and then reconstructed.[103] The electron microscope operates similar to the traditional light microscope but is able to bypass the diffraction limit of light microscopy using an electron source to image subwavelength objects.[104] The EM apparatus and sample must be under vacuum to circumvent strong electron scattering that occurs in air and can disrupt imaging quality.[103] This is problematic for biological samples like oligonucleotides and proteins, whose structure is only accurate in an aqueous environment and cannot be put under vacuum.[94] Furthermore, many biological samples are beam sensitive materials that are easily damaged upon irradiation by the electron beam.[92,105] High vacuum and radiation damage of electron microscopes significantly reduce the quality of imaging oligonucleotides accurately,

however biological samples that are frozen in vitreous ice before imaging address these issues.[106,107] The vitrification process, developed by Dubochet and colleagues begins with a small amount of sample applied to an EM grid covered in a holey carbon film.[108] Next, the grid is blotted with filter paper to remove excess solution so that only a thin liquid layer remains across the holes in the carbon film.[92] Finally, the sample is plunged into a liquid nitrogen-cooled pool of liquid ethane or propane, which with today's technological advances, can now be performed using an automatic "plunge-freezer" machine to produce a faster plunge and results in a better ice layer which is critical for imaging in cryo-EM.[92] Although trapped in a vitrified layer of ice, multiple samples have been demonstrated to preserve their native structure and have been imaged accurately at low doses (~400 $e^-/Å^2$) without fear of dehydration from vacuum or radiation damage.[92,107,109] The image generated by the detector is a 2D projection that corresponds to the structure in the path of the electron beam.[94] To generate a 3D structure of the sample with atomic level resolution, large ensembles of sample must imaged such that all possible orientations are found.[92,103,110,111] By classifying the images into groups based on orientation, aligning, and then refining them, a Coulomb potential density map is slowly assembled, revealing structural details about the sample.[92]

1.6 References

(1) Nie, Z.; Petukhova, A.; Kumacheva, E. Properties and Emerging Applications of Self-Assembled Structures Made from Inorganic Nanoparticles. *Nat. Nanotechnol.* **2010**, *5* (1), 15–25.

(2) Biacchi, A. J.; Schaak, R. E. Ligand-Induced Fate of Embryonic Species in the Shape-Controlled Synthesis of Rhodium Nanoparticles. *ACS Nano* **2015**, *9* (2), 1707–1720.

(3) Khlebtsov, N. G. Determination of Size and Concentration of Gold Nanoparticles from Extinction Spectra. *Anal. Chem.* **2008**, *80* (17), 6620–6625.

(4) Wang, L.; Clavero, C.; Huba, Z.; Carroll, K. J.; Carpenter, E. E.; Gu, D.; Lukaszew, R. A. Plasmonics and Enhanced Magneto-Optics in Core−Shell Co−Ag Nanoparticles. *Nano Lett.* **2011**, *11* (3), 1237–1240.

(5) Brannon-Peppas, L.; Blanchette, J. O. Nanoparticle and Targeted Systems for Cancer Therapy. *Adv. Drug Deliv. Rev.* **2004**, *56* (11), 1649–1659.

(6) Hergt, R.; Dutz, S.; Müller, R.; Zeisberger, M. Magnetic Particle Hyperthermia: Nanoparticle Magnetism and Materials Development for Cancer Therapy. *J. Phys. Condens. Matter* **2006**, *18* (38), S2919–S2934.

(7) Shi, J.; Kantoff, P. W.; Wooster, R.; Farokhzad, O. C. Cancer Nanomedicine: Progress, Challenges and Opportunities. *Nat. Rev. Cancer* **2016**, *17*, 20.

(8) Huang, D.; Liao, F.; Molesa, S.; Redinger, D.; Subramanian, V. Plastic-Compatible Low Resistance Printable Gold Nanoparticle Conductors for Flexible Electronics. *J. Electrochem. Soc.* **2003**, *150* (7), G412–G417.

(9) Kang, J. S.; Kim, H. S.; Ryu, J.; Thomas Hahn, H.; Jang, S.; Joung, J. W. Inkjet Printed Electronics Using Copper Nanoparticle Ink. *J. Mater. Sci. Mater. Electron.* **2010**, *21* (11), 1213–1220.

(10) Raschke, G.; Brogl, S.; Susha, A. S.; Rogach, A. L.; Klar, T. A.; Feldmann, J.; Fieres, B.; Petkov, N.; Bein, T.; Nichtl, A.; et al. Gold Nanoshells Improve Single Nanoparticle Molecular Sensors. *Nano Lett.* **2004**, *4* (10), 1853–1857.

(11) Peng, J.; He, X.; Wang, K.; Tan, W.; Wang, Y.; Liu, Y. Noninvasive Monitoring of Intracellular PH Change Induced by Drug Stimulation Using Silica Nanoparticle Sensors. *Anal. Bioanal. Chem.* **2007**, *388* (3), 645–654.

(12) You, C.-C.; Miranda, O. R.; Gider, B.; Ghosh, P. S.; Kim, I.-B.; Erdogan, B.; Krovi, S. A.; Bunz, U. H. F.; Rotello, V. M. Detection and Identification of Proteins Using Nanoparticle–Fluorescent Polymer 'Chemical Nose' Sensors. *Nat. Nanotechnol.* **2007**, *2* (5), 318–323.

(13) Rolison, D. R.; Long, J. W.; Lytle, J. C.; Fischer, A. E.; Rhodes, C. P.; McEvoy, T. M.; Bourg, M. E.; Lubers, A. M. Multifunctional 3D Nanoarchitectures for Energy Storage and Conversion. *Chem. Soc. Rev.* **2009**, *38* (1), 226–252.

(14) Xia, H.; Feng, J.; Wang, H.; Lai, M. O.; Lu, L. MnO2 Nanotube and Nanowire Arrays by Electrochemical Deposition for Supercapacitors. *J. Power Sources* **2010**, *195* (13), 4410–4413.

(15) Shir, D.; Yoon, J.; Chanda, D.; Ryu, J.-H.; Rogers, J. A. Performance of Ultrathin Silicon Solar Microcells with Nanostructures of Relief Formed by Soft Imprint Lithography for Broad Band Absorption Enhancement. *Nano Lett.* **2010**, *10* (8), 3041–3046.

(16) Reiss, G.; Hütten, A. Applications beyond Data Storage. *Nat. Mater.* **2005**, *4* (10), 725–726.

(17) Ethirajan, A.; Wiedwald, U.; Boyen, H.-G.; Kern, B.; Han, L.; Klimmer, A.; Weigl, F.; Kästle, G.; Ziemann, P.; Fauth, K.; et al. A Micellar Approach to Magnetic Ultrahigh-Density Data-Storage Media: Extending the Limits of Current Colloidal Methods. *Adv. Mater.* **2007**, *19* (3), 406–410.

(18) Blanco, E.; Shen, H.; Ferrari, M. Principles of Nanoparticle Design for Overcoming Biological Barriers to Drug Delivery. *Nat. Biotechnol.* **2015**, *33*, 941.

(19) Singh, R.; Lillard, J. W. Nanoparticle-Based Targeted Drug Delivery. *Exp. Mol. Pathol.* **2009**, *86* (3), 215–223.

(20) Amoozgar, Z.; Yeo, Y. Recent Advances in Stealth Coating of Nanoparticle Drug Delivery Systems. *Wiley Interdiscip. Rev. Nanomedicine Nanobiotechnology* **2012**, *4* (2), 219–233.

(21) Holzinger, M.; Le Goff, A.; Cosnier, S. Nanomaterials for Biosensing Applications: A Review. *Frontiers in Chemistry*. **2014**, p 63.

(22) Ding, L.; Bond, A. M.; Zhai, J.; Zhang, J. Utilization of Nanoparticle Labels for Signal Amplification in Ultrasensitive Electrochemical Affinity Biosensors: A Review. *Anal. Chim. Acta* **2013**, *797*, 1–12.

(23) Qiao, L.; Fu, Z.; Li, J.; Ghosen, J.; Zeng, M.; Stebbins, J.; Prasad, P. N.; Swihart, M. T. Standardizing Size- and Shape-Controlled Synthesis of Monodisperse Magnetite (Fe3O4) Nanocrystals by Identifying and Exploiting Effects of Organic Impurities. *ACS Nano* **2017**, *11* (6), 6370–6381.

(24) Sun, S.; Zeng, H.; Robinson, D. B.; Raoux, S.; Rice, P. M.; Wang, S. X.; Li, G. Monodisperse MFe2O4 (M = Fe, Co, Mn) Nanoparticles. *J. Am. Chem. Soc.* **2004**, *126* (1), 273–279.

(25) Mathew, D. S.; Juang, R.-S. An Overview of the Structure and Magnetism of Spinel Ferrite Nanoparticles and Their Synthesis in Microemulsions. *Chem. Eng. J.* **2007**, *129* (1), 51–65.

(26) Andreu, I.; Natividad, E.; Solozábal, L.; Roubeau, O. Nano-Objects for Addressing the Control of Nanoparticle Arrangement and Performance in Magnetic Hyperthermia. *ACS Nano* **2015**, *9* (2), 1408–1419.

(27) Mayer, K. M.; Hafner, J. H. Localized Surface Plasmon Resonance Sensors. *Chem. Rev.* **2011**, *111* (6), 3828–3857.

(28) Mattox, T. M.; Bergerud, A.; Agrawal, A.; Milliron, D. J. Influence of Shape on the Surface Plasmon Resonance of Tungsten Bronze Nanocrystals. *Chem. Mater.* **2014**, *26* (5), 1779–1784.

(29) Lee, K.-S.; El-Sayed, M. A. Gold and Silver Nanoparticles in Sensing and Imaging: Sensitivity of Plasmon Response to Size, Shape, and Metal Composition. *J. Phys. Chem. B* **2006**, *110* (39), 19220–19225.

(30) Park, S. Y.; Lytton-Jean, A. K. R.; Lee, B.; Weigand, S.; Schatz, G. C.; Mirkin, C. A. DNA-Programmable Nanoparticle Crystallization. *Nature* **2008**, *451* (7178), 553–556.

(31) Zheng, J.; Constantinou, P. E.; Micheel, C.; Alivisatos, A. P.; Kiehl, R. A.; Seeman, N. C. Two-Dimensional Nanoparticle Arrays Show the Organizational Power of Robust DNA Motifs. *Nano Lett.* **2006**, *6* (7), 1502–1504.

(32) Mornet, S.; Vasseur, S.; Grasset, F.; Duguet, E. Magnetic Nanoparticle Design for Medical Diagnosis and Therapy. *J. Mater. Chem.* **2004**, *14* (14), 2161–2175.

(33) Yang, H.; Zhang, C.; Shi, X.; Hu, H.; Du, X.; Fang, Y.; Ma, Y.; Wu, H.; Yang, S. Water-Soluble Superparamagnetic Manganese Ferrite Nanoparticles for Magnetic Resonance Imaging. *Biomaterials* **2010**, *31* (13), 3667–3673.

(34) Karimi, Z.; Karimi, L.; Shokrollahi, H. Nano-Magnetic Particles Used in Biomedicine: Core and Coating Materials. *Mater. Sci. Eng. C* **2013**, *33* (5), 2465–2475.

(35) Wang, S. X.; Li, G. Advances in Giant Magnetoresistance Biosensors With Magnetic Nanoparticle Tags: Review and Outlook. *IEEE Trans. Magn.* **2008**, *44* (7), 1687–1702.

(36) Nikitin, P. I.; Vetoshko, P. M.; Ksenevich, T. I. New Type of Biosensor Based on Magnetic Nanoparticle Detection. *J. Magn. Magn. Mater.* **2007**, *311* (1), 445–449.

(37) Dai, Q.; Berman, D.; Virwani, K.; Frommer, J.; Jubert, P.-O.; Lam, M.; Topuria, T.; Imaino, W.; Nelson, A. Self-Assembled Ferrimagnet−Polymer Composites for Magnetic Recording Media. *Nano Lett.* **2010**, *10* (8), 3216–3221.

(38) Calvin, S.; Carpenter, E. E.; Ravel, B.; Harris, V. G.; Morrison, S. A. Multiedge Refinement of Extended X-Ray-Absorption Fine Structure of Manganese Zinc Ferrite Nanoparticles. *Phys. Rev. B* **2002**, *66* (22), 224405.

(39) Zhang, T.; Ge, J.; Hu, Y.; Yin, Y. A General Approach for Transferring Hydrophobic Nanocrystals into Water. *Nano Lett.* **2007**, *7* (10), 3203–3207.

(40) West, A. R. *Solid State Chemistry and Its Applications*, 2nd ed.; John Wiley & Sons, Ltd.: Chichester, West Sussex, United Kingdom, 2014.

(41) Kodama, R. H. Magnetic Nanoparticles. *J. Magn. Magn. Mater.* **1999**, *200* (1), 359–372.

(42) Lee, J.-H.; Huh, Y.-M.; Jun, Y.; Seo, J.; Jang, J.; Song, H.-T.; Kim, S.; Cho, E.-J.; Yoon, H.-G.; Suh, J.-S.; et al. Artificially Engineered Magnetic Nanoparticles for Ultra-Sensitive Molecular Imaging. *Nat. Med.* **2007**, *13* (1), 95–99.

(43) Makovec, D.; Kodre, A.; Arčon, I.; Drofenik, M. Structure of Manganese Zinc Ferrite Spinel Nanoparticles Prepared with Co-Precipitation in Reversed Microemulsions. *J. Nanoparticle Res.* **2009**, *11* (5), 1145–1158.

(44) Anker, J. N.; Hall, W. P.; Lyandres, O.; Shah, N. C.; Zhao, J.; Van Duyne, R. P. Biosensing with Plasmonic Nanosensors. *Nat. Mater.* **2008**, *7* (6), 442–453.

(45) Dahlin, A. B.; Tegenfeldt, J. O.; Höök, F. Improving the Instrumental Resolution of Sensors Based on Localized Surface Plasmon Resonance. *Anal. Chem.* **2006**, *78* (13), 4416–4423.

(46) Yoo, S. Y.; Kim, D.-K.; Park, T. J.; Kim, E. K.; Tamiya, E.; Lee, S. Y. Detection of the Most Common Corneal Dystrophies Caused by BIGH3 Gene Point Mutations Using a Multispot Gold-Capped Nanoparticle Array Chip. *Anal. Chem.* **2010**, *82* (4), 1349–1357.

(47) Mayer, K. M.; Lee, S.; Liao, H.; Rostro, B. C.; Fuentes, A.; Scully, P. T.; Nehl, C. L.; Hafner, J. H. A Label-Free Immunoassay Based Upon Localized Surface Plasmon Resonance of Gold Nanorods. *ACS Nano* **2008**, *2* (4), 687–692.

(48) Chen, S.; Svedendahl, M.; Käll, M.; Gunnarsson, L.; Dmitriev, A. Ultrahigh Sensitivity Made Simple: Nanoplasmonic Label-Free Biosensing with an Extremely Low Limit-of-Detection for Bacterial and Cancer Diagnostics. *Nanotechnology* **2009**, *20* (43), 434015.

(49) Nam, J.-M.; Thaxton, C. S.; Mirkin, C. A. Nanoparticle-Based Bio-Bar Codes for the Ultrasensitive Detection of Proteins. *Science (80-.).* **2003**, *301* (5641), 1884 LP – 1886.

(50) Large, N.; Abb, M.; Aizpurua, J.; Muskens, O. L. Photoconductively Loaded Plasmonic Nanoantenna as Building Block for Ultracompact Optical Switches. *Nano Lett.* **2010**, *10* (5), 1741–1746.

(51) Maksymov, I. S. Optical Switching and Logic Gates with Hybrid Plasmonic–Photonic Crystal Nanobeam Cavities. *Phys. Lett. A* **2011**, *375* (5), 918–921.

(52) Maier, S. A.; Brongersma, M. L.; Kik, P. G.; Meltzer, S.; Requicha, A. A. G.; Atwater, H. A. Plasmonics—A Route to Nanoscale Optical Devices. *Adv. Mater.* **2001**, *13* (19), 1501–1505.

(53) Oulton, R. F.; Sorger, V. J.; Genov, D. A.; Pile, D. F. P.; Zhang, X. A Hybrid Plasmonic Waveguide for Subwavelength Confinement and Long-Range Propagation. *Nat. Photonics* **2008**, *2* (8), 496–500.

(54) Brongersma, M. L.; Hartman, J. W.; Atwater, H. A. Electromagnetic Energy Transfer and Switching in Nanoparticle Chain Arrays below the Diffraction Limit. *Phys. Rev. B* **2000**, *62* (24), R16356–R16359.

(55) Agrawal, A.; Johns, R. W.; Milliron, D. J. Control of Localized Surface Plasmon Resonances in Metal Oxide Nanocrystals. *Annu. Rev. Mater. Res.* **2017**, *47* (1), 1–31.

(56) Niklasson, G. A.; Granqvist, C. G. Electrochromics for Smart Windows: Thin Films of Tungsten Oxide and Nickel Oxide, and Devices Based on These. *J. Mater. Chem.* **2007**, *17* (2), 127–156.

(57) Fung, H. W. M.; So, S.; Kartub, K.; Corn, R. M. Quantitative Characterization of Optical Coupling in Nanoporous ZnO–WO3 and ZnO–PEDOT Composite Electrodeposited Gratings Using Electrodiffraction Measurements. *J. Phys. Chem. C* **2019**, *123* (1), 762–769.

(58) Halpern, A. R.; Wood, J. B.; Wang, Y.; Corn, R. M. Single-Nanoparticle Near-Infrared Surface Plasmon Resonance Microscopy for Real-Time Measurements of DNA Hybridization Adsorption. *ACS Nano* **2014**, *8* (1), 1022–1030.

(59) Link, S.; El-Sayed, M. A. Spectral Properties and Relaxation Dynamics of Surface Plasmon Electronic Oscillations in Gold and Silver Nanodots and Nanorods. *J. Phys. Chem. B* **1999**, *103* (40), 8410–8426.

(60) Mock, J. J.; Barbic, M.; Smith, D. R.; Schultz, D. A.; Schultz, S. Shape Effects in Plasmon Resonance of Individual Colloidal Silver Nanoparticles. *J. Chem. Phys.* **2002**, *116* (15), 6755–6759.

(61) Manthiram, K.; Alivisatos, A. P. Tunable Localized Surface Plasmon Resonances in Tungsten Oxide Nanocrystals. *J. Am. Chem. Soc.* **2012**, *134* (9), 3995–3998.

(62) Viswanathan, K.; Brandt, K.; Salje, E. Crystal Structure and Charge Carrier Concentration of W18O49. *J. Solid State Chem.* **1980**, *33* (3), 441–442.

(63) Somani, P. R.; Radhakrishnan, S. Electrochromic Materials and Devices: Present and Future. *Mater. Chem. Phys.* **2003**, *77* (1), 117–133.

(64) Xie, Z.; Jin, X.; Chen, G.; Xu, J.; Chen, D.; Shen, G. Integrated Smart Electrochromic Windows for Energy Saving and Storage Applications. *Chem. Commun.* **2014**, *50* (5), 608–610.

(65) Azens, A.; Granqvist, C. Electrochromic Smart Windows: Energy Efficiency and Device Aspects. *J. Solid State Electrochem.* **2003**, *7* (2), 64–68.

(66) Klymchenko, A. S.; Demchenko, A. P. Electrochromic Modulation of Excited-State Intramolecular Proton Transfer: The New Principle in Design of Fluorescence Sensors. *J. Am. Chem. Soc.* **2002**, *124* (41), 12372–12379.

(67) Xia, X.; Ku, Z.; Zhou, D.; Zhong, Y.; Zhang, Y.; Wang, Y.; Huang, M. J.; Tu, J.; Fan, H. J. Perovskite Solar Cell Powered Electrochromic Batteries for Smart Windows. *Mater. Horizons* **2016**, *3* (6), 588–595.

(68) Astruc, D.; Ornelas, C.; Ruiz, J. Dendritic Molecular Electrochromic Batteries Based on Redox-Robust Metallocenes. *Chem. – A Eur. J.* **2009**, *15* (36), 8936–8944.

(69) Mortimer, R. J.; Dyer, A. L.; Reynolds, J. R. Electrochromic Organic and Polymeric Materials for Display Applications. *Displays* **2006**, *27* (1), 2–18.

(70) Krebs, F. C. The New Black. *Nat. Mater.* **2008**, *7* (10), 766–767.

(71) Bonhôte, P.; Gogniat, E.; Campus, F.; Walder, L.; Grätzel, M. Nanocrystalline Electrochromic Displays. *Displays* **1999**, *20* (3), 137–144.

(72) Wang, F.; Di Valentin, C.; Pacchioni, G. Electronic and Structural Properties of WO3: A Systematic Hybrid DFT Study. *J. Phys. Chem. C* **2011**, *115* (16), 8345–8353.

(73) Vuong, N. M.; Kim, D.; Kim, H. Electrochromic Properties of Porous WO3–TiO2 Core–Shell Nanowires. *J. Mater. Chem. C* **2013**, *1* (21), 3399–3407.

(74) Wang, M.; Fang, G.; Yuan, L.; Huang, H.; Sun, Z.; Liu, N.; Xia, S.; Zhao, X. High Optical Switching Speed and Flexible Electrochromic Display Based on WO3nanoparticles with ZnO Nanorod Arrays' Supported Electrode. *Nanotechnology* **2009**, *20* (18), 185304.

(75) Granqvist, C.-G. Electrochromic Metal Oxides: An Introduction to Materials and Devices. *Electrochromic Materials and Devices*. September 28, 2013, pp 1–40.

(76) Granqvist, C. G. Electrochromics for Smart Windows: Oxide-Based Thin Films and Devices. *Thin Solid Films* **2014**, *564*, 1–38.

(77) Wang, Y.; Runnerstrom, E. L.; Milliron, D. J. Switchable Materials for Smart Windows. *Annu. Rev. Chem. Biomol. Eng.* **2016**, *7* (1), 283–304.

(78) Abe, O. O.; Jodhani, G.; Gouma, P. On the Coupled Ferroelectric-Electrochromic Effect of ε-WO3. *J. Am. Ceram. Soc.* **2018**, *101* (1), 12–15.

(79) Zhang, L.; Lei, D.; Smith, J. M.; Zhang, M.; Tong, H.; Zhang, X.; Lu, Z.; Liu, J.; Alivisatos, A. P.; Ren, G. Three-Dimensional Structural Dynamics and Fluctuations of DNA-Nanogold Conjugates by Individual-Particle Electron Tomography. *Nat. Commun.* **2016**, *7* (1), 11083.

(80) Elghanian, R.; Storhoff, J. J.; Mucic, R. C.; Letsinger, R. L.; Mirkin, C. A. Selective Colorimetric Detection of Polynucleotides Based on the Distance-Dependent Optical Properties of Gold Nanoparticles. *Science (80-.).* **1997**, *277* (5329), 1078 LP – 1081.

(81) Mirkin, C. A.; Letsinger, R. L.; Mucic, R. C.; Storhoff, J. J. A DNA-Based Method for Rationally Assembling Nanoparticles into Macroscopic Materials. *Nature* **1996**, *382* (6592), 607–609.

(82) Alivisatos, A. P.; Johnsson, K. P.; Peng, X.; Wilson, T. E.; Loweth, C. J.; Bruchez, M. P.; Schultz, P. G. Organization of "nanocrystal Molecules" Using DNA. *Nature* **1996**, *382* (6592), 609–611.

(83) Jones, M. R.; Seeman, N. C.; Mirkin, C. A. Programmable Materials and the Nature of the DNA Bond. *Science (80-.).* **2015**, *347* (6224), 1260901.

(84) Herne, T. M.; Tarlov, M. J. Characterization of DNA Probes Immobilized on Gold Surfaces. *J. Am. Chem. Soc.* **1997**, *119* (38), 8916–8920.

(85) Xiao, S.; Liu, F.; Rosen, A. E.; Hainfeld, J. F.; Seeman, N. C.; Musier-Forsyth, K.; Kiehl, R. A. Selfassembly of Metallic Nanoparticle Arrays by DNA Scaffolding. *J. Nanoparticle Res.* **2002**, *4* (4), 313–317.

(86) Le, J. D.; Pinto, Y.; Seeman, N. C.; Musier-Forsyth, K.; Taton, T. A.; Kiehl, R. A. DNA-Templated Self-Assembly of Metallic Nanocomponent Arrays on a Surface. *Nano Lett.* **2004**, *4* (12), 2343–2347.

(87) Shiraishi, S.; Yu, L.; Akiyama, Y.; Wang, G.; Kikitsu, T.; Miyamura, K.; Takarada, T.; Maeda, M. Folding of Nanoparticle Chains into 2D Arrays: Structural Change of DNA-Functionalized Gold Nanoparticle Assemblies. *Adv. Mater. Interfaces* **2018**, *5* (13), 1800189.

(88) Zhang, T.; Hartl, C.; Frank, K.; Heuer-Jungemann, A.; Fischer, S.; Nickels, P. C.; Nickel, B.; Liedl, T. 3D DNA Origami Crystals. *Adv. Mater.* **2018**, *30* (28), 1800273.

(89) Tian, Y.; Zhang, Y.; Wang, T.; Xin, H. L.; Li, H.; Gang, O. Lattice Engineering through Nanoparticle–DNA Frameworks. *Nat. Mater.* **2016**, *15*, 654.

(90) Ji, M.; Ma, N.; Tian, Y. 3D Lattice Engineering of Nanoparticles by DNA Shells. *Small* **2019**, *15* (26), 1805401.

(91) Zhan, P.; Dutta, P. K.; Wang, P.; Song, G.; Dai, M.; Zhao, S.-X.; Wang, Z.-G.; Yin, P.; Zhang, W.; Ding, B.; et al. Reconfigurable Three-Dimensional Gold Nanorod Plasmonic Nanostructures Organized on DNA Origami Tripod. *ACS Nano* **2017**, *11* (2), 1172–1179.

(92) Cheng, Y. Single-Particle Cryo-EM at Crystallographic Resolution. *Cell* **2015**, *161* (3), 450–457.

(93) Kühlbrandt, W. The Resolution Revolution. *Science (80-.).* **2014**, *343* (6178), 1443 LP – 1444.

(94) Nogales, E.; Scheres, S. H. W. Cryo-EM: A Unique Tool for the Visualization of Macromolecular Complexity. *Mol. Cell* **2015**, *58* (4), 677–689.

(95) Zhang, X.; Jin, L.; Fang, Q.; Hui, W. H.; Zhou, Z. H. 3.3 Å Cryo-EM Structure of a Nonenveloped Virus Reveals a Priming Mechanism for Cell Entry. *Cell* **2010**, *141* (3), 472–482.

(96) Yu, X.; Ge, P.; Jiang, J.; Atanasov, I.; Zhou, Z. H. Atomic Model of CPV Reveals the Mechanism Used by This Single-Shelled Virus to Economically Carry Out Functions Conserved in Multishelled Reoviruses. *Structure* **2011**, *19* (5), 652–661.

(97) Amunts, A.; Brown, A.; Toots, J.; Scheres, S. H. W.; Ramakrishnan, V. The Structure of the Human Mitochondrial Ribosome. *Science (80-.).* **2015**, *348* (6230), 95 LP – 98.

(98) Vinothkumar, K. R.; Zhu, J.; Hirst, J. Architecture of Mammalian Respiratory Complex I. *Nature* **2014**, *515*, 80.

(99) Bai, X.; Yan, C.; Yang, G.; Lu, P.; Ma, D.; Sun, L.; Zhou, R.; Scheres, S. H. W.; Shi, Y. An Atomic Structure of Human γ-Secretase. *Nature* **2015**, *525*, 212.

(100) Bai, X.; Martin, T. G.; Scheres, S. H. W.; Dietz, H. Cryo-EM Structure of a 3D DNA-Origami Object. *Proc. Natl. Acad. Sci.* **2012**, *109* (49), 20012 LP – 20017.

(101) Tian, Y.; Wang, T.; Liu, W.; Xin, H. L.; Li, H.; Ke, Y.; Shih, W. M.; Gang, O. Prescribed Nanoparticle Cluster Architectures and Low-Dimensional Arrays Built Using Octahedral DNA Origami Frames. *Nat. Nanotechnol.* **2015**, *10*, 637.

(102) Lermusiaux, L.; Funston, A. M. Plasmonic Isomers via DNA-Based Self-Assembly of Gold Nanoparticles. *Nanoscale* **2018**, *10* (41), 19557–19567.

(103) Egelman, E. H. The Current Revolution in Cryo-EM. *Biophys. J.* **2016**, *110* (5), 1008–1012.

(104) Zhou, W.; Apkarian, R. P.; Wang, Z. L.; Joy, D. *Scanning Microscopy for Nanotechnology*, 1st ed.; Zhou, W., Wang, Z. L., Eds.; Springer-Verlag New York: New York City, 2007.

(105) Henderson, R.; Glaeser, R. M. Quantitative Analysis of Image Contrast in Electron Micrographs of Beam-Sensitive Crystals. *Ultramicroscopy* **1985**, *16* (2), 139–150.

(106) Dubochet, J.; Lepault, J.; Freeman, R.; Berriman, J. A.; Homo, J.-C. Electron Microscopy of Frozen Water and Aqueous Solutions. *J. Microsc.* **1982**, *128* (3), 219–237.

(107) Taylor, K. A.; Glaeser, R. M. Electron Microscopy of Frozen Hydrated Biological Specimens. *J. Ultrastruct. Res.* **1976**, *55* (3), 448–456.

(108) Dubochet, J.; Chang, J.-J.; Freeman, R.; Lepault, J.; McDowall, A. W. Frozen Aqueous Suspensions. *Ultramicroscopy* **1982**, *10* (1), 55–61.

(109) Stark, H.; Zemlin, F.; Boettcher, C. Electron Radiation Damage to Protein Crystals of Bacteriorhodopsin at Different Temperatures. *Ultramicroscopy* **1996**, *63* (2), 75–79. h

(110) Li, X.; Mooney, P.; Zheng, S.; Booth, C. R.; Braunfeld, M. B.; Gubbens, S.; Agard, D. A.; Cheng, Y. Electron Counting and Beam-Induced Motion Correction Enable near-Atomic-Resolution Single-Particle Cryo-EM. *Nat. Methods* **2013**, *10*, 584.

(111) Frank, J.; Verschoor, A.; Boublik, M. Computer Averaging of Electron Micrographs of 40S Ribosomal Subunits. *Science (80-.).* **1981**, *214* (4527), 1353 LP – 1355.

Chapter 2

Synthesis and Functionalization of Ferrite Nanoparticles for Biological Applications

2.1 Introduction

Current magnetic nanoparticles studies exist for both the continual development of novel particles in conjunction with implementation of said particles as an aid to the advancement of other scientific research areas.[1–4] For example, magnetic nanoparticles see great use in biological and medicinal fields as purification tools, image contrast agents, or drug targeting and delivery methods.[5–9] Meanwhile, many groups still investigate the intrinsic properties of magnetic nanoparticles for their potential as ferrofluids,[10] energy and data storage materials,[11,12] or other magnetic devices.[13,14] Common among these varied applications is the challenge of stabilizing nanoparticles in solution such that they will not uncontrollably aggregate or self-assemble. One solution to this is to synthesize a superparamagnetic nanoparticle. Magnetic nanoparticles below a certain diameter can only host a single magnetic domain and become superparamagnetic.[1,2] They are disorganized outside of a magnetic field but will then cooperate and act as a "single" magnet with a greater response when introduced to a magnetic field.[2] Therefore, in order to avoid aggregation issues, it is desirable for magnetic nanoparticles to be superparamagnetic with small diameters below 20 nm and narrow size distributions.[11,15]

Of note are ferrite nanoparticles, which can be synthesized with improved magnetic properties – higher magnetic permeability, greater susceptibility, higher saturation magnetization, lower coercivity, and lower conductivity losses[7,15,16] than the baseline magnetite (Fe_3O_4) scaffold. Ferrites have been made with a range of metal cations including cobalt,[8,17] nickel,[18] manganese,[19] zinc,[13] or a mixture of two of these cations.[20] We aim to synthesize $Mn_xZn_{1-x}Fe_2O_4$, a ferrite known for its high saturation magnetization and high magnetic susceptibility.[7] Manganese was selected because the Mn^{2+} ion has the highest magnetic spin (5 μ_B) compared to other first-row transition metals.[21] Therefore, it is expected that manganese

ferrites will have higher magnetic susceptibilities than Fe_3O_4, $CoFe_2O_4$, and $NiFe_2O_4$.[7,21] In order to reduce the antiferromagnetic coupling between the tetrahedral A-sublattice and octahedral B-sublattice within the ferrite's spinel structure, small amounts of Zn^{2+} will also be added.[1,20] Diamagnetic Zn^{2+} favors the tetrahedral spaces within the A-sublattice, thereby decreasing the sublattice's magnetic moment and increasing the overall magnetic properties.[1,20] However, at higher zinc concentrations ($x < 0.6$), the ferrite changes from a mixed spinel to a normal spinel, changing the interactions of the sublattices, and resulting in an overall decrease of the magnetic moment.[1] With these conditions in mind, we have selected the following ratio of starting materials for our study: 2:0.7:0.5 Fe:Mn:Zn.

For these nanoparticles to be relevant to biological applications, they must be hydrophilic in nature and easily biofunctionalized. Most nanoparticle procedures result in a product coated in an oily surfactant; however, several post-synthetic modification methods exist in order to make ferrites water compatible.[6] For example, a ligand exchange can be applied to nanoparticles to exchange the oily surfactant with a hydrophilic coating.[22,23] Another method is to embed nanoparticles into amphiphilic polymer shells[22] or assemble them into micelles.[24] Alternatively, some magnetic nanoparticles were made water-soluble through a one-pot approach by replacing high-boiling-point solvents with water-soluble ones.[6,25] For this study, we take inspiration from Zhang et. al. and perform a similar ligand exchange on ferrite nanoparticles that replaces the oleic acid surfactant with hydrophilic polyelectrolyte molecules.[23]

As a final step, these ferrite nanoparticles were either wrapped in poly-lysine or incorporated into hydrogel nanoparticles to demonstrate their biofunctionalization capabilities. Poly-lysine coated surfaces can be modified for controlled protein adsorption,[26] DNA immobilization,[27,28] and stem cell labels.[29] On the other hand, hydrogel nanoparticles have been

incorporated in a variety of biological processes. Their flexible structure allows them to be tuned to specific cargo uptake and release,[30–32] or designed to detect chemical or biological targets.[33–35] Furthermore, existing examples combine hydrogel nanoparticles with inorganic nanoparticles for improved application, whether it is to aid in drug delivery through magnetic manipulation,[36,37] or provide advanced signal enhancement, thereby improving the sensitivity within a biosensor.[38–40] We believe successful combination of our ferrite nanoparticles with either poly-lysine or within a hydrogel will demonstrate the feasibility of these nanoparticles for future use in a variety of biological applications.

2.2 Methods and Materials

2.2.1 List of Materials

Iron (III) acetylacetonate (97%) (Fe-$(acac)_3$), manganese (II) acetylacetonate (Mn-$(acac)_2$), zinc (II) acetylacetonate (99.995%) (Zn-$(acac)_2$), and benzyl ether were purchased from Aldrich. Oleic acid, toluene, hexanes, and chloroform were purchased from Fisher Chemical. Argon (Ar) gas was acquired from Air Gas. Polyacrylic acid (63% solution in water) was received from Polysciences. Diethylene glycol, N-isopropylacrylamide (NIPAm), acrylic acid (AAc), sodium dodecyl sulfate (SDS), and ammonium persulfate (APS) was purchased from Sigma-Aldrich. 1-octcadecene (90% technical grade) and 0.5 M TRIS buffering solution (pH 8.5) was purchased from Alfa Aesar. Poly(L-lysine hydrobromide) (10 units) was purchased from Alamanda Polymers. N,N-methylenebis(acrylamide) (BIS) was obtained from Fluka. N-tert-butylacrylamide (TBAm) was obtained from Acros Organics. NIPAm was recrystallized from hexane before use. 11-mercaptoundecylamine (MUAM) was obtained from Dojindo. Ethyl alcohol (200 proof) was received from Gold Shield Distributors. Nanopure water was filtered

using a Milli-Q water purification system (Millipore) Concentrated sodium hydroxide was made by dissolving pellets from Macron Chemicals in nanopure water. 5.0 N hydrochloric acid was received from BDH. FTIR spectrum were taken on Fisher Scientific premium microscope slides that were vapor deposited with 1 nm chromium and 100 nm of gold from Kurt J. Lesker. SPRI microscopy substrates, borosilicate No. 1.5 coverslips, were purchased from Fisherbrand and coated by thermal vapor deposition of a 1 nm Cr adhesion layer and 45 nm Au. TEM grids (copper grids with formvar, stabilized with carbon, 400 mesh) were received from Ted Pella. All chemicals were used as received unless otherwise noted.

2.2.3 Synthesis of 10 nm $Mn_xZn_{1-x}Fe_2O_4$ Nanoparticles

Using a method inspired by a magnetite synthesis previously performed in this lab by Szyndler et. al., iron (III) acetylacetonate (0.478 g; 1.33 mmol), manganese (II) acetylacetonate (0.117 g; 0.465 mmol), and zinc (II) acetylacetonate (0.088 g; 0.334 mmol) were added to a round bottom flask.[41] To this was added oleic acid (2536 µL; 8.04 mmol) before dissolving everything in 1-octadecene (15 mL). Next, a stir bar was added, and the round bottom was hooked into a Schlenk line and vacuumed purged until the entire system was under Ar (g). The mixture was heated to 110 ºC and held for 30 minutes in order to remove oxygen dissolved in the solvents before continuing to heat the mixture to reflux at 290 ºC. The mixture was allowed to reflux for one half hour, during which it was observed to turn from reddish orange to black. After a half hour the mixture was allowed to cool and was washed with excess ethanol. Nanoparticles were collected through centrifugation (6000 rpm for 15 minutes) to first separate any undispersed residue, and then washed two more times in ethanol.

2.2.3 Synthesis of 40 nm $Mn_xZn_{1-x}Fe_2O_4$ Nanoparticles

40 nm ferrite nanoparticles were synthesized by first combining Fe-$(acac)_3$ (0.478 g; 1.33 mmol), Mn-$(acac)_2$ (0.117 g; 0.465 mmol), Zn-$(acac)_2$ (0.088 g; 0.334 mmol), and oleic acid (2536 µL; 8.04 mmol) in a round bottom flask. The contents of the round bottom flask were then dissolved in benzyl ether (15 mL). Next, a stir bar was added, and the round bottom was hooked into a Schlenk line and vacuumed purged until the entire system was under Ar (g). The mixture was heated to 290 ºC and allowed to reflux for one half hour. During this time the mixture was observed to turn from reddish orange to black. After a half hour the mixture was allowed to cool and was washed with 4:1 toluene:hexanes. Nanoparticles were collected through centrifugation (6000 rpm for 15 minutes) and washed three more times in chloroform.

2.2.4 Ligand Exchange of Ferrite Nanoparticles

Ferrite nanoparticles underwent a ligand exchange using a procedure inspired by Zhang et al. Polyacrylic acid solution (0.793 g) was measured out and added to a 3-neck round bottom flask. It was then dissolved in diethylene glycol (8 mL). A stir bar was added before hooking the flask into a Schlenk line. The flask was vacuum purged until its contents were under argon gas. The solution was heated and stirred to 110 °C before injecting about 1 mL of ferrite nanoparticle (32 mg) suspended in toluene. Then the solution heated to 240 ºC and allowed to reflux for 1 hour during which it was observed to turn brownish. The solution was then allowed to cool and was washed in excess dilute hydrochloric acid (0.1 M). The nanoparticles were collected through centrifugation (6000 rpm for 15 minutes) and wash with nanopure water three times. The nanoparticles were then ionized by suspending them in dilute NaOH (0.1 M).[23]

2.2.5 poly-Lysine Coating of Ferrite Nanoparticles

The polyacrylic acid capped nanoparticles were electrostatically wrapped in a poly-Lysine coating. First, the hydrophilic ferrite nanoparticles were transferred from dilute NaOH solution into Tris buffer (pH 8.5) using magnetic separation. A neodymium magnet was used to secure the magnetic nanoparticles in place while the NaOH was removed and replaced with Tris buffer. Next, an excess of short 10-unit chains of poly-lysine (pLys) was measured out (2 mg/mL) and added to solution. The nanoparticles were allowed to mix with the pLys for 4 hours, sonicating periodically. As a final step, excess pLys was washed away using magnetic separation similar to what was described above.

2.2.6 Incorporation of Ferrite Nanoparticles into Hydrogels

Hydrogel nanoparticle synthesis was adapted from the procedure detailed in Matthews. The monomers NIPAm (53 mol %), TBAm (38 mol %), AAc (5 mol %), and BIS (2 mol %) were dissolved in 1.7 mL of nanopure water in a round-bottom flask for a total monomer concentration of 21 mM. TBAm was dissolved in 50 μL of ethanol before addition to the monomer solution and the surfactant SDS (0.25 mg) was also added to the monomer solution. Nitrogen gas was bubbled through the solution for 30 minutes. Following the addition of a 100 μL aqueous solution containing 1 mg of APS, the polymerization reaction was carried out in an oil bath preset to 60 °C. For ferrite-encapsulation HNP synthesis, 100 μL of the diluted polyacrylic acid wrapped ferrite nanoparticle solution was added to the aqueous solution after thirty minutes of reaction time. From there, the reaction was permitted to continue for an additional 2.5 hours under nitrogen atmosphere. The resulting solution was purified by dialysis using a 12-14 kDa molecular weight cut off dialysis membrane against an excess amount of nanopure water (changed three times a day) for 3 days.[42]

2.2.6 Characterization of Nanoparticles

The high-angle annular dark field (HAADF) and bright field (BF) images of ferrite samples were acquired using JEOL Grand ARM TEM/STEM operated at 300 kV STEM mode. Simultaneously, the elemental mapping via energy dispersive X-ray spectroscopy (EDS) was collected by the large angle dual dry solid-state 100 mm^2 detectors. Diffraction patterns were obtained on a JEOL-2100F Cryo-TEM using a JEOL double tilt holder and recorded on a OneView camera (Gatan, Inc.). For X-ray diffraction measurements, ferrite samples were baked for 5 hours at 500 ºC to remove their oleic acid coating. The collected powder was analyzed on a Rigaku Smartlab X-ray Diffractometer with Cu kα radiation and analyzed using PDXL: Integrated X-ray Powder Diffraction software.

FTIR measurements were acquired using a Jasco FT/IR-4100 with a Harrick Refractor 2 reflectance attachment and a liquid nitrogen cooled MCT detector (Jasco). Zeta potential measurements were taken on a Malvern Zetasizer ZS Nano DLS (Malvern) using Zetasizer Nano Series disposable folded capillary cells (Malvern).

Hydrogel nanoparticle images were obtained on a Cryo-TEM image using 3μL of concentrated sample solution applied on a glow-discharged Quantifoil grid (Quantifoild, R2/2) and then loaded on Leica EMGP plunger (Leica Biosystem). The grid was quickly plunged into liquid propane after blotting away the excess liquid and the hydrogel particles were then embedded in a thin layer of vitrified ice on the grid. The cryo-grid was then transferred into a JEM-2100F electron microscope using a Gatan cryo-transfer holder (Gatan, Inc). The electron microscope was operated at 200KV with a field emission gun and specimen was examined under minimum dose system. The images were recorded on a OneView camera (Gatan, Inc.) at 40,000X magnification, corresponding to 0.28 nm per pixel at specimen space.

2.3 Results and Discussion

2.3.1 Synthesis of Ferrite Nanoparticles

$Mn_xZn_{1-x}Fe_2O_4$ nanoparticles were successfully synthesized through the reaction of Fe-$(acac)_3$, Mn-$(acac)_2$, and Zn-$(acac)_2$ with a surfactant at high temperatures. The mechanism behind thermal decomposition methods is reported as follows: precursor materials (Fe-$(acac)_3$, Mn-$(acac)_2$, and Zn-$(acac)_2$) dissolve, upon heating they decompose and form monomeric building units, which accumulate and nucleate into nanoparticles.[43,44] If the precursors were heated in the solvent 1-octadecene, highly mono-disperse nanoparticles averaging 10 nm in diameter were produced. These nanoparticles were magnetized in the presence of a neodymium magnet and were observed to return to an unaggregated powder when the magnet was removed, suggesting they have superparamagnetic characteristics. If the solvent is switched to benzyl ether, the resulting polydisperse nanoparticles were observed to be 40 nm in diameter. Though both solvents are thought of as "non-coordinating" solvents, benzyl ether shows a slightly stronger affinity for the nanoparticle's monomeric building units. Qiao et. al. reasoned that solvents with higher polarity, will result in an increase of average magnetite nanoparticle size.[44] Therefore we can expect to observe larger nanoparticles when using benzyl ether compared to the less polar alkenes from 1-octadecene. The 40 nm nanoparticles were also magnetized in the presence of a neodymium magnet; however, they would remain aggregated in the absence of the magnet, suggesting they are not completely superparamagnetic.

2.3.2 TEM Analysis of Ferrite Nanoparticles

2.3.2.1 Analysis of 10 nm Nanoparticles

TEM analysis of the smaller ferrite nanoparticles confirmed these nanoparticles average 10 ± 1 nm in diameter and are highly monodisperse (Figure 2.1 a). A higher magnification TEM image in Figure 2.1 c shows the distance between two adjacent planes to be 2.11 Å, which corresponds to (400) lattice planes in spinel-structured ferrites and a unit cell of 8.44 Å. An electron diffraction pattern of these nanoparticles (Figure 2.1 d) shows that the nanoparticles are single crystal in structure. Table 2.1 displays the measured lattice spacings based on the points in the diffraction pattern, or in one case based on an FFT performed on a TEM micrograph of ferrite nanoparticles (Figure A.1), and compares them to known lattice spacings for magnetite (Fe_3O_4) along with their *hkl* indexes from literature values.[15] The values are well matched and the lack of any secondary diffraction patterns lead us to believe our nanoparticles are single crystal with a spinel structure similar to Fe_3O_4. The undispersed residue from the synthesis was observed using TEM to be aggregations of 10 nm nanoparticles.

Table 2.1. Measured lattice spacings, *d* (Å), based on diffraction points in Figure 2.1 d compared to the d-spacings calculated from the XRD peak measurements and the standard lattice spacing for Fe_3O_4 and the respective *hkl* indexes.

	Diffraction Points								
	1	2	3	4	5	6	7	8	9
d	-	2.99*	2.49	2.05	-	1.57	1.45	-	1.23
XRD	-	2.96	2.53	2.09	1.71	1.61	1.48	-	1.27
Fe_3O_4	4.86	2.97	2.53	2.1	1.71	1.62	1.48	1.33	1.28
hkl	111	220	311	400	422	511	440	620	533

*value obtained from the resulting FFT performed on a TEM micrograph of ferrite nanoparticles (Figure A.1).

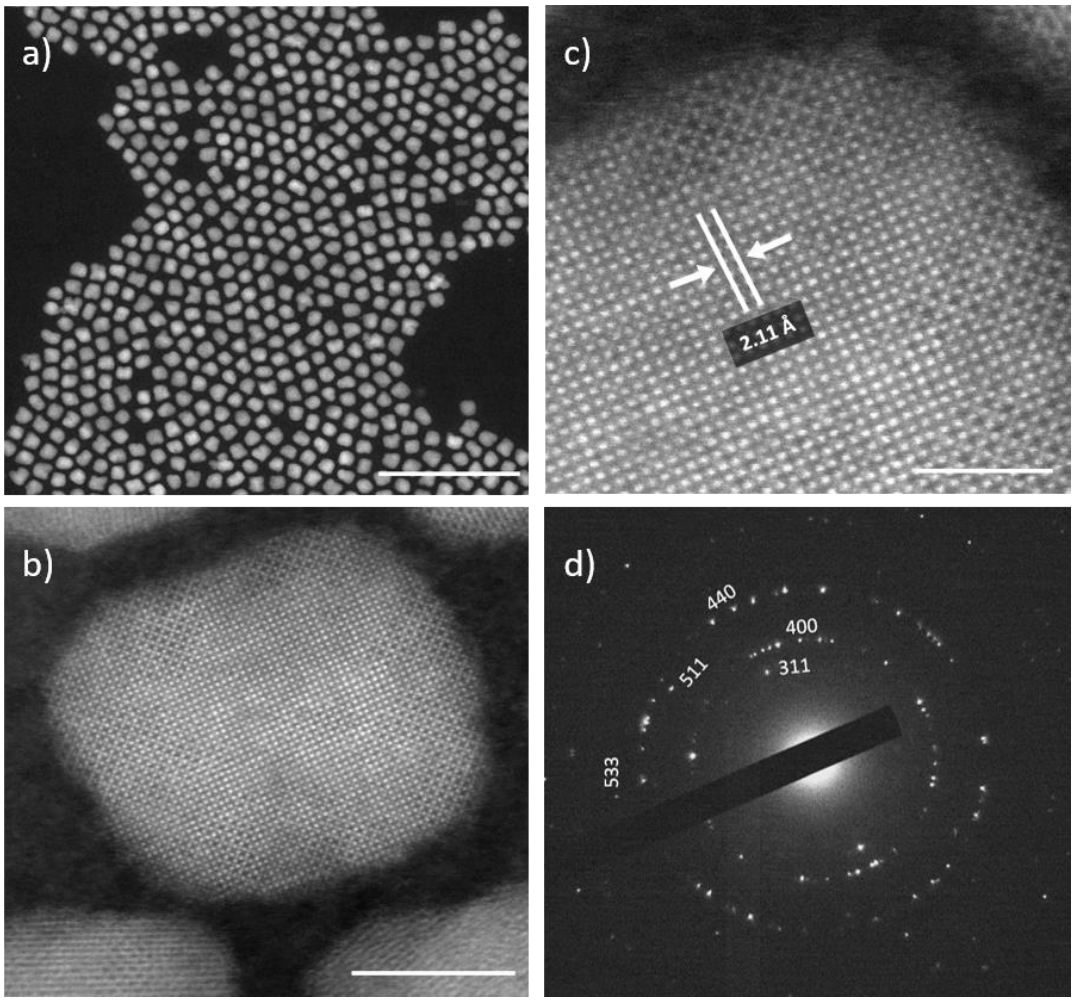

Figure 2.1. TEM images of ferrite nanoparticles taken on a Grand Arm JEOL Grand ARM TEM with scale bars representing a) 100 nm and b) 5 nm. c) A zoomed in TEM micrograph of a ferrite nanoparticle showing the 400 plane. Scale bar represents 2 nm. d) Diffraction pattern of ferrite nanoparticles taken on JEOL 2100F Cryo-TEM. Diffraction points have been labelled with their corresponding *hkl* indexes.

2.3.2.2 Analysis of 40 nm Nanoparticles

TEM was also used to confirm the size and shape of larger ferrite nanoparticles. Nanoparticles averaged around 40 nm in size but were not observed from TEM images to be as monodisperse in size as the 10 nm ferrites. However, they are uniform in their octahedral shape. The development of these larger nanoparticles into distinct octahedral shapes is again likely

linked to the solvent used during synthesis.[44] Higher polarity benzyl ether has a stronger affinity for monomers and therefore increases monomer activity.[44] This in turn, affects the growth rate of the three low-index planes, which in order of highest chemical potential to lowest are: {100}, {110}, and {111}.[45] Because the chemical potential of the monomeric building blocks in solution are higher than all three of the index planes, the monomers can deposit along any plane at a rate determined by the activation barrier for deposition.[44,45] Stable {111} facets have the largest activation barrier and therefore grow the slowest, producing octahedra, or sometimes tetrahedra.[44] Monomers with reduced activity, such as those in a solvent such as 1-octadecene, may have chemical potentials lower than the {100} plane. Therefore, they will only grow along the {110} and {111} facets, resulting in a more cube-like structure.[44] A higher magnification micrograph of a ferrite nanoparticle (Figure 2.3 b) shows a spacing of 4.79 Å between what appears to be the (111) lattice plane based on the arrangement of the atoms.

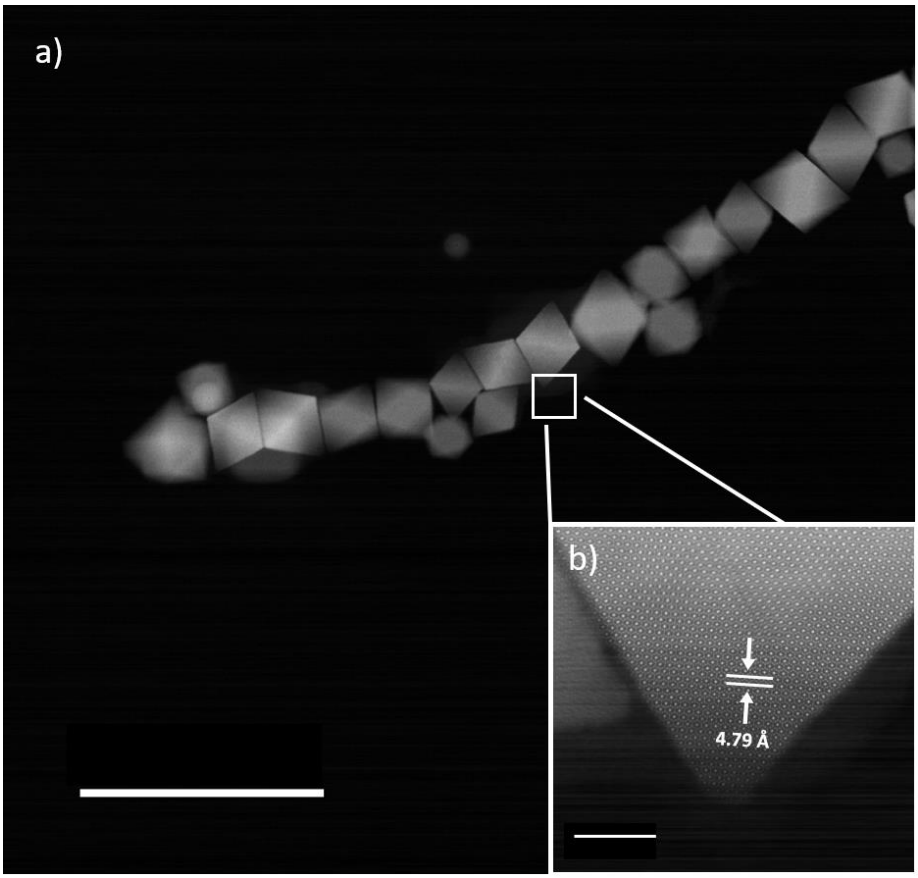

Figure 2.2. TEM images of 40 nm ferrite nanoparticles and their crystal lattice. Inset shows ferrite crystal lattice in the 111 plane. Scale bar represents (a) 200 nm and (b) 5 nm.

2.3.3 Surface Characterization of Ferrite Nanoparticles

Elemental mapping was also performed on the ferrite nanoparticles using the EDS function on the JEOL Grand ARM TEM/STEM. Results from the EDS spectrum (Figures 2.3 and 2.4) confirm the presence of all three metal cations, however the reported ratios of Fe/Mn and Fe/Zn are significantly higher than the precursor ratios for both sizes of nanoparticles (Table A.1), indicating the syntheses of these nanoparticles are non-stoichiometric.

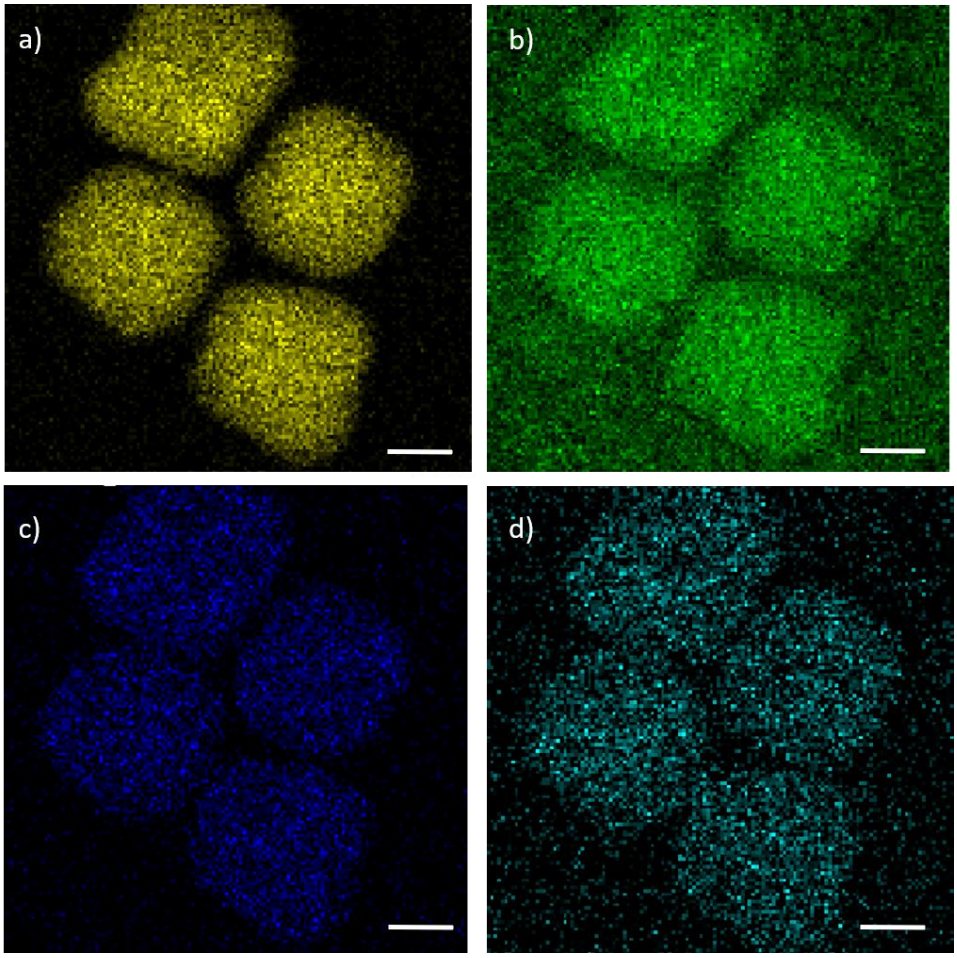

Figure 2.3. Elemental maps for 10 nm ferrite nanoparticles obtained by EDS-TEM showing a) iron (yellow), b) oxygen (green), c) manganese (blue), and d) zinc (teal). Scale bar represents 5 nm.

The EDS spectrum for 40 nm ferrites (Figure 2.4) also shows and interesting preference for Mn^{2+} and Zn^{2+} ions to leech to the surface. To explain this phenomenon, we return to Qiao et. al. As explored previously, the activity of monomeric building blocks has significant impact on the resulting size and shape. Monomer activity is dependent on its activity coefficient and molar concentration.[44] As there is a significantly higher concentration of iron cations compared to manganese or zinc, monomers with Mn^{2+} and Zn^{2+} will have a lower activity. It could be that

this lower activity limits these monomers to only grow in the {111} plane, possibly explaining this apparent preference for the nanoparticle surface, which is mostly the {111} facet.

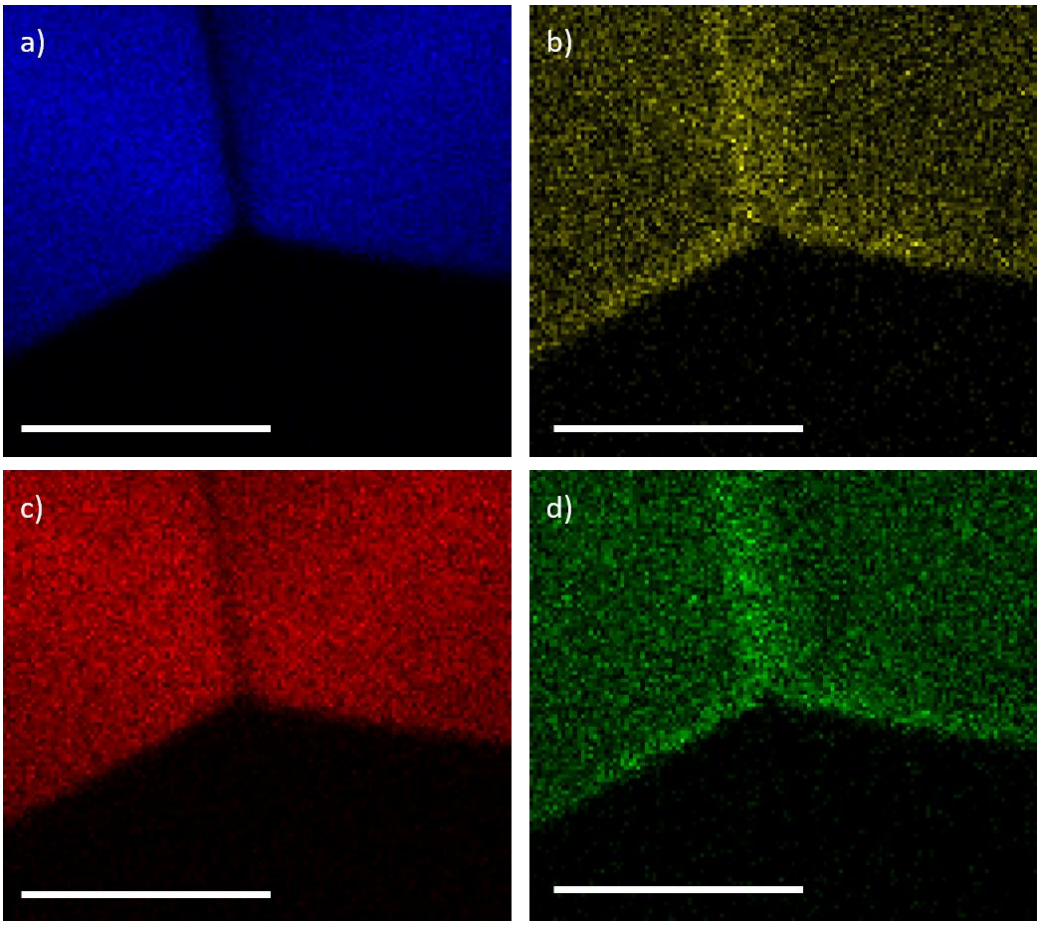

Figure 2.4. Element maps for 40 nm ferrite nanoparticles obtained by TEM-EDS of (a) iron (blue), (b) zinc (yellow), (c) oxygen (red), and (d) manganese (green). Scale bar represents 20 nm.

2.3.4 XRD Characterization of Ferrite Nanoparticles

Structural information from a powdered sample of ferrite nanoparticles was obtained using a Rigaku Smartlab X-ray Diffractometer. Figure 2.5 shows the XRD patterns for the 10 nm ferrite nanoparticles (blue) and the 40 nm ferrite nanoparticles (red). Despite the lower intensities of the 10 nm ferrite pattern, the peak positions and relative intensities between the two

patterns match well, suggesting the phase and lattice parameters are preserved between the varying sizes. Additionally, the peak patterns match well with standard diffraction data for $Mn_xZn_{1-x}Fe_2O_4$ powders. Both sets of diffraction peaks were indexed as cubic phase [space group of F$d\bar{3}$m]. The d-spacings were calculated from both peak patterns and observed to match well with the diffraction pattern calculations and the known lattice spacings for magnetite (Table 2.1). The calculated lattice parameters for both smaller and larger nanoparticles also matched closely with the real spacings observed from the TEM images (Figure 2.1 c and 2.2 b). Smaller nanoparticles reported a lattice parameter of a = 8.38 Å and larger nanoparticles reported a value of a = 8.41 Å.

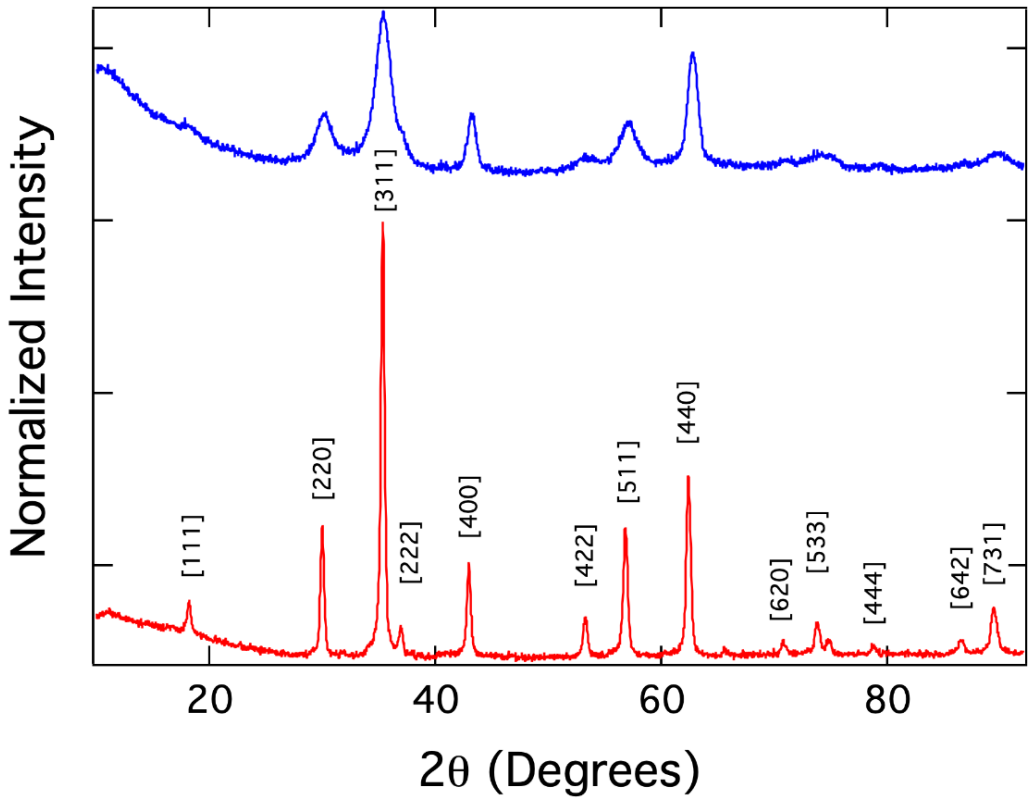

Figure 2.5. XRD powder diffraction of 40 nm ferrite nanoparticles (red) and 10 nm ferrite nanoparticles (blue). *hkl* values labelled match previously reported peaks for ferrite nanoparticles.

2.3.5 Ferrite Nanoparticle Ligand Exchange

Hydrophobic oleic acid surfactant was exchanged for polyacrylic acid in order to make hydrophilic polyacrylic acid coated ferrite nanoparticles (PAA-ferrite). Polyacrylic acid was selected for its strong affinity to metal oxide surfaces and high density of polar groups.[23] The ligand exchange was performed in diethylene glycol, which has a high miscibility with both aqueous and organic solvents, and a high boiling point in order to ensure a high exchange ratio.[23] The resulting product was observed to suspend well in water, confirming the success of the ligand exchange. In the case of the 10 nm ferrites, the reaction was observed to work best using the undispersed nanoparticle aggregates. We believe the undispersed aggregates are more easily transferred from toluene into diethylene glycol, making them more accessible to the ligand exchange. The well suspended ferrites do not transfer easily from toluene into diethylene glycol, resulting in smaller yields.

TEM images were taken after performing a ligand exchange to observe if any changes occurred during the reaction. No noticeable changes were observed in the shape and size of 10 nm ferrite nanoparticles post ligand exchange. We noted that the 40 nm nanoparticles lost their octahedral shape, showing more rounded edges. This change might signify the formation of the PAA-coating but is more likely the result from sintering effect while being heated in the reaction flask.[14,46] Additionally, the average size of the larger nanoparticles is now smaller, around 20 nm. We attribute this observation to the transfer step during the ligand exchange, which is selective for smaller nanoparticles. Nanoparticles are introduced into the reaction chamber by first suspending them in toluene and then injecting them into the reaction. Because smaller nanoparticles are easier to suspend, only these nanoparticles are transferred into the ligand exchange reaction chamber, resulting in a population of < 20 nm nanoparticles.

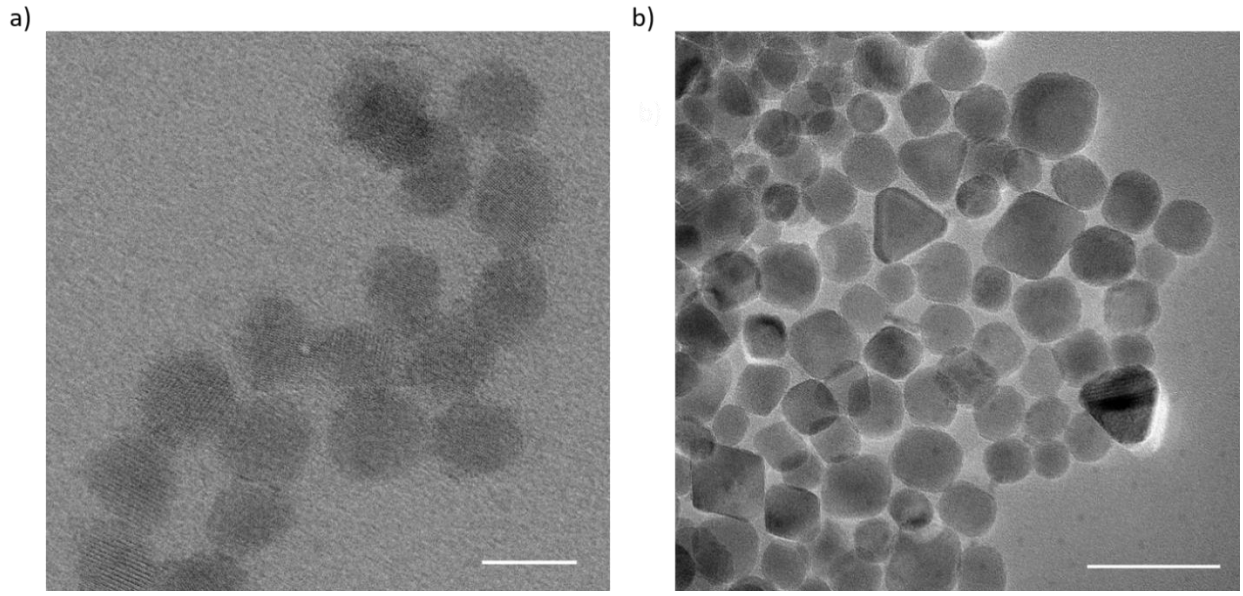

Figure 2.6. TEM images of ferrite nanoparticles with oleic acid exchanged for polyacrylic acid. Ligand exchange was performed on both a) 10 nm ferrite nanoparticles and b) 40 nm ferrite nanoparticles. Scale bar represents 10 nm and 50 nm respectively.

2.3.6 poly-Lysine wrapping of Ferrite Nanoparticles

In order to confirm the successful manipulation of the surface chemistry between the PAA-ferrites and the poly-lysine wrapped PAA-ferrites (pLys-PAA-ferrite), FTIR and zeta potential measurements were taken. FTIR measurements were collected in reflectance mode to observe changes in the peaks between different solutions of nanoparticles. As expected, PAA-ferrite shows carboxylic acid stretches at 1332 cm^{-1}, 1413 cm^{-1}, and 1499 cm^{-1}, which are likely the C−O stretch, $-COO^-$ symmetric stretch, and $-COO^-$ antisymmetric stretch respectively, .[47,48] The broad peak at 1737 cm^{-1} is likely the C=O stretch. After the poly-lysine wrapping, these peaks disappeared, and the amide stretches at 1630 cm^{-1}, and 1555 cm^{-1} were observed, leading us to believe the magnetic nanoparticles were successfully wrapped in poly-lysine.[49] Zeta potential measurements were taken to track the growth of the charged polymer wrappings. Both samples were measured at pH 8.5, and a change in zeta potential was observed from -43 mV ± 5

mV (PAA) to +50 mV ± 10 mV (pLys), indicating a change from the negatively charged $-COO^-$ from polyacrylic acid to the $-NH_3^+$ off the poly-lysine wrapping.

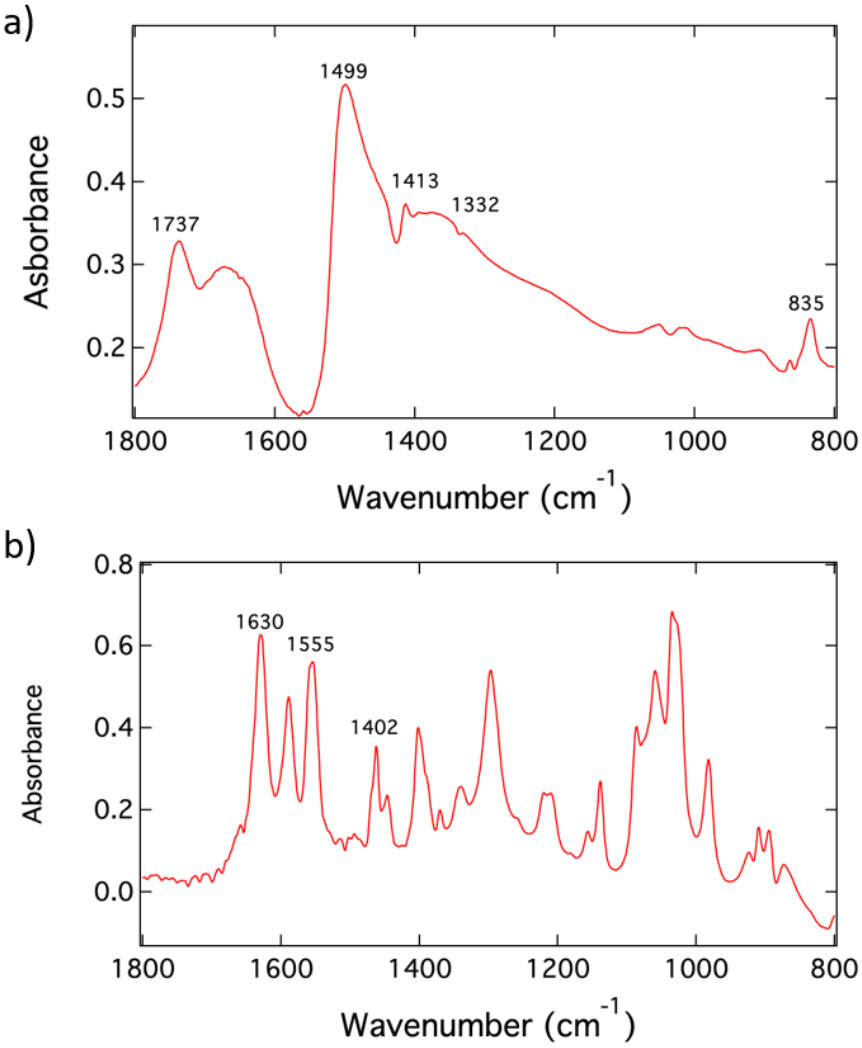

Figure 2.7. FTIR spectrum of 10 nm ferrites with a) polyacrylic acid as the capping ligand and b) electrostatically wrapped with poly-lysine.

Table 2.2. Comparison of FTIR peak assignments for polyacrylic wrapped PAA-ferrites (PAA-ferrite)[47,48] and poly-lysine coated ferrites (pLys-PAA-ferrites).[49]

PAA-Ferrite		pLys-PAA-Ferrite	
Peak position (cm^{-1})	**Peak assignment**	**Peak position (cm^{-1})**	**Peak assignment**
1737	–C=O	1630	Amide I (C=O)
1671	Water	1589	
1499	$–COO^-$ antisymmetric stretch	1555	Amide II (N–H bend)
1438	CH_2 scissor	1462	
1413	$–COO^-$ symmetric stretch	1402	$–COO^-$
1332	C–O stretch	1296	
835	Fe–OH–Fe	1059	
		1034	

2.3.6 Synthesis and Characterization of Ferrite Incorporated Hydrogels

To further test the biological functionality of these nanoparticles, larger PAA-ferrite nanoparticles were incorporated into hydrogel nanoparticles. Hydrogels were synthesized using polyacrylic acid as the polymer backbone and ferrites were added during the synthesis to be incorporated into this backbone. Ferrite encapsulation was investigated using cryo-EM. As the hydrogels are mostly full of water, preserving the hydrogels in vitreous ice and imaging using cryo-EM was expected to give the most accurate results. As seen in Figure 2.8, the presence of ferrite nanoparticles can clearly be seen within ferrite incorporated hydrogels as compared to hydrogels synthesized without ferrite. We believe the excess of ferrite observed is due to the sample preparation process, which concentrates the hydrogels using a magnet and attracts free ferrite nanoparticles as well. Further analysis of these ferrite incorporated hydrogels via SPR microscopy have led us to believe ferrite was successfully incorporated into the hydrogel nanoparticle as detailed in Chapter 4 of Brandon Matthews' thesis.[50]

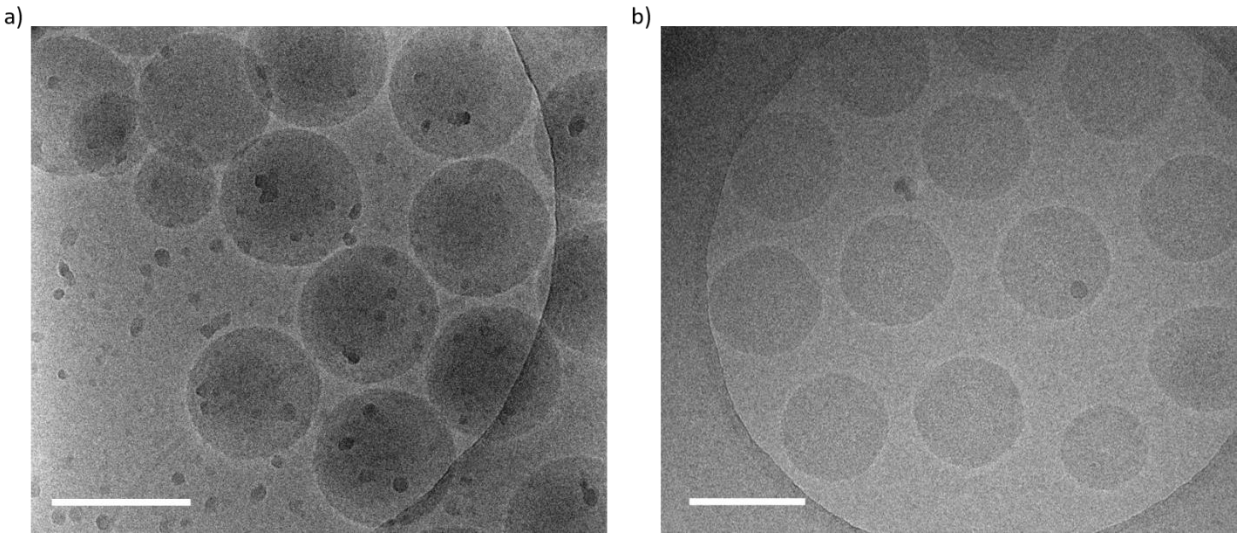

Figure 2.8. Cryo-EM micrographs of a) ferrite incorporated hydrogel nanoparticles and b) hydrogel nanoparticles without ferrite incorporation. Scale bars represent 200 nm.

2.4 Conclusion

In conclusion, we demonstrate a new procedure for hydrophilic ferrite nanoparticles of various sizes. Thermal decomposition of metal precursors in either 1-octadecene or benzyl ether produced ferrite nanoparticles averaging 10 nm and 40 nm in diameter respectively. These nanoparticles were analyzed using a combination of microscope and surface techniques to confirm their size, shape, and composition. At smaller sizes, the nanoparticles are monodisperse and initial observations in their magnetic properties suggest they are superparamagnetic and magnetic measurements should be obtained to determine their effectiveness within biomedical applications.[15] Larger nanoparticles are not as monodisperse in size nor are they superparamagnetic, but they have a distinct crystal structure that can easily be characterized by XRD. Both sizes of nanoparticles were successfully suspended in an aqueous solution via a ligand exchange adapted from Zhang et al. and subsequently wrapped in poly-Lysine. The changing surface chemistry was tracked using FTIR and by observing the change in zeta-

potential from negative to positive. Finally, larger PAA-ferrites were successfully incorporated in hydrogel nanoparticles, suggesting potential applications in hydrogel-based drug delivery or biosensing.

2.5 Acknowledgements

This work was supported by the National Science Foundation through grant CHE-1807317 and through grant CHE-1403506. Zeta-potentials were performed at the UC Irvine Laser Spectroscopy Labs. TEM, cryo-EM, and XRD analyses were performed at the UC Irvine Materials Research Institute (IMRI). The author would like to thank Dr. Mingjie Xu and Dr. Li Xing for their help with TEM and cryo-EM measurements.

2.6 References

(1) Mathew, D. S.; Juang, R.-S. An Overview of the Structure and Magnetism of Spinel Ferrite Nanoparticles and Their Synthesis in Microemulsions. *Chem. Eng. J.* **2007**, *129* (1), 51–65.

(2) Kodama, R. H. Magnetic Nanoparticles. *J. Magn. Magn. Mater.* **1999**, *200* (1), 359–372.

(3) Kemp, S. J.; Ferguson, R. M.; Khandhar, A. P.; Krishnan, K. M. Monodisperse Magnetite Nanoparticles with Nearly Ideal Saturation Magnetization. *RSC Adv.* **2016**, *6* (81), 77452–77464.

(4) Rath, C.; Anand, S.; Das, R. P.; Sahu, K. K.; Kulkarni, S. D.; Date, S. K.; Mishra, N. C. Dependence on Cation Distribution of Particle Size, Lattice Parameter, and Magnetic Properties in Nanosize Mn–Zn Ferrite. *J. Appl. Phys.* **2002**, *91* (4), 2211–2215.

(5) Mornet, S.; Vasseur, S.; Grasset, F.; Duguet, E. Magnetic Nanoparticle Design for Medical Diagnosis and Therapy. *J. Mater. Chem.* **2004**, *14* (14), 2161–2175.

(6) Yang, H.; Zhang, C.; Shi, X.; Hu, H.; Du, X.; Fang, Y.; Ma, Y.; Wu, H.; Yang, S. Water-Soluble Superparamagnetic Manganese Ferrite Nanoparticles for Magnetic Resonance Imaging. *Biomaterials* **2010**, *31* (13), 3667–3673.

(7) Karimi, Z.; Karimi, L.; Shokrollahi, H. Nano-Magnetic Particles Used in Biomedicine: Core and Coating Materials. *Mater. Sci. Eng. C* **2013**, *33* (5), 2465–2475.

(8) Bai, J.; Wang, J.-P. High-Magnetic-Moment Core-Shell-Type FeCo–Au⁄Ag Nanoparticles. *Appl. Phys. Lett.* **2005**, *87* (15), 152502.

(9) Berry, C. C.; Curtis, A. S. G. Functionalisation of Magnetic Nanoparticles for Applications in Biomedicine. *J. Phys. D. Appl. Phys.* **2003**, *36* (13), R198–R206.

(10) Raj, K.; Moskowitz, B.; Casciari, R. Advances in Ferrofluid Technology. *J. Magn. Magn. Mater.* **1995**, *149* (1), 174–180.

(11) Dai, Q.; Berman, D.; Virwani, K.; Frommer, J.; Jubert, P.-O.; Lam, M.; Topuria, T.; Imaino, W.; Nelson, A. Self-Assembled Ferrimagnet−Polymer Composites for Magnetic Recording Media. *Nano Lett.* **2010**, *10* (8), 3216–3221.

(12) Sun, S.; Anders, S.; Hamann, H. F.; Thiele, J.-U.; Baglin, J. E. E.; Thomson, T.; Fullerton, E. E.; Murray, C. B.; Terris, B. D. Polymer Mediated Self-Assembly of Magnetic Nanoparticles. *J. Am. Chem. Soc.* **2002**, *124* (12), 2884–2885.

(13) Yan, A.; Liu, X.; Yi, R.; Shi, R.; Zhang, N.; Qiu, G. Selective Synthesis and Properties of Monodisperse Zn Ferrite Hollow Nanospheres and Nanosheets. *J. Phys. Chem. C* **2008**, *112* (23), 8558–8563.

(14) Dias, A.; Buono, V. T. L. Hydrothermal Synthesis and Sintering of Nickel and Manganese-Zinc Ferrites. *J. Mater. Res.* **1997**, *12* (12), 3278–3285.

(15) Sun, S.; Zeng, H.; Robinson, D. B.; Raoux, S.; Rice, P. M.; Wang, S. X.; Li, G. Monodisperse MFe2O4 (M = Fe, Co, Mn) Nanoparticles. *J. Am. Chem. Soc.* **2004**, *126* (1), 273–279.

(16) Calvin, S.; Carpenter, E. E.; Ravel, B.; Harris, V. G.; Morrison, S. A. Multiedge Refinement of Extended X-Ray-Absorption Fine Structure of Manganese Zinc Ferrite Nanoparticles. *Phys. Rev. B* **2002**, *66* (22), 224405.

(17) Skumryev, V.; Stoyanov, S.; Zhang, Y.; Hadjipanayis, G.; Givord, D.; Nogués, J. Beating the Superparamagnetic Limit with Exchange Bias. *Nature* **2003**, *423* (6942), 850–853.

(18) Misra, R. D. K.; Gubbala, S.; Kale, A.; Egelhoff, W. F. A Comparison of the Magnetic Characteristics of Nanocrystalline Nickel, Zinc, and Manganese Ferrites Synthesized by Reverse Micelle Technique. *Mater. Sci. Eng. B* **2004**, *111* (2), 164–174.

(19) Warner, C. L.; Chouyyok, W.; Mackie, K. E.; Neiner, D.; Saraf, L. V; Droubay, T. C.; Warner, M. G.; Addleman, R. S. Manganese Doping of Magnetic Iron Oxide Nanoparticles: Tailoring Surface Reactivity for a Regenerable Heavy Metal Sorbent. *Langmuir* **2012**, *28* (8), 3931–3937.

(20) Makovec, D.; Kodre, A.; Arčon, I.; Drofenik, M. Structure of Manganese Zinc Ferrite Spinel Nanoparticles Prepared with Co-Precipitation in Reversed Microemulsions. *J. Nanoparticle Res.* **2009**, *11* (5), 1145–1158.

(21) Lee, J.-H.; Huh, Y.-M.; Jun, Y.; Seo, J.; Jang, J.; Song, H.-T.; Kim, S.; Cho, E.-J.; Yoon, H.-G.; Suh, J.-S.; et al. Artificially Engineered Magnetic Nanoparticles for Ultra-Sensitive Molecular Imaging. *Nat. Med.* **2007**, *13* (1), 95–99.

(22) Tromsdorf, U. I.; Bigall, N. C.; Kaul, M. G.; Bruns, O. T.; Nikolic, M. S.; Mollwitz, B.; Sperling, R. A.; Reimer, R.; Hohenberg, H.; Parak, W. J.; et al. Size and Surface Effects on the MRI Relaxivity of Manganese Ferrite Nanoparticle Contrast Agents. *Nano Lett.* **2007**, *7* (8), 2422–2427.

(23) Zhang, T.; Ge, J.; Hu, Y.; Yin, Y. A General Approach for Transferring Hydrophobic Nanocrystals into Water. *Nano Lett.* **2007**, *7* (10), 3203–3207.

(24) Lu, J.; Ma, S.; Sun, J.; Xia, C.; Liu, C.; Wang, Z.; Zhao, X.; Gao, F.; Gong, Q.; Song, B.; et al. Manganese Ferrite Nanoparticle Micellar Nanocomposites as MRI Contrast Agent for Liver Imaging. *Biomaterials* **2009**, *30* (15), 2919–2928.

(25) Cheng, F.-Y.; Su, C.-H.; Yang, Y.-S.; Yeh, C.-S.; Tsai, C.-Y.; Wu, C.-L.; Wu, M.-T.; Shieh, D.-B. Characterization of Aqueous Dispersions of Fe3O4 Nanoparticles and Their Biomedical Applications. *Biomaterials* **2005**, *26* (7), 729–738.

(26) Frey, B. L.; Jordan, C. E.; Kornguth, S.; Corn, R. M. Control of the Specific Adsorption of Proteins onto Gold Surfaces with Poly(L-Lysine) Monolayers. *Anal. Chem.* **1995**, *67* (24), 4452–4457.

(27) Stobiecka, M.; Hepel, M. Double-Shell Gold Nanoparticle-Based DNA-Carriers with Poly-l-Lysine Binding Surface. *Biomaterials* **2011**, *32* (12), 3312–3321.

(28) Ivanova, E. P.; Pham, D. K.; Brack, N.; Pigram, P.; Nicolau, D. . Poly(l-Lysine)-Mediated Immobilisation of Oligonucleotides on Carboxy-Rich Polymer Surfaces. *Biosens. Bioelectron.* **2004**, *19* (11), 1363–1370.

(29) Babič, M.; Horák, D.; Trchová, M.; Jendelová, P.; Glogarová, K.; Lesný, P.; Herynek, V.; Hájek, M.; Syková, E. Poly(l-Lysine)-Modified Iron Oxide Nanoparticles for Stem Cell Labeling. *Bioconjug. Chem.* **2008**, *19* (3), 740–750.

(30) Moura, L. M.; Martinho, J. M. G.; Farinha, J. P. S. DNA Hybridization in Thermoresponsive Polymer Nanoparticles. *ChemPhysChem* **2010**, *11* (8), 1749–1756.

(31) Wang, D.; Hu, Y.; Liu, P.; Luo, D. Bioresponsive DNA Hydrogels: Beyond the Conventional Stimuli Responsiveness. *Acc. Chem. Res.* **2017**, *50* (4), 733–739.

(32) Lilienthal, S.; Shpilt, Z.; Wang, F.; Orbach, R.; Willner, I. Programmed DNAzyme-Triggered Dissolution of DNA-Based Hydrogels: Means for Controlled Release of Biocatalysts and for the Activation of Enzyme Cascades. *ACS Appl. Mater. Interfaces* **2015**, *7* (16), 8923–8931.

(33) Dave, N.; Chan, M. Y.; Huang, P.-J. J.; Smith, B. D.; Liu, J. Regenerable DNA-Functionalized Hydrogels for Ultrasensitive, Instrument-Free Mercury(II) Detection and Removal in Water. *J. Am. Chem. Soc.* **2010**, *132* (36), 12668–12673.

(34) Maley, A. M.; Terada, Y.; Onogi, S.; Shea, K. J.; Miura, Y.; Corn, R. M. Measuring Protein Binding to Individual Hydrogel Nanoparticles with Single-Nanoparticle Surface Plasmon Resonance Imaging Microscopy. *J. Phys. Chem. C* **2016**, *120* (30), 16843–16849.

(35) Carvalho, W. S. P.; Wei, M.; Ikpo, N.; Gao, Y.; Serpe, M. J. Polymer-Based Technologies for Sensing Applications. *Anal. Chem.* **2018**, *90* (1), 459–479.

(36) Riedinger, A.; Pernia Leal, M.; Deka, S. R.; George, C.; Franchini, I. R.; Falqui, A.; Cingolani, R.; Pellegrino, T. "Nanohybrids" Based on PH-Responsive Hydrogels and Inorganic Nanoparticles for Drug Delivery and Sensor Applications. *Nano Lett.* **2011**, *11* (8), 3136–3141.

(37) Giani, G.; Fedi, S.; Barbucci, R. Hybrid Magnetic Hydrogel: A Potential System for Controlled Drug Delivery by Means of Alternating Magnetic Fields. *Polymers (Basel).* **2012**, *4* (2), 1157–1169.

(38) Contreras-Cáceres, R.; Sánchez-Iglesias, A.; Karg, M.; Pastoriza-Santos, I.; Pérez-Juste, J.; Pacifico, J.; Hellweg, T.; Fernández-Barbero, A.; Liz-Marzán, L. M. Encapsulation and Growth of Gold Nanoparticles in Thermoresponsive Microgels. *Adv. Mater.* **2008**, *20* (9), 1666–1670.

(39) Zhan, P.; Dutta, P. K.; Wang, P.; Song, G.; Dai, M.; Zhao, S.-X.; Wang, Z.-G.; Yin, P.; Zhang, W.; Ding, B.; et al. Reconfigurable Three-Dimensional Gold Nanorod Plasmonic Nanostructures Organized on DNA Origami Tripod. *ACS Nano* **2017**, *11* (2), 1172–1179.

(40) Kim, J.-H.; Boote, B. W.; Pham, J. A.; Hu, J.; Byun, H. Thermally Tunable Catalytic and Optical Properties of Gold–Hydrogel Nanocomposites. *Nanotechnology* **2012**, *23* (27), 275606.

(41) Szyndler, M. W.; Corn, R. M. Self-Assembly of Flux-Closure Polygons from Magnetite Nanocubes. *J. Phys. Chem. Lett.* **2012**, *3* (17), 2320–2325.

(42) Matthews, B. M.; Maley, A. M.; Kartub, K. M.; Corn, R. M. Characterizing the Incorporation of DNA into Single NIPAm Hydrogel Nanoparticles with Surface Plasmon Resonance Imaging Measurements. *J. Phys. Chem. C* **2019**, *123* (10), 6090–6096.

(43) Lee, J.; Yang, J.; Kwon, S. G.; Hyeon, T. Nonclassical Nucleation and Growth of Inorganic Nanoparticles. *Nat. Rev. Mater.* **2016**, *1* (8), 16034.

(44) Qiao, L.; Fu, Z.; Li, J.; Ghosen, J.; Zeng, M.; Stebbins, J.; Prasad, P. N.; Swihart, M. T. Standardizing Size- and Shape-Controlled Synthesis of Monodisperse Magnetite (Fe3O4) Nanocrystals by Identifying and Exploiting Effects of Organic Impurities. *ACS Nano* **2017**, *11* (6), 6370–6381.

(45) Peng, Z. A.; Peng, X. Mechanisms of the Shape Evolution of CdSe Nanocrystals. *J. Am. Chem. Soc.* **2001**, *123* (7), 1389–1395.

(46) Tseng, T. Y.; Lin, J. C. Microstructure and Properties of Ni-Zn Ferrites Sintered from Slip Cast Colloidally Precipitated Particles. *IEEE Trans. Magn.* **1989**, *25* (6), 4405–4408.

(47) Kirwan, L. J.; Fawell, P. D.; van Bronswijk, W. In Situ FTIR-ATR Examination of Poly(Acrylic Acid) Adsorbed onto Hematite at Low PH. *Langmuir* **2003**, *19* (14), 5802–5807.

(48) Wu, X.; Ding, Z.; Wang, W.; Song, N.; Khaimanov, S.; Tsidaeva, N. Effect of Polyacrylic Acid Addition on Structure, Magnetic and Adsorption Properties of Manganese Ferrite Nanoparticles. *Powder Technol.* **2016**, *295*, 59–68.

(49) Frey, B. L.; Corn, R. M. Covalent Attachment and Derivatization of Poly(l-Lysine) Monolayers on Gold Surfaces As Characterized by Polarization−Modulation FT-IR Spectroscopy. *Anal. Chem.* **1996**, *68* (18), 3187–3193.

(50) Matthews, B. M. Single-Nanoparticle Microscopy of DNA-Incorporated Hydrogel Nanoparticles, University of California, Irivne, 2019.

Chapter 3

The Reduction of Metal Oxide Nanostructures for LSPR Sensing in the Near Infrared

3.1 Introduction

Nanoparticles and nanostructured films that exhibit plasmon resonance lend themselves well to sensing applications,[1] such as the detection of single molecules,[2] biomarkers of Alzheimer's disease,[3] anthrax,[4] and various other biorecognition events.[5–8] These unique materials exhibit surface plasmon resonance, coherent oscillations of electrons that propagate along a metal/dielectric boundary.[9,10] Their sensing capabilities come from the resonance, or wavelength, of the propagating plasmon that is highly sensitive to changes in the local dielectric environment and will shift as a result.[11–13] In the case of nanoparticles and nanostructures, this resonance is confined locally around the nanomaterial. This localized surface plasmon resonance (LSPR) is still sensitive to change in the local refractive index such as single-layer molecular adsorption.[1,14,15] Additionally, LSPR can be tuned throughout the visible, near-infrared (NIR), and infrared (IR) regions of the electromagnetic spectrum based on the nanostructure's size and shape.[1,15–17]

While the chemical composition of LSPR materials may vary, they all must have a sufficient carrier concentration. Typically, metallic elements such as silver[18–20] and gold[21–23] are used due to their stability and high electron carrier densities - upwards to 10^{23} cm^{-3}.[15,24] Another class of materials that exhibit LSPR behavior is metal oxides, such as tungsten trioxide when in a reduced state (WO_{3-x}).[24–27] Metal oxides do not have the necessary number of free carriers for surface plasmon resonance and must be doped to exhibit more metallic characteristics. Doping can consist of n-type, which adds electrons, or p-type which creates holes; either of which can increase the carrier density anywhere from 10^{18}-10^{22} cm^{-3}.[15,28] One of the benefits of using metal oxides for LSPR materials is that their resonance appears in the NIR as opposed to the visible region many metallic resonances appear in. This allows plasmonic metal oxide nanostructures to

have applications as energy efficient smart windows or in solar energy collection.[15,29] Secondly, these materials can now be tuned on three levels: size, shape, and composition.[15]

Materials fabricated from WO_3 have attracted research interest due to their electrochromic capabilities. Its LSPR can be tuned not only from reduction via oxygen vacancies, but further doped with electrons through intercalation of cations like Li^+.[24,26] Tungsten oxide can also be combined with other metal oxides such as its row two equivalent molybdenum oxide, MoO_3, for improved stability during ion insertion.[30] In this study, a variety of nanostructures were selected to be fabricated out of WO_3 including nanowires, nanorings, and diffraction gratings in hopes of exploring tunable localized surface plasmon resonances in the NIR. All three of these structures can be patterned over large areas with precise control over size parameters like height, width, and periodicity.[31–33] Arrays of nanowires can rapidly be fabricated using lithographically patterned nanowire electrodeposition (LPNE)[34] and have proven to be highly responsive to gases and as biosensors.[35,36] Using a combination of LPNE and colloidal lithography, nanoring arrays can be fabricated over large areas and have grown in popularity as their LSPR can be widely tuned by adjusting their spacing, diameter, and ring width.[32,33,37,38] Diffraction based sensing is the simplest design of the three and has been incorporated into a variety of different sensing applications, from scanners to optical switches, to spectrometers.[39–42] Furthermore, electrochromic materials on the nanoscale are able to bypass electrochromic response limitations found within bulk matter. The small radii of nanostructures and their high surface areas create shorter diffusion path lengths and improved cation mobility; the end result being faster cation insertion for a more rapid electrochromic response.[43,44] We believed combining the tunability of a metal oxide material with the sensitivity of LSPR nanostructures will open the door to devices with greater sensitivity.

3.2 Methods and Materials

3.2.1 List of Materials

Polystyrene beads solutions (2.6% w/v, 1 or 0.5 μm diameter, carboxylate coated) were purchased from Polysciences Inc. Shipley S1808 positive photoresist, Thinner P, and MF-319 developer were purchased from Microchem. Tungsten powder, 10 μ, ≥99.99% trace metal basis was received from Sigma Aldrich. Molybdenum powder, 99.9% metals basis and platinum foil, 99.9% metal basis were received from Alfa Aesar. Nickel pellets were purchased from Kurt J. Lesker Company. A silver/silver chloride standard reference electrode was assembled using a kit acquired from BASi. 30% wt hydrogen peroxide was received from Fisher Chemical. Fisher Premium glass microscope slides (1 mm thick) and Sigma-Aldrich ITO Glass slides (~15-25 Ω/sq cm) were used as substrates. All reagents were used as received unless otherwise noted.

3.2.2 Electrodeposition of Planar WO_3

Using a method adapted from Yan et. al., 1.8 g of tungsten powder was dissolved in a solution of 20 mL hydrogen peroxide and 100 water overnight resulting in a peroxytungstic acid ($H_2W_2O_{11}$) solution.[45] Platinum foil was then added to remove excess hydrogen peroxide from solution. Tungsten oxide was electrodeposited on ITO glass at -0.4 V against a Ag/AgCl reference electrode for 500 to 1000 seconds using a PGSTAT12, Metrohm Autolab with a platinum foil counter electrode.[46]

3.2.3 Electrodeposition of Planar MoO_3-WO_3

A peroxomolybdic acid solution was made by dissolving 115 mg of molybdenum powder into a solution of 20 mL hydrogen peroxide and 100 mL water.[30] Platinum foil was added to remove excess hydrogen peroxide from solution. This solution was mixed with the peroxytungstic acid plating solution to create a mixed solution that is 20% peroxomolybdic acid,

80% peroxytungstic acid. A mixture of tungsten oxide and molybdenum oxide was electrodeposited on ITO glass at -0.5 V for 500 seconds against an Ag/AgCl reference electrode with a platinum foil counter electrode

3.2.5 WO_3 Nanowire Fabrication

WO_3 nanowire arrays were fabricated using previously described LPNE methods.[31,47] First, a layer of nickel was vapor deposited onto clean glass microscope slides. Next, a layer of positive photoresist was spin-coated onto the Ni layer, baked at 90°C for 25 min to evaporate photoresist solvent, and cooled to room temperature. Using a contact photomask, select sections of photoresist were exposed to a UV light source (50 W, Oriel Instruments He(Xe) arc lamp), developed, and then rinsed away. Following, an initial nickel etch was performed to create trenches underneath the photoresist. WO_3 was electrodeposited using the same conditions as planar WO_3, but for various times ranging from 200 to 500 s. Finally, the remaining photoresist and nickel were removed leaving ordered arrays of WO_3 nanowires.

3.2.6 WO_3 Nanoring Fabrication

Nanoring arrays were fabricated using a previously described method that combines LPNE and colloidal lithography.[33] Carboxyl-functionalized polystyrene beads (1 μm in diameter) were spin coated onto a clean microscope slide to form a monolayer of hexagonally close packed beads. These beads were etched by oxygen plasma between 2 and a half minutes to 3 minutes to create an array of smaller beads that retained their hexagonally close packed orientation. Next, a layer of nickel was vapor deposited and the beads were subsequently removed, leaving an array of hexagonally ordered holes. A mixture of 1:1 positive photoresist:thinner P was spin coated onto the glass substrates which were then baked at 90°C for 25 min before cooling to room temperature. The slides were backside exposed through the nanohole array to a UV light. Once

developed, a nanowell array was left on the slide. Electrodeposition of WO_3 was performed using conditions similar to planar WO_3, with an electrodeposition time of 100s. The remaining photoresist was removed, and the nickel etched away to leave an array of nanorings.

3.2.7 WO_3 and MoO_3-WO_3 Gratings Fabrication

S1808 positive photoresist was spincoated onto clean ITO coated glass slides at 2500 rpm for 80 s, baked at 90°C for 25 min, and cooled to room temperature. The photoresist coated glass slides were exposed to a UV lamp source for 3.5 s and patterned using a photomask with 15 μm wide Cr lines and 15 μm glass spacings. The photoresist was then developed for 25 s using MF-319 developer, rinsed with deionized water, and dried under an N2 stream. An electrical contact area was made by dissolving the corner of the photoresist with acetone using a Q-tip. WO_3 was then electrochemically deposited onto the photopatterned ITO substrate using a potentiostat in a three-electrode setup. The working electrode of the photopatterned ITO substrate was exposed to either the peroxytungstic acid plating solution or the mixture of peroxytungstic acid and peroxomolybdic acid for 500 s at a cathodic potential of −0.5 V vs. a Ag/AgCl reference electrode and a Pt counter electrode.

3.2.8 Furnace Reduction

Glass substrates with electrodeposited samples on them were placed in a Paragon SC3 furnace and heated under Formant gas (95% nitrogen and 5% hydrogen) at 550 ºC for 1 to 2 hours.

3.2.9 Characterization of WO_3 and MoO_3-WO_3 Samples

SEM images were obtained using a FEI Magellan 400 field-emission scanning electron microscope at an accelerating voltage of 10 kV. X-ray photoelectron spectroscopy (XPS) measurements were collected using a Kratos Analytical AXIS Supra surface analysis instrument,

with an emission current of 15 mA during analysis. For UV-Vis/NIR absorbance measurements, a Jasco V-670 absorption spectrophotometer was used.

3.3 Results and Discussion

3.3.1 Electrodeposition of Planar WO_3

The mechanism of WO_3 electrodeposition from acidic peroxytungstic acid plating solutions has been explored previously by other researchers.[30,48,49] Many believe electrodeposition begins with the $W_2O_{11}^{-2}$ anion as the starting material as it is the majority peroxytungstate species in acidic solutions.[48] This peroxytungstate ion is then reduced at negative potentials (-0.4 V vs. Ag/AgCl) as described in Equation 1, where x is either 0, 4, or 8. In the case x = 8, all four of the peroxide anions are reduced electrochemically to three O^{2-} ions found within the WO_3 lattice and five H_2O. If x = 0, then the four peroxide anions disproportionate to form three O^{2-} ions, H_2O and two O_2. In addition to electrodeposition, sub-stoichoimetric amounts of hydrogen ions can simultaneously be inserted, reducing W^{VI} ions in the WO_3 lattice to W^{V}. This mixed valent product is supported by the observation of a blue color of the electrodeposited WO_3 film during electrodeposition. However, this reduction is not permanent, as the thin film becomes transparent once electrodeposition has finished.

$$(1)\quad W_2O_{11}^{2-} + (2+x)\,H^+ + xe^- \rightarrow 2WO_3 + \frac{(2+x)}{2}H_2O + \frac{(8-x)}{4}O_2$$

$$(2)\quad zH^+ + WO_3 + ze^- \rightarrow H_zWO_3$$

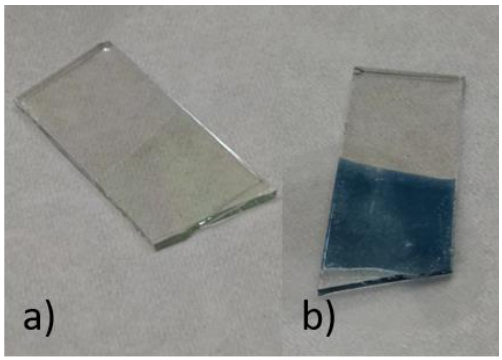

Figure 3.1. Image of electrodeposited WO_3 on ITO glass in its a) oxidized and b) reduced state.

3.3.2 Electrodeposition of Planar MoO_3-WO_3

Although the electrodeposition of tungsten oxide from a mixed plating solution likely occurs in a similar fashion to the mechanism previously described, the molybdenum oxide electrodeposition is slightly more complex.[30,50] While the main species of the plating solution is still a dimeric peroxymolybdate ion ($Mo_2O_{11}^{2-}$), there is also significant presence of molybdic acid (H_2MoO_4).[50] Under these conditions, the electrodeposition of molybdenum oxide at negative potentials (-0.5 vs. Ag/AgCl) from a molybdate plating solution is Equation 3. The resulting molybdenum oxide product is thought to be a mixture of Mo^V and Mo^{VI}: $(MoO_2^+)_2(MoO_4^{2-})$.[50] Reduced molybdenum within the MoO_3-WO_3 lattice could explain why thin films of electrodeposited MoO_3-WO_3 were observed to have a permanently faint blue color (Figure 3.9 a). The blue color is thought to arise from exchange between reduced metal centers and fully oxidized metal centers, in which case Mo^V could be interacting with both Mo^{VI} (Equation 4) and W^{VI} (Equation 5).[27]

$$(3)\quad Mo_2O_{11}^{2-} + H_2MoO_4 + 12H^+ + 10e^- \rightarrow Mo_3O_8 + 7H_2O$$

$$(4)\quad Mo^V + Mo^{VI} + e^- \leftrightarrow Mo^{VI} + Mo^V$$

$$(5)\quad Mo^V + W^{VI} + e^- \leftrightarrow Mo^{VI} + W^V$$

3.3.3 Characterization of WO_3 Nanowire Surfaces

Tungsten oxide nanowires were fabricated using lithographically patterned nanowire electrodeposition. SEM was performed in order to determine the width and periodic spacing of the wires (Figure 3.2 a). Electrodeposition for 200 seconds on a 2x1 cm^2 substrate produced 200 ± 10 nm thick nanowires alternating 4.7 and 10.4 ± .1 μm apart. Nanowires were occasionally continuous across the substrate; however, breaks and gaps were observed throughout. X-ray photoelectron spectroscopy for the W4f core confirmed the presence of tungsten on our substrate. Interestingly, peaks were observed at 36.4 and 34.2 eV, often corresponding to a W^V oxidation state.[51] Unfortunately, this could not be corroborated using UV-vis NIR spectroscopy which revealed no resonances of note (Figure B.1).

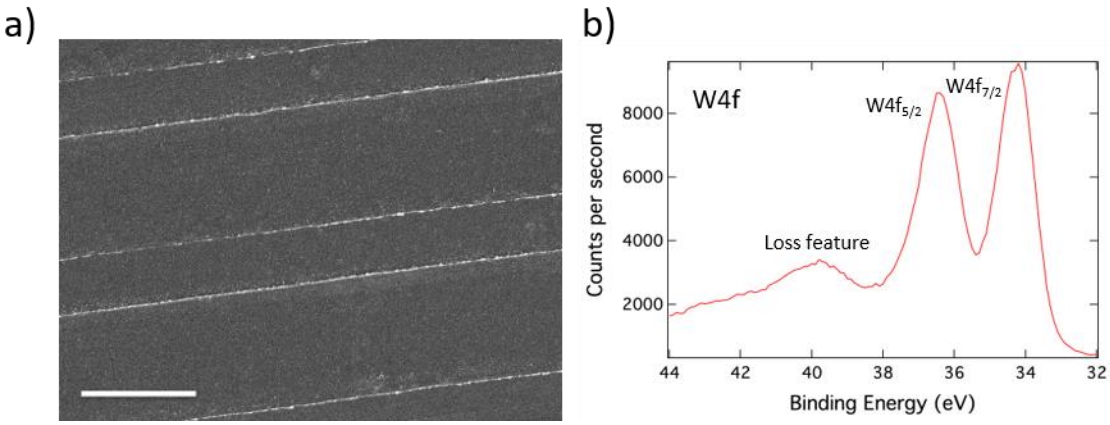

Figure 3.2. a) SEM of 200 ± 10 nm thick WO_3 nanowires alternating 4.7 and 10.4 ± .1 μm apart across a 1x2 cm^2 surface area. Scale bar represents 10 μm. b) XPS spectrum of WO_3 nanowires confirming the presence of W4f peaks at 36.4 and 34.2 eV.

The lack of LSPR signal can likely be attributed to the wide spacing between the wires compared to their thickness and the observed gaps and breaks. Strong LSPR signal requires an optimized packing density of nanostructures, often a distance comparable to the structure's diameter.[52,53] As

our current design results in nanowires spaced three orders of magnitude apart, the dimensions will need to be significantly modified for future studies.

3.3.4 Characterization of WO_3 Nanoring Surfaces

A combination of LPNE and colloidal lithography (using a colloidal mask of 1.0 um polystyrene beads) resulted in a WO_3 nanoring array covering a 1x1 cm^2 substrate. As confirmed by SEM, electrodeposition for 100 seconds produced rings 118 nm thick, about 490 nm in diameter, and 279 nm apart (Figure 3.3 a). X-ray photoelectron spectroscopy for the W4f core confirmed the presence of tungsten within our nanoring array. Though the peaks at 35.7 and 33.5 eV support the presence of W^V, the signal to noise ratio is too poor to conclude a reduced oxidation state with confidence. Despite the improved surface area coverage, the nanoring arrays had no observable LSPR. Further analysis of the SEM image shows poor contrast between the ring and the background, suggesting there is very little metal oxide material on the surface. This is further supported by the small amount of signal seen in the XPS. It could be these rings are not fully formed, but rather just shells outlining the space where the WO_3 would deposit.

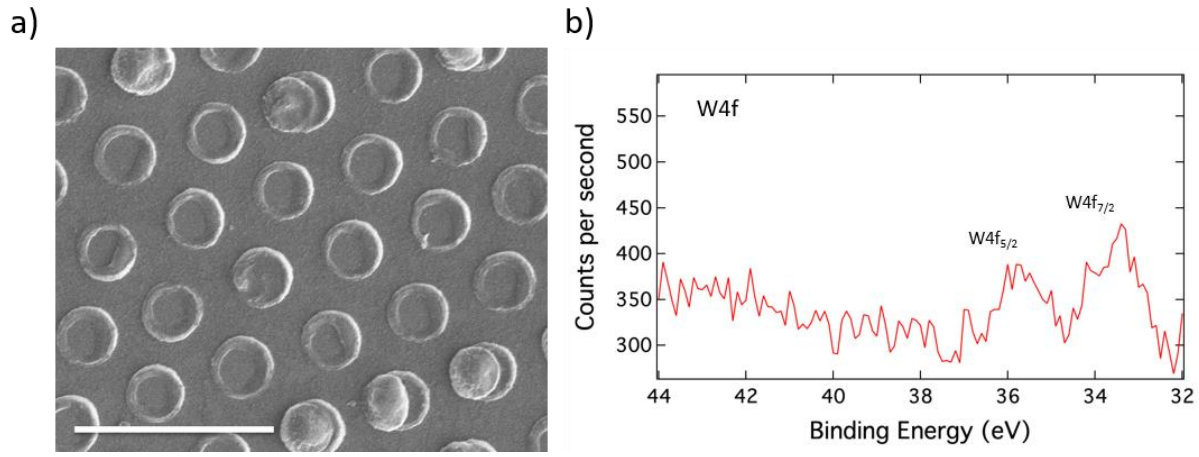

Figure 3.3. a) SEM of 118 nm thick WO_3 nanorings about 490 nm in diameter and 279 nm apart across a 1x1 cm^2 surface area. Scale bar represents 2 μm. b) Survey XPS spectrum of WO_3 nanowires confirming the presence of W4f peaks at 35.7 and 33.5 eV.

3.3.5 Comparison of Furnace Reduced Planar and Nanoring Surfaces

Planar films of WO_3 were heated in a furnace at 550 ºC for one hour under reducing conditions (formant gas). When removed from the furnace, the substrate was observed to be slightly teal in color (Figure 3.4 a). Thinner samples were observed to revert to their original transparent state (Figure 3.1 a) as they would oxidize upon returning to atmospheric conditions; however thicker films (electrodeposited for 1000 seconds) resulting in a more permanent color change. This change in absorbance was reflected in the UV-vis NIR spectra collected. As seen in Figure 3.4 b, reduced WO_3 films (blue) show significantly larger absorption throughout the NIR and visible region up until about 500 nm whereas fully oxidized WO_3 films (red) absorbs strongly throughout the visible region.

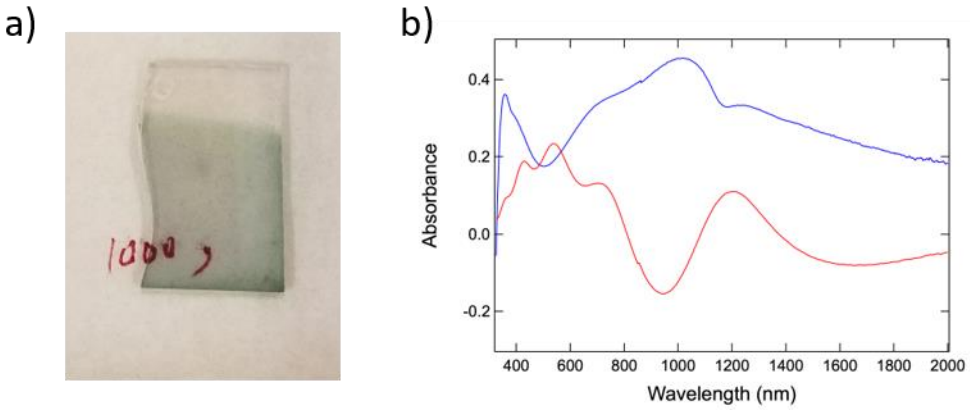

Figure 3.4. a) Image of furnace reduced planar WO_3 on ITO substrate. b) UV-vis NIR spectra of WO_3 before furnace treatment and after. The obtained spectra demonstrate the substrate was likely fully oxidized (red) beforehand and then reduced (blue) after treatment.

XPS spectra (Figure 3.5) comparing the W4f regions (a) before and (b) after furnace treatment show a slight change tungsten oxidation. As expected, planar tungsten oxide films that have not been reduced show peaks at 38.2 and 36.1 eV, the standard binding energy for tungsten in the 6+

oxidation state. After furnace treatment, these peaks were observed to shift down to 37.8 and 35.6 eV and are much broader, implying a mixture of W^{V} and W^{VI} within the thin film.[51]

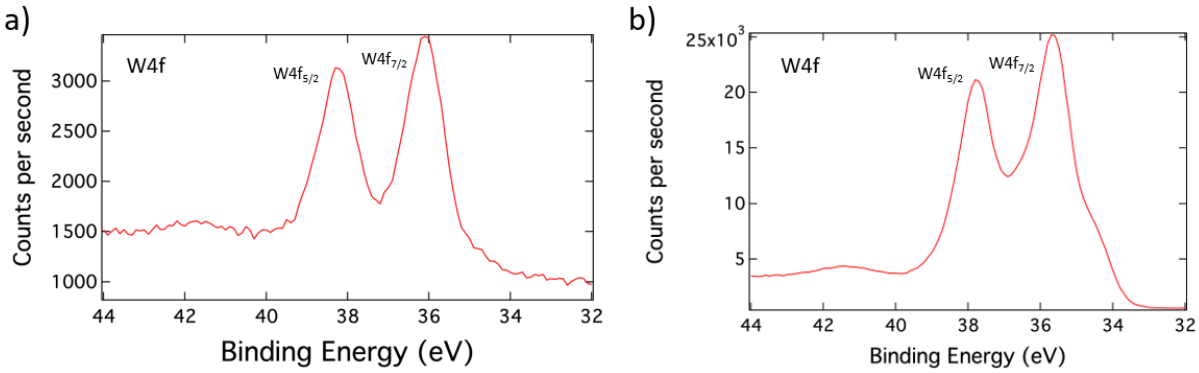

Figure 3.5. Comparison of XPS spectra for a) fully oxidized planar WO_3 and b) furnace reduced planar WO_3. Fully oxidized WO_3 shows W4f peaks at 38.2 and 36.1 eV as expected for W^{VI}. The broadened and slightly downshifted W4f peaks at 37.8 and 35.6 eV suggest there is a mix of W^{VI} and W^{V} within the thin film after furnace treatment.

When a similar treatment was applied to WO_3 nanorings, the nanostructures degraded as seen in Figure 3.6. Even shortening the treatment time to 1 hour produced similar results. Though the furnace was a viable option for planar WO3 reduction, it seems the nanorings are too delicate to be reduced in this fashion.

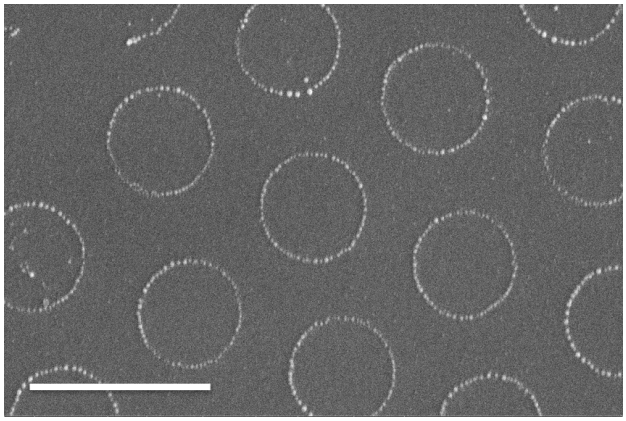

Figure 3.6. SEM image of WO_3 nanorings after being heated in furnace at 550°C for 1 hour under formant gas. Scale bar represents 1 μm.

3.3.6 Comparison of WO_3 and MoO_3-WO_3 Planar Surfaces

To improve the structure and stability of electrodeposited nanostructures, a mixture of MoO_3 and WO_3 was electrodeposited onto ITO glass at negative potentials (-0.5 V vs. Ag/AgCl). SEM images of planar WO_3 reveal a cracked surface, but the mixture of MoO_3 and WO_3 planar films were observed to electrodeposit more smoothly. WO_3 is often polycrystalline, resulting in multiple phases such as monoclinic and triclinic; the strain between these heterogenous phases likely caused the thin film surface to crack.[30] The addition of metal oxides like molybdenum is thought to help reduce the observed cracking and can improve structural lifetime during lithium ion insertion.[30] Molybdenum oxide that has been sintered at high temperatures results in an intermixed α-/β-MoO_3 structure. It was reasoned that the presence of β-MoO_3 can stabilize α-MoO_3 by reducing electrochemically induced structural changes.[30] Mixing MoO_3 with WO_3 may create a more homogeneous material that can electrodeposit more smoothly.

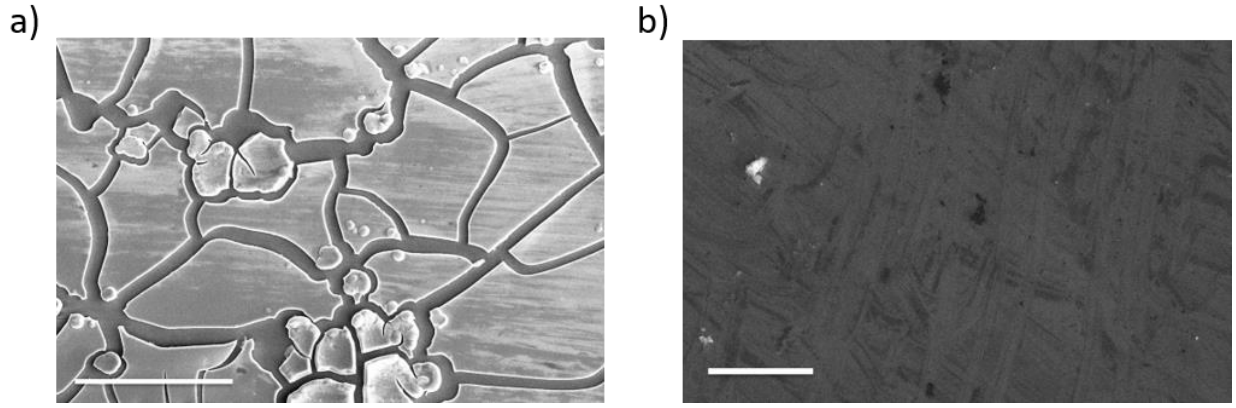

Figure 3.7. a) SEM image of electrodeposited planar WO_3. Scale bar represents 30 μm. b) SEM image of electrodeposited planar MoO_3-WO_3. Scale bar represents 1 μm.

Characterization by XPS confirmed both the presence of WO_3 and MoO_3 within the mixed thin film. W4f peaks appeared at 37.5 and 35.5 eV and Mo3d peaks appeared at 235.7 and 232.6 eV. Compared to the standard peaks for fully oxidized tungsten (38.3 and 36.1 eV) and molybdenum (236.2 and 233.1 eV) both sets of observed peaks are slightly downshifted, leading us to believe the MoO_3-WO_3 system is in a slightly reduced oxidation state. As mentioned previously, MoO_3 likely electrodeposits as a mixture of both Mo^{V} and Mo^{VI}, and the reduced Mo^{V} is then free to interact with and reduce the W^{VI} within the crystal lattice. A slightly reduced MoO_3-WO_3 system is further supported by its spectroscopic characterization, which shows a strong absorption from the NIR into the visible region (Figure 3.8 b).

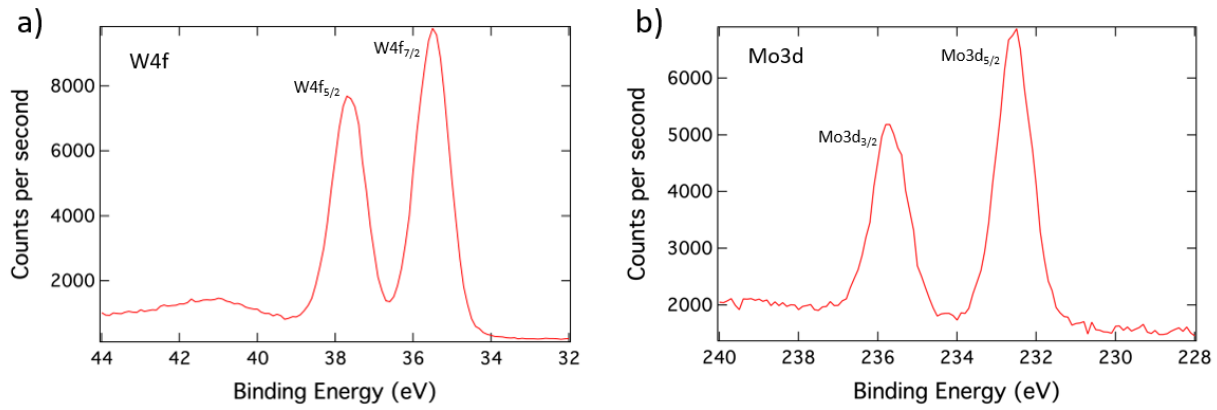

Figure 3.8. XPS spectrum of electrodeposited planar MoO_3-WO_3 confirming the presence of a) slightly reduced WO_3 with peaks appearing at 37.5 and 35.5 eV in the W4f region and b) slightly reduced MoO_3 with peaks appearing at 235.7 and 232.6 eV in the Mo3d region.

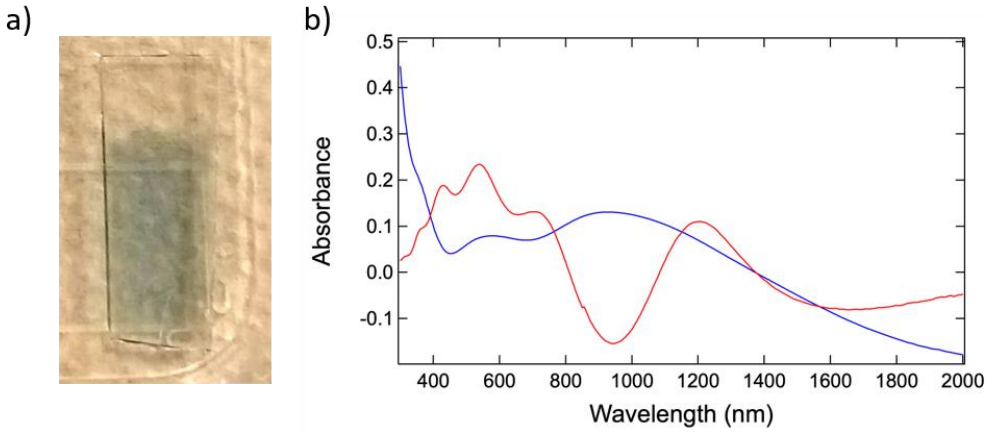

Figure 3.9. a) Image of MoO_3-WO_3 electrodeposited on ITO glass. b) UV-vis NIR spectra of electrodeposited planar WO_3 (red) compared to electrodeposited planar MoO_3-WO_3 (blue).

3.3.7 Comparison of WO_3 and MoO_3-WO_3 Diffraction Gratings

Diffraction gratings made from MoO_3-WO_3 electroplating solution demonstrated improved structural stability compared to WO_3 diffraction gratings. As seen in Figure 3.10, the SEM image of the WO_3 (a) has significantly less contrast when compared to that of MoO_3-WO_3 (b). This implies that the MoO_3-WO_3 has a sharper feature, likely because a thicker grating was electrodeposited. As seen with previously deposited arrays of nanowires and nanorings, WO_3 did not deposit a sufficient amount of material, leading to poor spectroscopic characteristics (Figure 3.11). However, spectroscopic behavior similar to planar MoO_3-WO_3 was observed in the MoO_3-WO_3 diffraction gratings which displayed a permanent blue color and improved absorption throughout the visible and NIR regions up to around 500 nm (Figure 3.11). The XPS data for MoO_3-WO_3 diffraction gratings compared to WO3 diffraction gratings matched previously acquired data from planar samples. MoO_3-WO_3 diffraction gratings showed slightly reduced tungsten and molybdenum peaks at 37.7 and 35.6 eV and 235.8 and 232.6 eV respectively whereas the WO_3 had peaks at 38.2 and 36 eV, corresponding to fully oxidized W^{VI} (Figure B.2).

If the MoO_3-WO_3 electroplating solution was applied to arrays of nanowires and nanorings, we hope to observe similarly improved structures as well as a permanently reduced state, possibly leading to a strong LSPR.

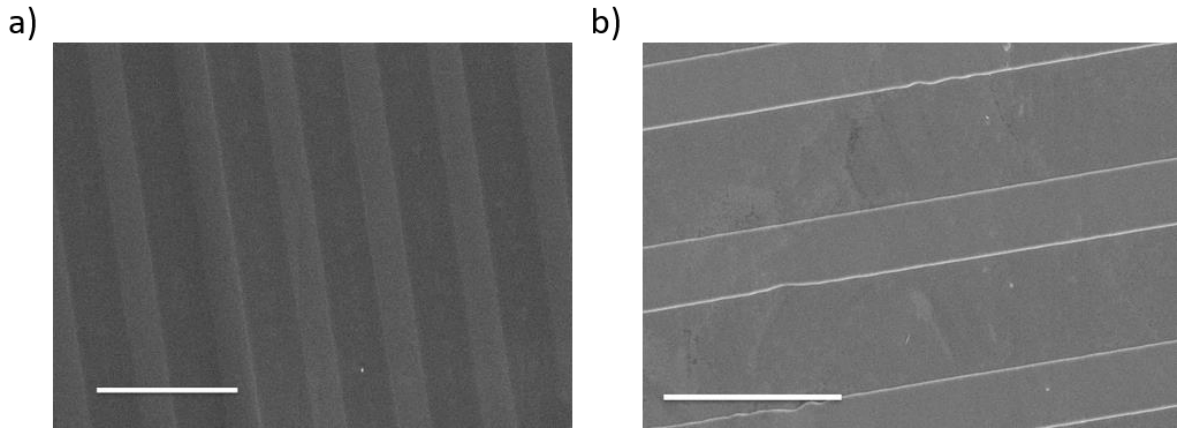

Figure 3.10. a) SEM image of electrodeposited WO_3 diffraction gratings. Scale bar represents 50 μm. b) SEM image of electrodeposited MoO3-WO_3 diffraction gratings. Scale bar represents 30 μm.

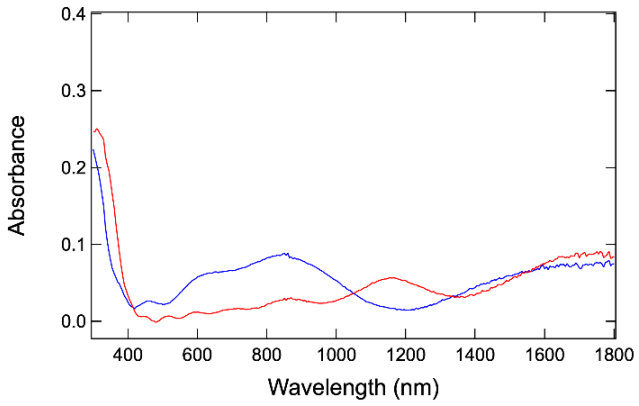

Figure 3.11. UV-vis NIR spectrum of electrodeposited WO_3 diffraction gratings (red) and of electrodeposited MoO_3-WO_3 diffraction gratings (blue).

3.4 Conclusion

In summary, we demonstrated the fabrication of nanowire, nanoring, and diffraction gratings using WO_3 and MoO_3-WO_3. Nanostructures electrodeposited from WO_3 in their unmodified states did not display LSPR and we turned to several methods in order to create permanent reduced states within the WO_3 crystal lattice. Although a permanently reduced thin film of WO3 was successfully achieved using a furnace, nanostructured WO_3 was too delicate to undergo similar treatment. To improve the stability, we explored mixing MoO_3 within the WO_3 crystal lattice. Electrodeposited thin films and diffraction gratings using a MoO_3-WO_3 plating solution showed improved structures and strongly suggest permanent oxygen vacancies within the lattice due to a mixture of Mo^{V} and Mo^{VI} metal centers. Although the work here did not lead to nanostructure devices with tunable LSPR, WO_3 was successfully incorporated into diffraction gratings that explored the enhancement of electrodiffraction from the incorporation of nanostructured ZnO.[54]

3.5 Acknowledgements

This work was supported by the National Science Foundation through grant CHE-1403506. SEM analyses were performed at the UC Irvine Materials Research Institute (IMRI) at UC Irvine. XPS work was performed at the UC Irvine Materials Research Institute using instrumentation funded in part by the National Science Foundation Major Research Instrumentation Program under grant no. CHE-1338173. UV-vis/NIR measurements were performed at the UC Irvine Laser and Spectroscopy lab.

3.6 References

(1) Willets, K. A.; Van Duyne, R. P. Localized Surface Plasmon Resonance Spectroscopy and Sensing. *Annu. Rev. Phys. Chem.* **2007**, *58* (1), 267–297.

(2) Nie, S.; Emory, S. R. Probing Single Molecules and Single Nanoparticles by Surface-Enhanced Raman Scattering. *Science (80-.).* **1997**, *275* (5303), 1102 LP – 1106.

(3) Haes, A. J.; Chang, L.; Klein, W. L.; Van Duyne, R. P. Detection of a Biomarker for Alzheimer's Disease from Synthetic and Clinical Samples Using a Nanoscale Optical Biosensor. *J. Am. Chem. Soc.* **2005**, *127* (7), 2264–2271.

(4) Zhang, X.; Young, M. A.; Lyandres, O.; Van Duyne, R. P. Rapid Detection of an Anthrax Biomarker by Surface-Enhanced Raman Spectroscopy. *J. Am. Chem. Soc.* **2005**, *127* (12), 4484–4489.

(5) Endo, T.; Kerman, K.; Nagatani, N.; Takamura, Y.; Tamiya, E. Label-Free Detection of Peptide Nucleic Acid−DNA Hybridization Using Localized Surface Plasmon Resonance Based Optical Biosensor. *Anal. Chem.* **2005**, *77* (21), 6976–6984.

(6) Endo, T.; Yamamura, S.; Nagatani, N.; Morita, Y.; Takamura, Y.; Tamiya, E. Localized Surface Plasmon Resonance Based Optical Biosensor Using Surface Modified Nanoparticle Layer for Label-Free Monitoring of Antigen–Antibody Reaction. *Sci. Technol. Adv. Mater.* **2005**, *6* (5), 491–500.

(7) Englebienne, P. Use of Colloidal Gold Surface Plasmon Resonance Peak Shift to Infer Affinity Constants from the Interactions between Protein Antigens and Antibodies Specific for Single or Multiple Epitopes. *Analyst* **1998**, *123* (7), 1599–1603.

(8) Raschke, G.; Kowarik, S.; Franzl, T.; Sönnichsen, C.; Klar, T. A.; Feldmann, J.; Nichtl, A.; Kürzinger, K. Biomolecular Recognition Based on Single Gold Nanoparticle Light Scattering. *Nano Lett.* **2003**, *3* (7), 935–938.

(9) Spoto, G.; Minunni, M. Surface Plasmon Resonance Imaging: What Next? *J. Phys. Chem. Lett.* **2012**, *3* (18), 2682–2691.

(10) Smith, E. A.; Corn, R. M. Surface Plasmon Resonance Imaging as a Tool to Monitor Biomolecular Interactions in an Array Based Format. *Appl. Spectrosc.* **2003**, *57* (11), 320A-332A.

(11) Kelly, K. L.; Coronado, E.; Zhao, L. L.; Schatz, G. C. The Optical Properties of Metal Nanoparticles: The Influence of Size, Shape, and Dielectric Environment. *J. Phys. Chem. B* **2003**, *107* (3), 668–677.

(12) Miller, M. M.; Lazarides, A. A. Sensitivity of Metal Nanoparticle Surface Plasmon Resonance to the Dielectric Environment. *J. Phys. Chem. B* **2005**, *109* (46), 21556–21565.

(13) Jensen, T. R.; Duval, M. L.; Kelly, K. L.; Lazarides, A. A.; Schatz, G. C.; Van Duyne, R. P. Nanosphere Lithography: Effect of the External Dielectric Medium on the Surface Plasmon Resonance Spectrum of a Periodic Array of Silver Nanoparticles. *J. Phys. Chem. B* **1999**, *103* (45), 9846–9853.

(14) Haes, A. J.; Van Duyne, R. P. A Unified View of Propagating and Localized Surface Plasmon Resonance Biosensors. *Anal. Bioanal. Chem.* **2004**, *379* (7), 920–930.

(15) Agrawal, A.; Johns, R. W.; Milliron, D. J. Control of Localized Surface Plasmon Resonances in Metal Oxide Nanocrystals. *Annu. Rev. Mater. Res.* **2017**, *47* (1), 1–31.

(16) Nehl, C. L.; Hafner, J. H. Shape-Dependent Plasmon Resonances of Gold Nanoparticles. *J. Mater. Chem.* **2008**, *18* (21), 2415–2419.

(17) Sherry, L. J.; Chang, S.-H.; Schatz, G. C.; Van Duyne, R. P.; Wiley, B. J.; Xia, Y. Localized Surface Plasmon Resonance Spectroscopy of Single Silver Nanocubes. *Nano Lett.* **2005**, *5* (10), 2034–2038.

(18) Martinsson, E.; Shahjamali, M. M.; Enander, K.; Boey, F.; Xue, C.; Aili, D.; Liedberg, B. Local Refractive Index Sensing Based on Edge Gold-Coated Silver Nanoprisms. *J. Phys. Chem. C* **2013**, *117* (44), 23148–23154.

(19) Wiley, B. J.; Chen, Y.; McLellan, J. M.; Xiong, Y.; Li, Z.-Y.; Ginger, D.; Xia, Y. Synthesis and Optical Properties of Silver Nanobars and Nanorice. *Nano Lett.* **2007**, *7* (4), 1032–1036.

(20) Mock, J. J.; Barbic, M.; Smith, D. R.; Schultz, D. A.; Schultz, S. Shape Effects in Plasmon Resonance of Individual Colloidal Silver Nanoparticles. *J. Chem. Phys.* **2002**, *116* (15), 6755–6759.

(21) Chen, H.; Shao, L.; Li, Q.; Wang, J. Gold Nanorods and Their Plasmonic Properties. *Chem. Soc. Rev.* **2013**, *42* (7), 2679–2724.

(22) Tanaka, A.; Hashimoto, K.; Kominami, H. Preparation of Au/CeO2 Exhibiting Strong Surface Plasmon Resonance Effective for Selective or Chemoselective Oxidation of Alcohols to Aldehydes or Ketones in Aqueous Suspensions under Irradiation by Green Light. *J. Am. Chem. Soc.* **2012**, *134* (35), 14526–14533.

(23) Becker, J.; Trügler, A.; Jakab, A.; Hohenester, U.; Sönnichsen, C. The Optimal Aspect Ratio of Gold Nanorods for Plasmonic Bio-Sensing. *Plasmonics* **2010**, *5* (2), 161–167.

(24) Manthiram, K.; Alivisatos, A. P. Tunable Localized Surface Plasmon Resonances in Tungsten Oxide Nanocrystals. *J. Am. Chem. Soc.* **2012**, *134* (9), 3995–3998.

(25) Cheng, H.; Wen, M.; Ma, X.; Kuwahara, Y.; Mori, K.; Dai, Y.; Huang, B.; Yamashita, H. Hydrogen Doped Metal Oxide Semiconductors with Exceptional and Tunable Localized Surface Plasmon Resonances. *J. Am. Chem. Soc.* **2016**, *138* (29), 9316–9324.

(26) Mattox, T. M.; Bergerud, A.; Agrawal, A.; Milliron, D. J. Influence of Shape on the Surface Plasmon Resonance of Tungsten Bronze Nanocrystals. *Chem. Mater.* **2014**, *26* (5), 1779–1784.

(27) Johansson, M. B.; Kristiansen, P. T.; Duda, L.; Niklasson, G. A.; Österlund, L. Band Gap States in Nanocrystalline WO3thin Films Studied by Soft X-Ray Spectroscopy and Optical Spectrophotometry. *J. Phys. Condens. Matter* **2016**, *28* (47), 475802.

(28) Donovan, B. F.; Sachet, E.; Maria, J.-P.; Hopkins, P. E. Interplay between Mass-Impurity and Vacancy Phonon Scattering Effects on the Thermal Conductivity of Doped Cadmium Oxide. *Appl. Phys. Lett.* **2016**, *108* (2), 21901.

(29) Granqvist, C. G. Transparent Conductors as Solar Energy Materials: A Panoramic Review. *Sol. Energy Mater. Sol. Cells* **2007**, *91* (17), 1529–1598.

(30) Kondrachova, L.; Hahn, B. P.; Vijayaraghavan, G.; Williams, R. D.; Stevenson, K. J. Cathodic Electrodeposition of Mixed Molybdenum Tungsten Oxides from Peroxo-Polymolybdotungstate Solutions. *Langmuir* **2006**, *22* (25), 10490–10498.

(31) Menke, E. J.; Thompson, M. A.; Xiang, C.; Yang, L. C.; Penner, R. M. Lithographically Patterned Nanowire Electrodeposition. *Nat. Mater.* **2006**, *5* (11), 914–919.

(32) Halpern, A. R.; Corn, R. M. Lithographically Patterned Electrodeposition of Gold, Silver, and Nickel Nanoring Arrays with Widely Tunable Near-Infrared Plasmonic Resonances. *ACS Nano* **2013**, *7* (2), 1755–1762.

(33) Toma, M.; Cho, K.; Wood, J. B.; Corn, R. M. Gold Nanoring Arrays for Near Infrared Plasmonic Biosensing. *Plasmonics* **2014**, *9* (4), 765–772.

(34) Xiang, C.; Kung, S.-C.; Taggart, D. K.; Yang, F.; Thompson, M. A.; Güell, A. G.; Yang, Y.; Penner, R. M. Lithographically Patterned Nanowire Electrodeposition: A Method for Patterning Electrically Continuous Metal Nanowires on Dielectrics. *ACS Nano* **2008**, *2* (9), 1939–1949.

(35) Loget, G.; Corn, R. M. Silica Nanowire Arrays for Diffraction-Based Bioaffinity Sensing. *Chem. – A Eur. J.* **2014**, *20* (34), 10802–10810.

(36) Halpern, A. R.; Nishi, N.; Wen, J.; Yang, F.; Xiang, C.; Penner, R. M.; Corn, R. M. Characterization of Electrodeposited Gold and Palladium Nanowire Gratings with Optical Diffraction Measurements. *Anal. Chem.* **2009**, *81* (14), 5585–5592.

(37) Aizpurua, J.; Hanarp, P.; Sutherland, D. S.; Käll, M.; Bryant, G. W.; García de Abajo, F. J. Optical Properties of Gold Nanorings. *Phys. Rev. Lett.* **2003**, *90* (5), 57401.

(38) Cai, Y.; Li, Y.; Nordlander, P.; Cremer, P. S. Fabrication of Elliptical Nanorings with Highly Tunable and Multiple Plasmonic Resonances. *Nano Lett.* **2012**, *12* (9), 4881–4888.

(39) Zahid Yaqoob, N. A. R. Passive Optics No-Moving-Parts Barcode Scanners. *IEEE Photonics Technol. Lett.* **2004**, *16*, 954–956.

(40) Glesk, I.; Bock, P. J.; Cheben, P.; Schmid, J. H.; Lapointe, J.; Janz, S. All-Optical Switching Using Nonlinear Subwavelength Mach-Zehnder on Silicon. *Opt. Express* **2011**, *19* (15), 14031–14039.

(41) Hossain, M. A.; Canning, J.; Cook, K.; Jamalipour, A. Smartphone Laser Beam Spatial Profiler. *Opt. Lett.* **2015**, *40* (22), 5156–5159.

(42) Kondrachova, L. V; May, R. A.; Cone, C. W.; Vanden Bout, D. A.; Stevenson, K. J. Evaluation of Lithium Ion Insertion Reactivity via Electrochromic Diffraction-Based Imaging. *Langmuir* **2009**, *25* (4), 2508–2518.

(43) Lee, S.-H.; Deshpande, R.; Parilla, P. A.; Jones, K. M.; To, B.; Mahan, A. H.; Dillon, A. C. Crystalline WO3 Nanoparticles for Highly Improved Electrochromic Applications. *Adv. Mater.* **2006**, *18* (6), 763–766.

(44) Runnerstrom, E. L.; Llordés, A.; Lounis, S. D.; Milliron, D. J. Nanostructured Electrochromic Smart Windows: Traditional Materials and NIR-Selective Plasmonic Nanocrystals. *Chem. Commun.* **2014**, *50* (73), 10555–10572.

(45) Yan, C.; Kang, W.; Wang, J.; Cui, M.; Wang, X.; Foo, C. Y.; Chee, K. J.; Lee, P. S. Stretchable and Wearable Electrochromic Devices. *ACS Nano* **2014**, *8* (1), 316–322.

(46) Ling, H.; Lu, J.; Phua, S.; Liu, H.; Liu, L.; Huang, Y.; Mandler, D.; Lee, P. S.; Lu, X. One-Pot Sequential Electrochemical Deposition of Multilayer Poly(3,4-Ethylenedioxythiophene):Poly(4-Styrenesulfonic Acid)/Tungsten Trioxide Hybrid Films and Their Enhanced Electrochromic Properties. *J. Mater. Chem. A* **2014**, *2* (8), 2708–2717.

(47) Halpern, A. R.; Donavan, K. C.; Penner, R. M.; Corn, R. M. Wafer-Scale Fabrication of Nanofluidic Arrays and Networks Using Nanoimprint Lithography and Lithographically Patterned Nanowire Electrodeposition Gold Nanowire Masters. *Anal. Chem.* **2012**, *84* (11), 5053–5058.

(48) Meulenkamp, E. A. Mechanism of WO 3 Electrodeposition from Peroxy-Tungstate Solution. *J. Electrochem. Soc.* **1997**, *144* (5), 1664–1671.

(49) Cai, G.; Cui, M.; Kumar, V.; Darmawan, P.; Wang, J.; Wang, X.; Lee-Sie Eh, A.; Qian, K.; Lee, P. S. Ultra-Large Optical Modulation of Electrochromic Porous WO3 Film and the Local Monitoring of Redox Activity. *Chem. Sci.* **2016**, *7* (2), 1373–1382.

(50) McEvoy, T. M.; Stevenson, K. J. Electrochemical Quartz Crystal Microbalance Study of the Electrodeposition Mechanism of Molybdenum Oxide Thin Films from Peroxo-Polymolybdate Solution. *Anal. Chim. Acta* **2003**, *496* (1), 39–51.

(51) Mews, M.; Korte, L.; Rech, B. Oxygen Vacancies in Tungsten Oxide and Their Influence on Tungsten Oxide/Silicon Heterojunction Solar Cells. *Sol. Energy Mater. Sol. Cells* **2016**, *158*, 77–83.

(52) Fong, K. E.; Yung, L.-Y. L. Localized Surface Plasmon Resonance: A Unique Property of Plasmonic Nanoparticles for Nucleic Acid Detection. *Nanoscale* **2013**, *5* (24), 12043–12071.

(53) Kuznetsov, A. S. Effect of Proximity in Arrays of Plasmonic Nanoantennas on Hot Spots Density: Degenerate Semiconductors vs. Conventional Metals. *Plasmonics* **2016**, *11* (6), 1487–1493.

(54) Fung, H. W. M.; So, S.; Kartub, K.; Corn, R. M. Quantitative Characterization of Optical Coupling in Nanoporous ZnO–WO3 and ZnO–PEDOT Composite Electrodeposited Gratings Using Electrodiffraction Measurements. *J. Phys. Chem. C* **2019**, *123* (1), 762–769.

Chapter 4

Characterization of DNA-Nanogold Conjugates by Electron Microscopy.

4.1 Introduction

The controlled assembly of gold and other nanoparticles into specific patterns and arrangements has generated significant interest as these assemblies can display new electronic, magnetic, and optical properties different from either individual samples or bulk materials of the same composition.[1–4] DNA-DNA hybridization reactions have been demonstrated to be a reliable method to direct ensembles of gold nanoparticles into specific patterns.[2,4–7] One of the most established methods to attach DNA to gold nanoparticles is with the addition of a thiol moiety to the end of a DNA strand, which will orient the nucleotide perpendicular to the nanoparticle surface and leave it available for further hybridization.[5,7–9] These patterns and structures are often referred to as "programmable materials" because the end shape can reliably be predicted through the specific design of DNA linkers.[4,7] Examples of DNA directed nanoparticle designs include linear arrays,[10,11] 2D arrays,[4,12] 3D lattices,[13–15] and tripods.[16] However, in order to design improved DNA-mediated nanoparticle assemblies, it is of the utmost importance to understand the structure of the DNA-gold interaction.[2,17]

With its ability to visualize biological samples with a resolution as far down as 2 Å, cryo-electron microscopy (EM) has revolutionized the way we determine the structures of biological samples.[18,19] One of the major benefits of cryo-EM compared to x-ray crystallography, is that it can analyze samples that cannot be isolated in sufficient quantity or do not readily produce crystals, such as flexible DNA conjugates.[2,18,20] Since its development, cryo-EM has been used to visualize a variety of biological samples including viruses,[21,22] ribosomes,[23] enzymes,[24,25] and DNA.[2,26] In particular, cyro-EM has been used to reconstruct DNA arrangements of 10 nm gold particles.[27,28] Additionally, the 3D structure of hybridized DNA-nanogold conjugates have been successfully reconstructed using a combination of negative-staining, individual-particle electron

tomography, and cryo-EM.[2] However, the structural determination of nanogold, in particular of water-soluble nanogold[17] or of nanogold bound to DNA,[2] is limited. This chapter presents our progress in developing improved methodologies to characterize DNA-gold interactions at small masses using cryo-EM. 1.4 nm sized nanogold clusters (NG) were selected for analysis as clusters this small have not been structurally characterized when bound to DNA. Second, while several lengths of DNA were considered, the design used in this work is a simple 60 base pair dimer with a dithiol group attached to the 3′ end of the oligo chain for adsorption to the nanogold surface.[5,8,9] The two DNA sequences in Table 4.1, T7 and 3598, will undergo a kinase reaction to form the self-complementary sequence 3598/T7.

Table 4.1. List of DNA sequences

Name	DNA Sequence
T7	5′- TCT CCC TAT AGT GAG TCG TAT TAG -3′ (SS)
3598	5′- CTA ATA CGA CTC ACT ATA GGG AGA GGG AAA TTT CCC – 3′
3598/T7	5′- CTA ATA CGA CTC ACT ATA GGG AGA GGG AAA TTT CCC TCT CCC TAT AGT GAG TCG TAT TAG -3′ (SS)

To successfully recreate 3D structures from 2D images of biological samples, several key experimental designs must be considered. First, to withstand the high vacuum and radiation damage of electron microscopes, biological samples are frozen in vitreous ice before imaging.[29,30] The resulting frozen-hydrated molecules have been demonstrated to preserve their native structure and can successfully be imaged without dehydration and frozen-hydrated molecules show reduced radiation damage.[19,30,31] Second, large ensembles of samples must be imaged using a low dose (~400 $e^-/Å^2$), to further reduce radiation damage, such that all possible orientations are found.[19,32] These 2D projections are classified into groups by orientation and can then be combined to generate a 3D reconstruction of the sample at atomic level resolution.[19,33]

Despite ice encasement, there is potential for motion and blurring due to the beam striking the sample.[32] The solution to this is to use a high frame rate (10-40 frames per second) camera that outputs "movies" of particles.[32] This shortens the amount of time a sample needs to be exposed to the beam, limiting the amount of motion, while still taking the number of images required for reconstruction later on. Finally, smaller objects have a low signal-to-noise ratio that makes determining the particle's orientation during reconstruction difficult.[32] The proposed solution is to use a K2 detector that reduces both detection and readout noise.[32] The K2 detector detects peak electron density and accumulates electron events over time. By relying on primary electrons, rather than integrating charge, the detector can significantly reduce detection and readout noise

4.2 Materials and Methods

4.2.1 List of Materials

All DNA oligomers were synthesized and purchased from Integrated DNA Technologies. T4 DNA Ligase buffer (10X), T4 DNA Ligase, T4 Polynucleotide Kinase Buffer (10X), T4 Polynucleotide Kinase, and the base-pair ladder were all received from New England Biolabs. Sephedex G-10 and Tris buffer (Trizma hydrochloride; pH 7.5) were received from Sigma. Nanopure water was filtered using a Milli-Q water purification system (Millipore). The mini-columns (without media or buffer) used to perform a Sephedex G-10 ion exchange were purchased from USA Scientific. Agarose (molecular biology grade) was ordered from Fisher Bioreagents. TBE Buffer (UltraPure 10X) was received from Thermo Fisher Scientific and diluted to 0.5X concentration. Ethidium bromide was received from Invitrogen. Non-functionalized nanogold (NG) and monoamino nanogold (NG+), was acquired from Nanoprobes

and suspended in water for further use. The nanogold concentration was determined using a ND-1000 Nanodrop Spectrophotometer (Thermo Fisher Scientific) and observing the absorbance at 420 nm. At this wavelength, NG^+ has an extinction coefficient of $1.6 \times 10^5\ M^-\ cm^-$ and NG has an extinction coefficient of $1.12 \times 10^5\ M^-\ cm^-$. TEM grids TEM grids (copper grids with formvar, stabilized with carbon, 400 mesh and Quantifoil R2/2) were received from Ted Pella. All chemicals were used as received unless otherwise noted.

4.2.2 Synthesis of 3598/T7 DNA

A 50 μL solution of 2 μM oligo was made in a small eppendorf tube by first combining 1 μL of T7 (100 μM) and 10 uL of 3598 (10 μM) together. To this, 5 μL of T4 DNA ligase buffer with ATP and 5 μL of PNK ligase buffer were added. The solution was brought to 48 μL by adding 27 μL of nanopure water. Then the solution was heated at 70 °C for 5 minutes using a C1000 Touch Thermal Cycler (Bio Rad). After cooling to room temperature, 1 μL of PNK enzyme and 1 μL of DNA ligase was added. The solution was then incubated overnight cycling between 37 °C for 2 minutes and 16 °C for two minutes. To remove excess DDT from PNK buffer the solution was run through a Sephedex column. The column was prepared by adding 0.8 mL of G-10 (in TE buffer) Sephedex to a mini-column and spinning it down at 8000 rcf for 30 seconds and tossing the flow through. Then the 50 μL of solution was added to the column and were run through by spinning the column under the same conditions and collecting the flow through. A 1 μL sample of solution was run through a gel to confirm oligo ligation. The remainder was mixed with NG^+ in a 1:1 ratio and analyzed using cyro-EM.

4.2.3 Gel of 3598/T7

A 3% agarose gel was prepared by adding 1.5 g of agarose to 50 mL 0.5X Tris Borate EDTA (TBE) buffer. The solution was microwaved for approximately 1 minute or until the

agarose was suspended in solution. In order to visualize the DNA, the gel was stained with a small amount of ethidium bromide. The hot solution was then poured into a gel mold, a gel comb was added, and allowed to solidify. Once solidified, the gel and mold were placed into a gel electrophoresis apparatus containing 0.5X TBE running buffer. DNA samples - ligation reaction, 3598 control, T7 control - were mixed with bromophenol blue and then loaded into the wells alongside a 50 base pair (bp) reference ladder. Electrophoresis was performed at 300 V and 400 mA using a PowerPac (Bio Rad) power supply for 7 minutes for sufficient separation. After 7 minutes, the gel was removed, and the image was captured with a Nikon D500 under UV light.

4.2.4 Electron Microscope Analysis

A nanogold sample was prepared for TEM by dissolving a small fraction of nanogold in water. 4 uL of sample was applied to a copper TEM grid and allowed to dry. The high-angle annular dark field (HAADF) and bright field (BF) images of nanogold samples were acquired using JEOL Grand ARM TEM/STEM operated at 300 kV STEM mode. The acquired images of nanogold were then processed to render their structure in 3D. Using the program cisTEM, a computational imaging system for TEM, particles within the images were first manually selected. Once a large enough population was selected, the particles were classified into groups with the same orientation. These classifications were then iteratively refined such that a 2D projection of the electron density was obtained.

Cryo-EM - DNA+NG images were obtained on a Cryo-TEM image using 3μL of concentrated sample solution applied on a glow-discharged Quantifoil grid and then loaded on Leica EMGP plunger (Leica Biosystem). The grid was quickly plunged into liquid propane after blotting away the excess liquid and the DNA+NG were then embedded in a thin layer of vitrified ice on the grid. The cryo-grid was then transferred into a JEM-2100F electron microscope using

a Gatan cryo-transfer holder (Gatan, Inc). The electron microscope was operated at 200KV with a field emission gun and specimen was examined under minimum dose system. The images were recorded on a OneView camera (Gatan, Inc.) at 50,000X magnification, corresponding to 0.19 nm per pixel at specimen space.

4.3 Results and Discussion

4.3.1 Synthesis of 3598/T7

A 60 bp oligonucleotide was successfully synthesized by performing a kinase reaction, which replaces the hydroxyl group from the 3´ end of strand 3598 with a phosphate group. The resulting 3598/T7 strand is a self-complementary oligo, and the ligation could occur simultaneously by heating the solution in the presence of both PNK enzyme and DNA ligase. As a final step, the resulting sample was quickly run through an ion exchange column to remove excess DTT which would otherwise degrade the nanogold. To confirm the success of our DNA synthesis, a gel was performed. The synthesized oligo was compared to a 50 bp ladder. As seen from Figure 4.1, a band is clearly visible just above the 50 bp marker, confirming the presence of a larger oligo likely around 60 bp. This gel was also run with a T7 and 3598 control which were observed to appear well below the other markers, as expected for smaller strands.

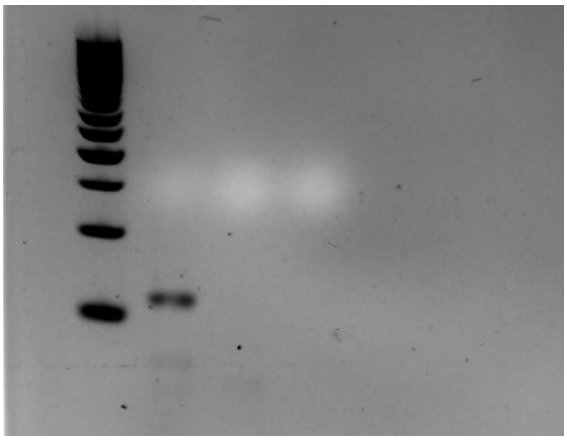

Figure 4.1. Agarose gel under UV light. The well next to the 50 bp ladder is the fully ligated 3598/T7 sequence. Control runs of 3598 and T7 were run in the following two wells.

4.3.2. TEM of Nanogold

TEM micrographs of NG were taken to confirm their size and structure. Clusters of gold atoms were observed to average 1.4 nm in diameter; however, several clusters of smaller and larger sizers were also noted (Figure 4.2). This is likely a result of beam-induced Ostwald ripening, as seen from the small bright spots observed between clusters.[34] These bright points about 1.6 Å in diameter and are likely gold atoms caught in the process of diffusing from cluster to cluster, resulting in the range of cluster sizes observed. Clusters appear to range from 5 to 7 atoms across, suggesting the arrangement of these atoms is similar to that described by Azubel et. al. They describe a 68-atom arrangement as a 13-atom cuboctahedron with one atom in the center and 24 atoms extending in a face-centered cubic framework from the cuboctahedron.[17] The remaining 31 atoms arrange themselves around the framework without any apparent symmetry.

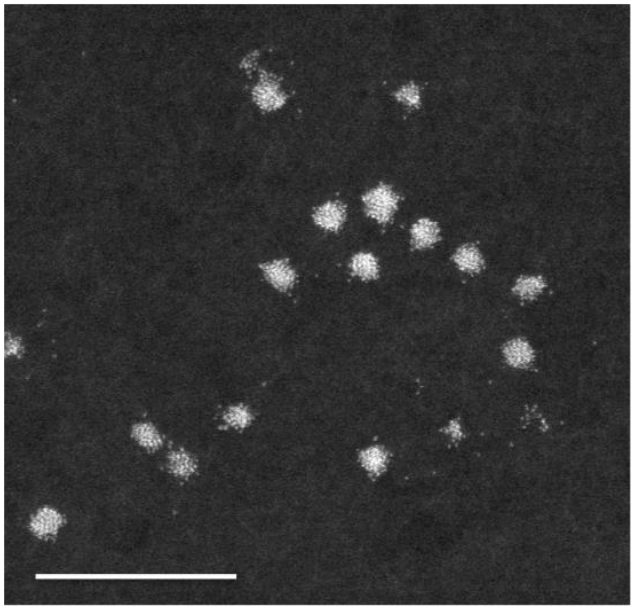

Figure 4.2. Dark field image of 1.4 nm nanogold. Free atoms are believed to be a result from beam induced Ostwald ripening. Scale bar represents 10 nm.

Using the computational imaging program cisTEM, we began the process to render a 3D structure of our nanogold sample using the TEM images. First, particles within the images were manually selected (Figure 4.3 a) and then classified into groups by their orientation. These classifications were then iteratively refined to reduce background noise and produce a 2D projection of the electron density was obtained (Figure 4.3 b). At this point, a 3D image of the nanogold can be reconstructed. Unfortunately, computational power has limited the reconstruction of NG. Additional processing power is needed to resolve structures, and efforts are being made to do so.

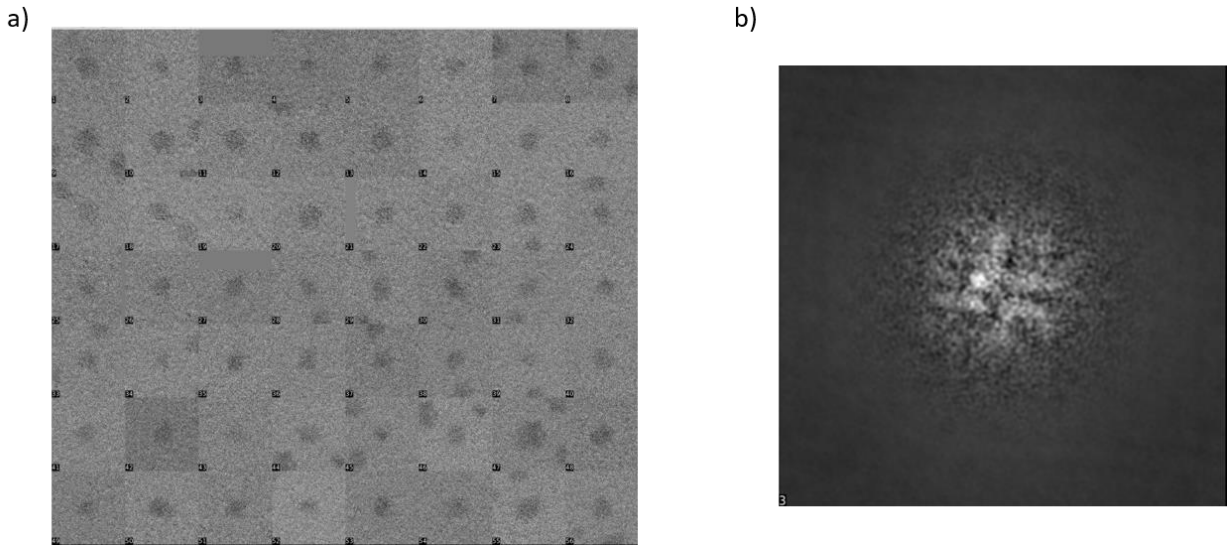

Figure 4.3. a) Sample particle picking of nanogold from TEM micrograph. b) After a correction the particles were aligned to a common center for 3D reconstruction via an iterative refinement process in the cisTEM program.

4.3.3 Cryo-EM Characterization of T7/3598 + NG^+

Initial cryo-EM data shows the presence of NG^+ in high concentration (Figure 4.5). There appear to be domains of NG^+ throughout the sample; several sample domains have been circled in yellow (Figure 4.4 a-e). The likelihood that some of the spacing between nanogold clusters are caused by DNA is high, but it is near impossible to determine which pairs of nanogolds are linked together. Focusing in on some of the more organized arrangements, it is clear that these NG^+ are packed too densely to be tethered to their neighbors by the same DNA, which at 60 bp long should be around 20.4 nm in length. Using the gray value line profile intensities in ImageJ particle distances were determined as seen in Figure 4.5 (original line profiles can be seen in C.1), the majority of the intensities are seen to occur much closer than 20.4 nm apart. Only the sample in Figure 4.5 c shows a length close to 20.4 nm. We believe the

high density of nanogold is caused in part, by the nature of the cryo-EM detector. Because this image is a 2D projection, objects that are far apart in the z-axis will appear closer together once compressed into a 2D image on the x- and y-axes. A second experimental consideration for future work is to work with a less concentrated sample. Thus far, efforts to limit the stoichiometric amounts of NG^+ compared to oligo or reducing the concentration of the sample loaded onto the grid have had mixed results and a sample preparation method still needs to be optimized. Once a reliable method for sample preparation has been optimized, structural analysis can move forward. Data will be collected on a K3 camera, which can give improved signal-to-noise ratios compared to a CCD camera.[32]

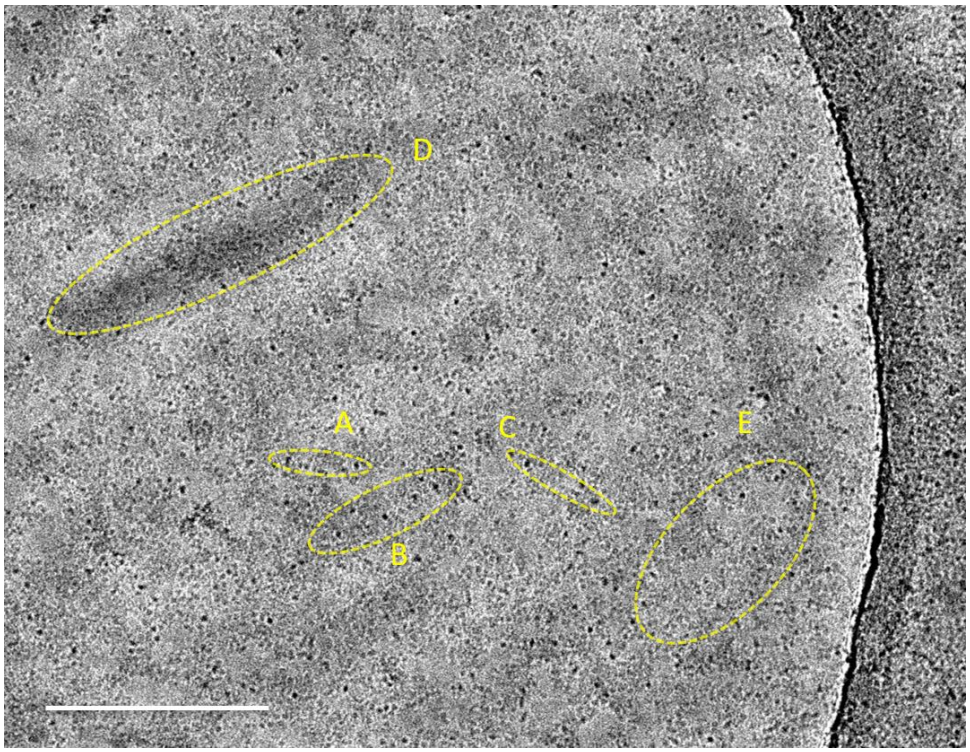

Figure 4.4. CCD micrograph taken on a cryo-EM of 3598/T7 oligonucleotide bound to NG^+. Potential domains of NG^+ arrangements have been highlighted by a yellow ring. Scale bar represents 50 nm.

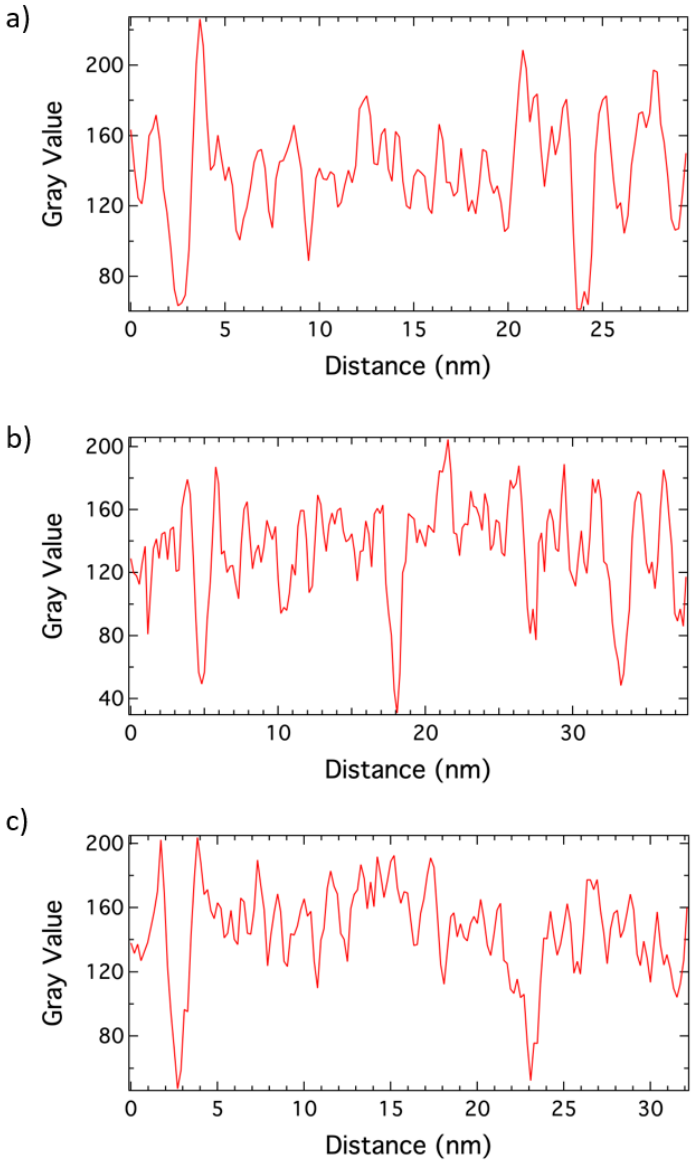

Figure 4.5. The intensity of NG^+ as measured using ImageJ. Intensities correlate to the nanogold found within circles a, b, and c in Figure 4.4. Original line profiles can be found in Appendix C Figure C.1.

4.4 Conclusion

Despite the relatively simple design of the experiment, it is the sample preparation and data processing that has proven tricky and requires improvement. Although DNA appears to

have successfully attached to nanogold clusters, the samples are far too concentrated for the cryo-EM as seen the densely populated projections acquired. Additionally, the method for analyzing and rendering the DNA-NG bond into a 3D reconstruction is still an ongoing process. Once the sample preparation has been optimized, it will be easier to find potential samples to pick particles from for refinement and reconstruction.

4.5 Acknowledgements

This work was supported by the National Science Foundation through grant CHE-1403506. TEM and cryo-EM analyses were performed at the UC Irvine Materials Research Institute (IMRI). The author would like to thank Dr. Mingjie Xu for his help obtaining TEM images and Dr. Li Xing for her extensive help obtaining and analyzing cryo-EM measurements.

4.6 References

(1) Nie, Z.; Petukhova, A.; Kumacheva, E. Properties and Emerging Applications of Self-Assembled Structures Made from Inorganic Nanoparticles. *Nat. Nanotechnol.* **2010**, *5* (1), 15–25.

(2) Zhang, L.; Lei, D.; Smith, J. M.; Zhang, M.; Tong, H.; Zhang, X.; Lu, Z.; Liu, J.; Alivisatos, A. P.; Ren, G. Three-Dimensional Structural Dynamics and Fluctuations of DNA-Nanogold Conjugates by Individual-Particle Electron Tomography. *Nat. Commun.* **2016**, *7* (1), 11083.

(3) Elghanian, R.; Storhoff, J. J.; Mucic, R. C.; Letsinger, R. L.; Mirkin, C. A. Selective Colorimetric Detection of Polynucleotides Based on the Distance-Dependent Optical Properties of Gold Nanoparticles. *Science (80-.).* **1997**, *277* (5329), 1078 LP – 1081.

(4) Zheng, J.; Constantinou, P. E.; Micheel, C.; Alivisatos, A. P.; Kiehl, R. A.; Seeman, N. C. Two-Dimensional Nanoparticle Arrays Show the Organizational Power of Robust DNA Motifs. *Nano Lett.* **2006**, *6* (7), 1502–1504.

(5) Mirkin, C. A.; Letsinger, R. L.; Mucic, R. C.; Storhoff, J. J. A DNA-Based Method for Rationally Assembling Nanoparticles into Macroscopic Materials. *Nature* **1996**, *382* (6592), 607–609.

(6) Alivisatos, A. P.; Johnsson, K. P.; Peng, X.; Wilson, T. E.; Loweth, C. J.; Bruchez, M. P.; Schultz, P. G. Organization of "nanocrystal Molecules" Using DNA. *Nature* **1996**, *382* (6592), 609–611.

(7) Jones, M. R.; Seeman, N. C.; Mirkin, C. A. Programmable Materials and the Nature of the DNA Bond. *Science (80-.).* **2015**, *347* (6224), 1260901.

(8) Dubois, L. H.; Nuzzo, R. G. Synthesis, Structure, and Properties of Model Organic Surfaces. *Annu. Rev. Phys. Chem.* **1992**, *43* (1), 437–463.

(9) Bain, C. D.; Whitesides, G. M. Formation of Two-Component Surfaces by the Spontaneous Assembly of Monolayers on Gold from Solutions Containing Mixtures of Organic Thiols. *J. Am. Chem. Soc.* **1988**, *110* (19), 6560–6561.

(10) Xiao, S.; Liu, F.; Rosen, A. E.; Hainfeld, J. F.; Seeman, N. C.; Musier-Forsyth, K.; Kiehl, R. A. Selfassembly of Metallic Nanoparticle Arrays by DNA Scaffolding. *J. Nanoparticle Res.* **2002**, *4* (4), 313–317.

(11) Le, J. D.; Pinto, Y.; Seeman, N. C.; Musier-Forsyth, K.; Taton, T. A.; Kiehl, R. A. DNA-Templated Self-Assembly of Metallic Nanocomponent Arrays on a Surface. *Nano Lett.* **2004**, *4* (12), 2343–2347.

(12) Shiraishi, S.; Yu, L.; Akiyama, Y.; Wang, G.; Kikitsu, T.; Miyamura, K.; Takarada, T.; Maeda, M. Folding of Nanoparticle Chains into 2D Arrays: Structural Change of DNA-Functionalized Gold Nanoparticle Assemblies. *Adv. Mater. Interfaces* **2018**, *5* (13), 1800189.

(13) Zhang, T.; Hartl, C.; Frank, K.; Heuer-Jungemann, A.; Fischer, S.; Nickels, P. C.; Nickel, B.; Liedl, T. 3D DNA Origami Crystals. *Adv. Mater.* **2018**, *30* (28), 1800273.

(14) Tian, Y.; Zhang, Y.; Wang, T.; Xin, H. L.; Li, H.; Gang, O. Lattice Engineering through Nanoparticle–DNA Frameworks. *Nat. Mater.* **2016**, *15*, 654.

(15) Ji, M.; Ma, N.; Tian, Y. 3D Lattice Engineering of Nanoparticles by DNA Shells. *Small* **2019**, *15* (26), 1805401.

(16) Zhan, P.; Dutta, P. K.; Wang, P.; Song, G.; Dai, M.; Zhao, S.-X.; Wang, Z.-G.; Yin, P.; Zhang, W.; Ding, B.; et al. Reconfigurable Three-Dimensional Gold Nanorod Plasmonic Nanostructures Organized on DNA Origami Tripod. *ACS Nano* **2017**, *11* (2), 1172–1179.

(17) Azubel, M.; Koivisto, J.; Malola, S.; Bushnell, D.; Hura, G. L.; Koh, A. L.; Tsunoyama, H.; Tsukuda, T.; Pettersson, M.; Häkkinen, H.; et al. Electron Microscopy of Gold Nanoparticles at Atomic Resolution. *Science (80-.).* **2014**, *345* (6199), 909 LP – 912.

(18) Nogales, E.; Scheres, S. H. W. Cryo-EM: A Unique Tool for the Visualization of Macromolecular Complexity. *Mol. Cell* **2015**, *58* (4), 677–689.

(19) Cheng, Y. Single-Particle Cryo-EM at Crystallographic Resolution. *Cell* **2015**, *161* (3), 450–457.

(20) Kühlbrandt, W. The Resolution Revolution. *Science (80-.).* **2014**, *343* (6178), 1443 LP – 1444.

(21) Zhang, X.; Jin, L.; Fang, Q.; Hui, W. H.; Zhou, Z. H. 3.3 Å Cryo-EM Structure of a Nonenveloped Virus Reveals a Priming Mechanism for Cell Entry. *Cell* **2010**, *141* (3), 472–482.

(22) Yu, X.; Ge, P.; Jiang, J.; Atanasov, I.; Zhou, Z. H. Atomic Model of CPV Reveals the Mechanism Used by This Single-Shelled Virus to Economically Carry Out Functions Conserved in Multishelled Reoviruses. *Structure* **2011**, *19* (5), 652–661.

(23) Amunts, A.; Brown, A.; Toots, J.; Scheres, S. H. W.; Ramakrishnan, V. The Structure of the Human Mitochondrial Ribosome. *Science (80-.).* **2015**, *348* (6230), 95 LP – 98.

(24) Vinothkumar, K. R.; Zhu, J.; Hirst, J. Architecture of Mammalian Respiratory Complex I. *Nature* **2014**, *515*, 80.

(25) Bai, X.; Yan, C.; Yang, G.; Lu, P.; Ma, D.; Sun, L.; Zhou, R.; Scheres, S. H. W.; Shi, Y. An Atomic Structure of Human γ-Secretase. *Nature* **2015**, *525*, 212.

(26) Bai, X.; Martin, T. G.; Scheres, S. H. W.; Dietz, H. Cryo-EM Structure of a 3D DNA-Origami Object. *Proc. Natl. Acad. Sci.* **2012**, *109* (49), 20012 LP – 20017.

(27) Tian, Y.; Wang, T.; Liu, W.; Xin, H. L.; Li, H.; Ke, Y.; Shih, W. M.; Gang, O. Prescribed Nanoparticle Cluster Architectures and Low-Dimensional Arrays Built Using Octahedral DNA Origami Frames. *Nat. Nanotechnol.* **2015**, *10*, 637.

(28) Lermusiaux, L.; Funston, A. M. Plasmonic Isomers via DNA-Based Self-Assembly of Gold Nanoparticles. *Nanoscale* **2018**, *10* (41), 19557–19567.

(29) Dubochet, J.; Lepault, J.; Freeman, R.; Berriman, J. A.; Homo, J.-C. Electron Microscopy of Frozen Water and Aqueous Solutions. *J. Microsc.* **1982**, *128* (3), 219–237.

(30) Taylor, K. A.; Glaeser, R. M. Electron Microscopy of Frozen Hydrated Biological Specimens. *J. Ultrastruct. Res.* **1976**, *55* (3), 448–456.

(31) Stark, H.; Zemlin, F.; Boettcher, C. Electron Radiation Damage to Protein Crystals of Bacteriorhodopsin at Different Temperatures. *Ultramicroscopy* **1996**, *63* (2), 75–79.

(32) Li, X.; Mooney, P.; Zheng, S.; Booth, C. R.; Braunfeld, M. B.; Gubbens, S.; Agard, D. A.; Cheng, Y. Electron Counting and Beam-Induced Motion Correction Enable near-Atomic-Resolution Single-Particle Cryo-EM. *Nat. Methods* **2013**, *10*, 584.

(33) Frank, J.; Verschoor, A.; Boublik, M. Computer Averaging of Electron Micrographs of 40S Ribosomal Subunits. *Science (80-.).* **1981**, *214* (4527), 1353 LP – 1355.

(34) Yoshida, K.; Bright, A.; Tanaka, N. Direct Observation of the Initial Process of Ostwald Ripening Using Spherical Aberration-Corrected Transmission Electron Microscopy. *J. Electron Microsc. (Tokyo).* **2012**, *61* (2), 99–103.

Appendix A

Supporting Information for Synthesis and Functionalization of Ferrite Nanoparticles for Biological Applications

A.1 TEM Micrograph of Ferrite Nanoparticles and its Diffraction Pattern

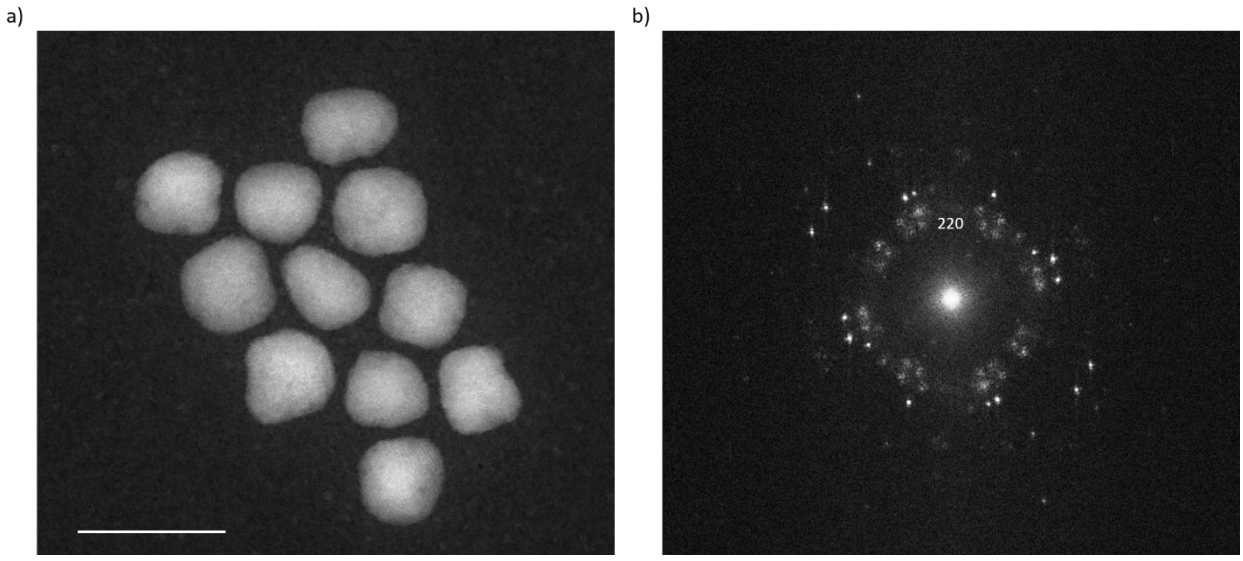

Figure A.1. a) TEM micrograph of a sample 10 nm ferrite population taken on a Grand Arm JEOL 300 TEM. Scale bar represents 20 nm. b) A diffraction pattern obtained by performing an FFT on the TEM micrograph with the 220 ring identified.

A.2 Table of Fe/Mn, Fe/Zn, and Mn/Zn Ratios

Table A.1. Comparison of the starting ratio and final ratios of Fe/Mn, Fe/Zn, and Mn/Zn as determined by EDS.

	Starting Ratio	10 nm Ferrite	40 nm Ferrite
Fe/Mn	2.8/1	4.8/1	11.7/1
Fe/Zn	4/1	6.5/1	9.8/1
Mn/Zn	1.4/1	1.3/1	0.83/1

A.3 FTIR Spectra Comparing PAA-Ferrites

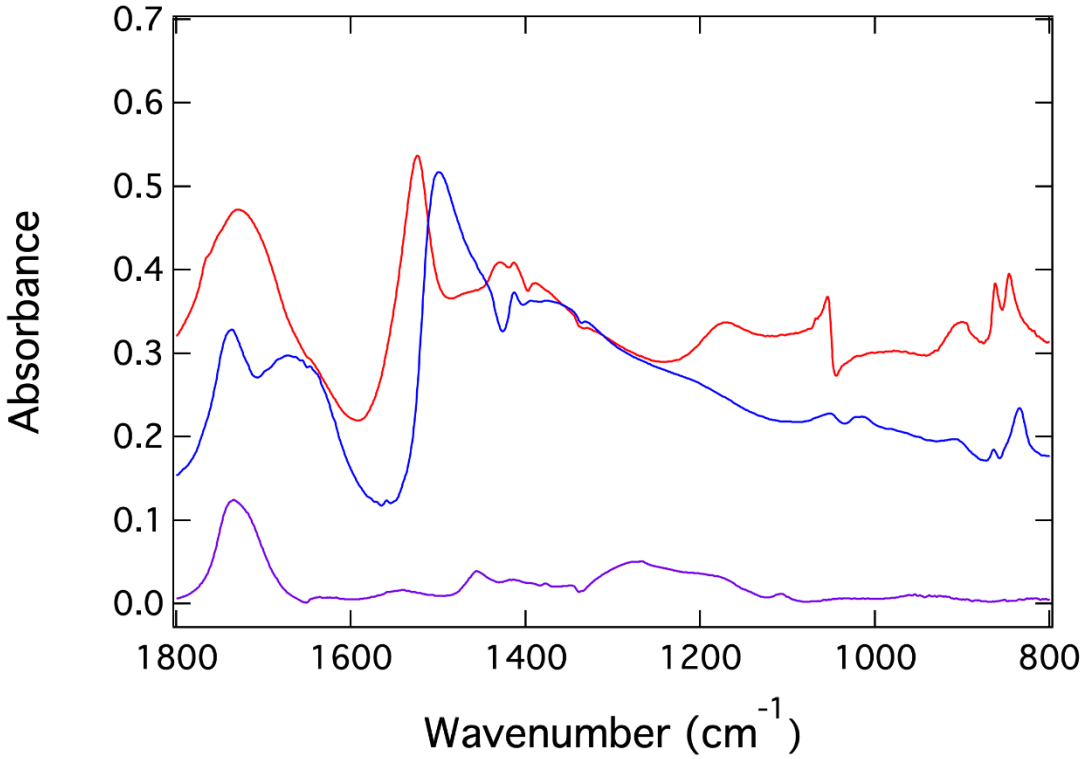

Figure A.2. FTIR spectra of polyacrylic acid (purple) polyacrylic acid coated 40 nm ferrites (red) and polyacrylic acid coated 10 nm ferrites (blue).

A.4 FTIR Spectra Comparing pLys-PAA-Ferrites

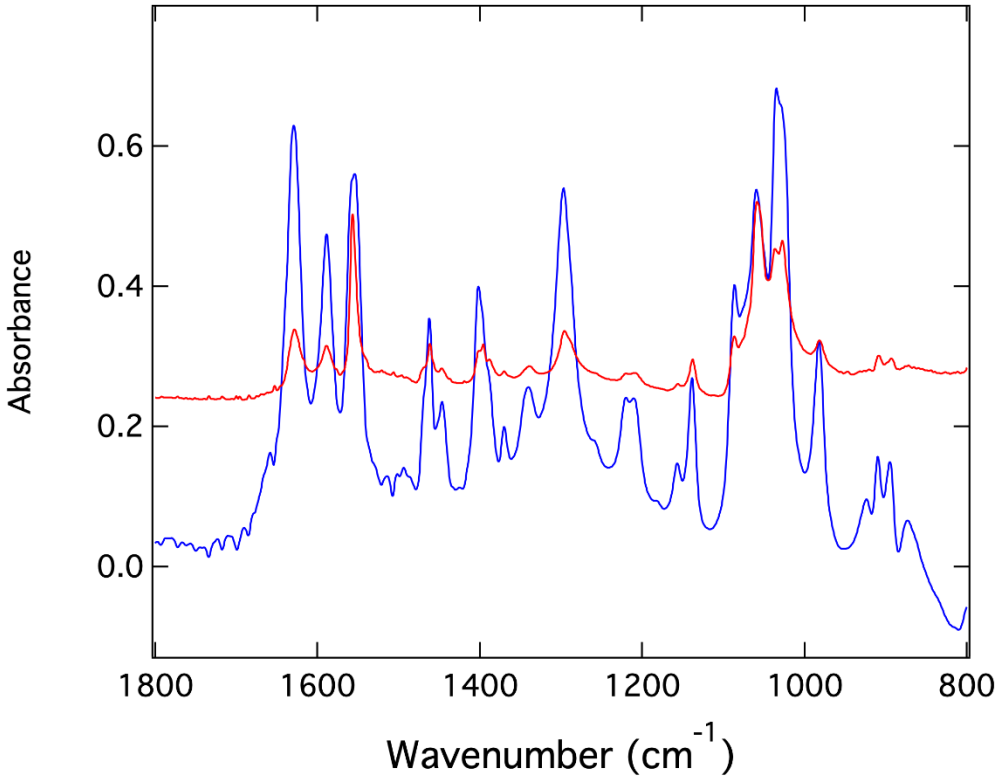

Figure A.3. Comparison FTIR spectra of large ferrites (red) and small ferrites (blue) that have been coated in PAA and then electrostatically wrapped in pLys.

Appendix B

Supporting Information for The Reduction of Metal Oxide Nanostructures for LSPR Sensing in the Near Infrared

B.1 Representative UV-vis NIR of WO_3 Nanowires and Nanorings

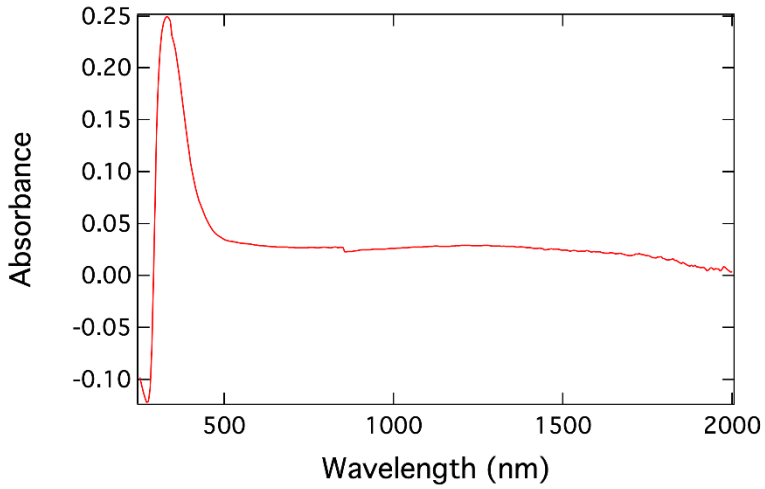

Figure B.1. Sample UV-vis NIR spectrum demonstrating the spectroscopic characteristics of both WO_3 nanowire arrays and nanoring arrays.

B.2 XPS Spectrum of WO_3 Diffraction Gratings

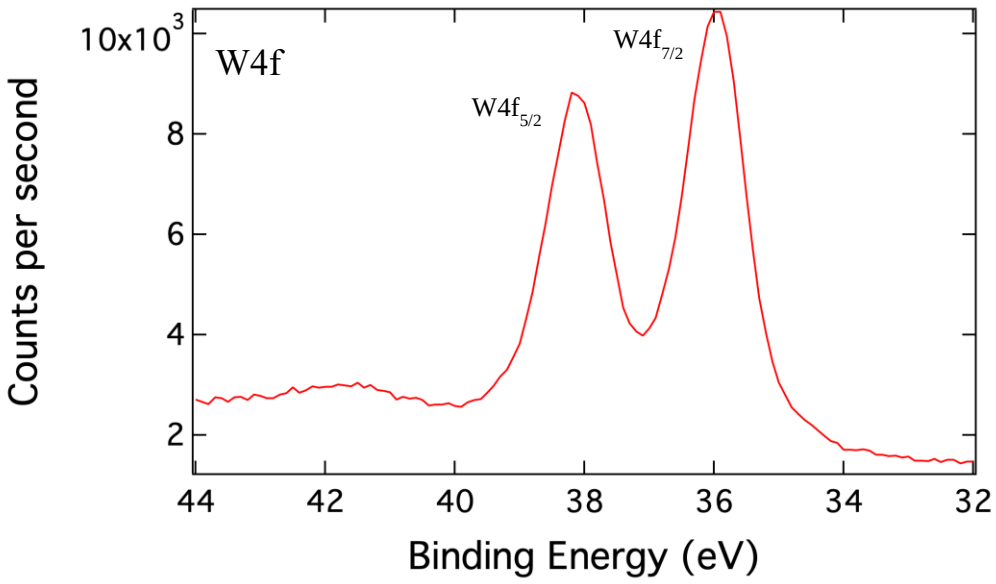

Figure B.2. XPS spectrum WO_3 diffraction gratings shows W4f peaks at 38.2 and 36.1 eV as expected for W^{VI}.

B.3 XPS Spectrum of MoO_3-WO_3 Diffraction Gratings

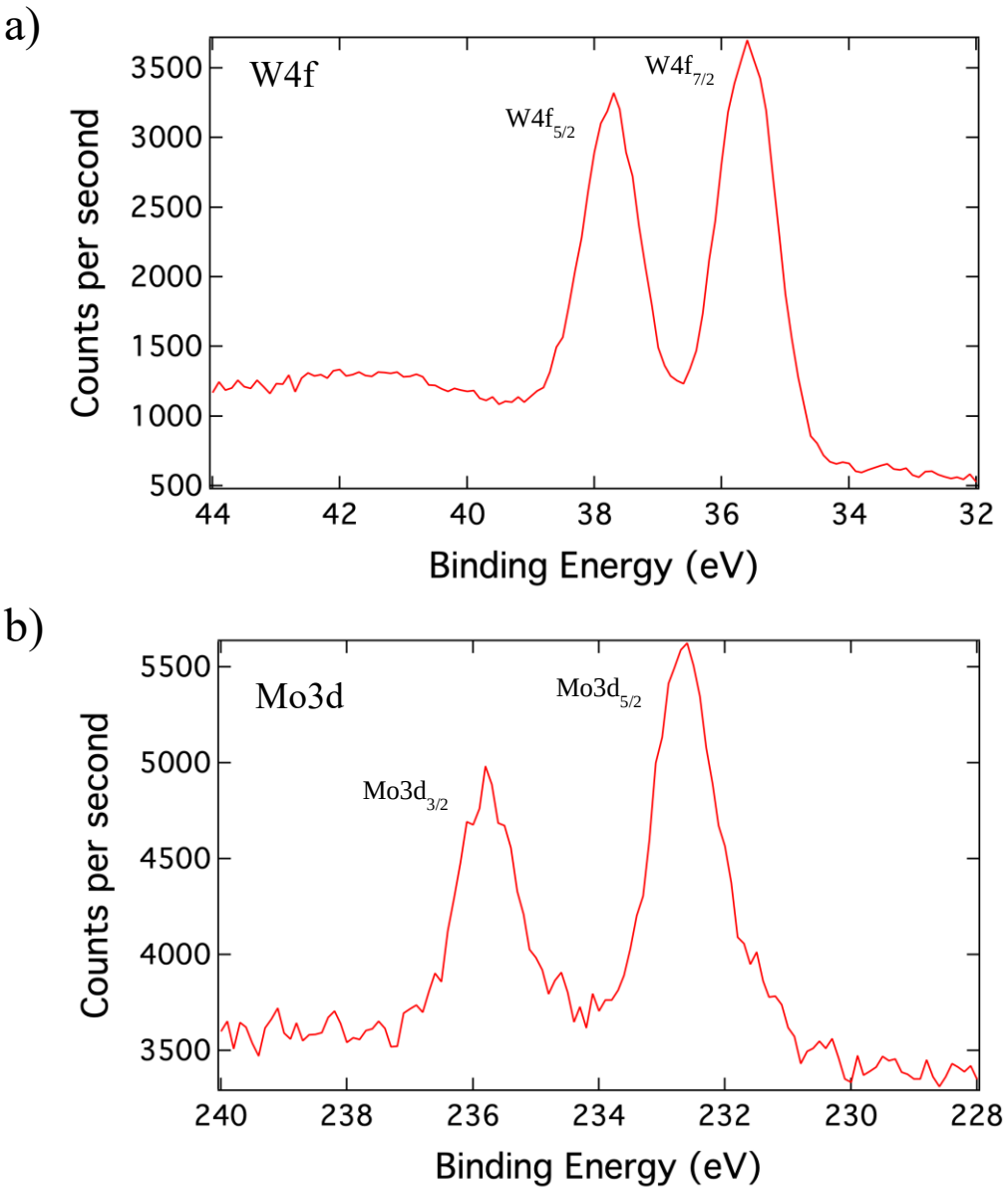

Figure B.3. XPS spectrum of electrodeposited MoO_3-WO_3 diffraction gratings confirming the presence of a) slightly reduced WO_3 with peaks appearing at 37.5 and 35.5 eV in the W4f region and b) slightly reduced MoO_3 with peaks appearing at 235.7 and 232.6 eV in the Mo3d region.

Appendix C

Supporting Information for Characterization of DNA-Nanogold Conjugates by Electron-Microscopy

C.1 ImageJ Line Profiles of DNA-Nanogold Cryo-EM Micrographs

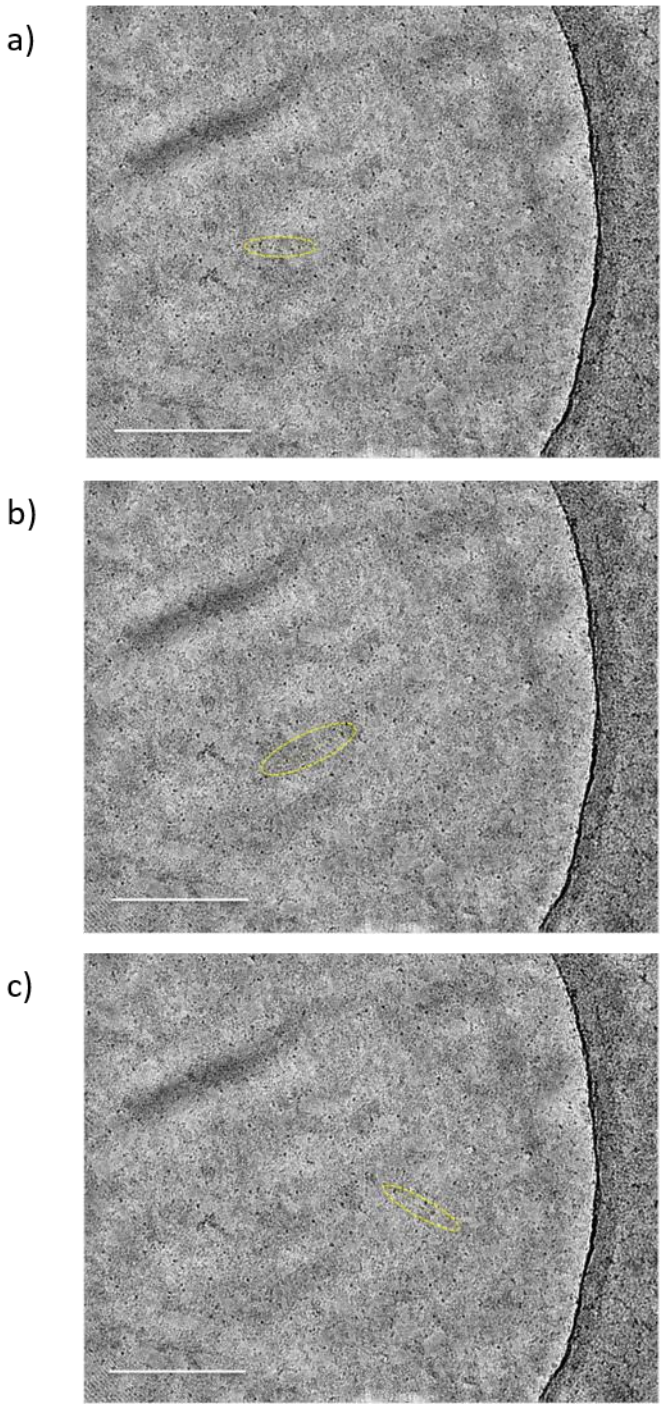

Figure C.1 a-c) ImageJ line profile of DNA-nanogold micrograph obtained using cryo-EM used to generate gray value intensities in Figure 4.6 a-c) respectively. Scale bars represents 50 nm.